USE OF IMPEDANCE SPECTROSCOPY TO INVESTIGATE FACTORS THAT INFLUENCE THE PERFORMANCE AND DURABILITY OF PROTON EXCHANGE MEMBRANE (PEM) FUEL CELLS

By

SUNIL K. ROY

A DISSERTATION PRESENTED TO THE GRADUATE SCHOOL
OF THE UNIVERSITY OF FLORIDA IN PARTIAL FULFILLMENT
OF THE REQUIREMENTS FOR THE DEGREE OF
DOCTOR OF PHILOSOPHY

UNIVERSITY OF FLORIDA

2008

To memory of my late mother and siblings

To inspiration and sacrifice of my father

To dedication of my sister-in-law

To smile of my angels, Mayank and Jayant

To my wife Asmita, the best gift I have received from GOD.

ACKNOWLEDGMENTS

I thank my advisor, Professor Mark Orazem, for his support, and guidance. He has shown me not only how to improve my abilities in research, but also how to improve my abilities as a person.

I wish to thank my colleagues, and group member Patrick McKinney, Erin Patrick, Shao-ling Wu, and Bryan Hirschorn, for their support and encouragement over the past four years. We have enjoyed conversation on the philosophy of life as well as on the technical issues associated with electrochemistry. By listening to my talks many times, they have helped me improve my presentation skills. I thank Chemical Engineering staffs Shirley Kelly, Dennis Vince, James Hinnant, Sean Poole, and Deborah Aldrich for their help with technical, computer, and purchase, respectively, essential for my research.

I would also like to thank NASA and Gamry Instruments Inc. for supporting this work. This work was supported by NASA Glenn Research Center under grant NAG 3-2930 monitored by Timothy Smith with additional support from Gamry Instruments Inc.

Finally, I like to give special credit to my parents, my sister, and my brother for their love and support throughout my life.

TABLE OF CONTENTS

page

LIST OF TABLES

LIST OF FIGURES

LIST OF SYMBOLS

b_i	Tafel constant (inversely related to the Tafel slope), V^{-1}
c	concentration, mole/cm^3
C_0	double layer capacitance, μF/cm^2
D_i	diffusivity of i species in ionomer agglomerates of the catalyst layer, m^2/s
i	current density, mA/cm^2
K_3	rate constant, mol/s
$K_{\mathrm{H_2}}$	rate constant of hydrogen oxidation, A cm/mol
$K_{\mathrm{H_2O_2}}$	rate constant of peroxide formation, A/mol
$K_{\mathrm{O_2}}$	rate constant of oxygen reduction, A cm/mol
K_{Pt}	rate constant of Pt oxidation, A cm/mol
$K_{\mathrm{Pt,b}}$	backward rate constant of Pt oxidation, A/cm^2
$K_{\mathrm{Pt,f}}$	forward rate constant of Pt oxidation, A/mol
K_{PtO}	rate constant of PtO formation, A cm/mol
n	number of electron exchanged in the reaction
R_e	membrane resistance, Ωcm^2
t	current density, mA/cm^2
U	cell potential, V
Z_j	imaginary part of impedance, Ωcm^2
Z_r	real part of impedance, Ωcm^2
δ	diffusion layer film thickness, m
Γ	maximum surface concentration, mole/cm^2
γ	fractional surface concentration, dimensionless
η_i	overpotential, V
ω	frequency, s^{-1}

Abstract of Dissertation Presented to the Graduate School
of the University of Florida in Partial Fulfillment of the
Requirements for the Degree of Doctor of Philosophy

USE OF IMPEDANCE SPECTROSCOPY TO INVESTIGATE FACTORS THAT INFLUENCE THE PERFORMANCE AND DURABILITY OF PROTON EXCHANGE MEMBRANE (PEM) FUEL CELLS

By

Sunil K. Roy

August 2008

Chair: Mark E. Orazem
Major: Chemical Engineering

Impedance spectroscopy provides the opportunity for in-situ identification and quantification of physical processes and has been used extensively to study the behavior of the fuel cell. However, a key question to be answered is whether the features seen in the impedance response are caused by an artifact or represent a physical process taking place in the system. The measurement model developed by our group can be used to identify the frequency ranges unaffected by bias errors associated with instrument artifacts and non-stationary behavior.

Impedance measurements were performed with the 850C fuel-cell test station supplied by Scribner Associates and with a Gamry Instruments FC350 impedance analyzer coupled with a Dynaload electronic load. All electrochemical measurements were performed with a two-electrode cell in which the anode served as a pseudo-reference electrode. The experiments were conducted in galavanostatic mode for a frequency range of 0.001-3000 Hz with 10 mA peak-to-peak sinusoidal perturbation, and ten points were collected per frequency decade. Ultra pure hydrogen was used as the anode fuel, and compressed air was used as oxidant.

The measurement model was used to show that low-frequency inductive loops were, in some cases, fully self consistent, and, therefore, the inductive loops could be attributed to processes occurring in the fuel cell. Then we developed first-principle models that

incorporate processes that may be responsible for the inductive response seen at low frequencies. We found that side reactions producing hydrogen peroxide intermediates and reactions causing Pt deactivation could yield inductive loops. These side reactions and the intermediates can degrade fuel cell components such as membranes and electrodes, thereby reducing the lifetime the fuel cells. The hypothesized reaction involving of peroxide and PtO formation were supported by microstructural characterization.

A more sensitive manner of using impedance spectroscopy to gain an insight into the problem of flooding which adversely affects the performance of the fuel cell was established. A comprehensive model for base-level noise in impedance measurements for normal (non-flooded) conditions was developed and actual noise in flooded conditions was calculated by transient fixed-frequency measurements. A comparison of the actual noise to the base-level noise was used to detect onset of flooding.

Also, graphical methods were used to interpret impedance spectra in terms of interfacial capacitance. The effective interfacial capacitance decreased with increase in current and decreased slowly with time. The decreases in interfacial capacitance with higher current density can be attributed to an excess amount of water i.e., flooding; whereas, the decrease in interfacial capacitance with time may be related to catalyst dissolution and deactivation.

CHAPTER 1
INTRODUCTION

PEM fuel cells are electrochemical reactors that convert chemical energy into electrical energy. These are promising energy converters in the 21^{th} century because of their pollution free characteristic and high power density; however, several issues unresolved which have limited commercialization of this fascinating technology on a large scale. Cost is one such factor. The required catalyst, membrane and cell hardware (e.g. bipolar plates) are expensive, resulting in a very high initial cost. In addition, hydrogen gas, a fuel required for fuel cells, is not widely available, has a low volumetric energy density, therefore is difficult to store. This reduces the operational range of portable fuel cell devices. Storing hydrogen in carbon nanotubes[5] and metal hydrides[6] has received a great deal of attention recently. In addition, less explored mechanisms such as side reactions and intermediates (peroxide formation,[7–9] platinum oxidation and dissolution,[10] carbon corrosion,[11] etc.) reduce performance and life-time. Water management issues[12] such as flooding and drying also limit operation of the fuel cell in normal operation, and under start/stop cycling.

The object of this work was to investigate factors and processes which adversely affect the fuel cell operation. The factors analyzed in this work include side reactions and intermediates in the reactions kinetics, and flooding of the fuel cell. In the last few decades, much attention have been given to research and development of the fuel cell; however, the role of side reactions and reaction intermediates is comparatively unexplored. Side reactions and the associated intermediates can degrade the fuel cell components such as membranes and electrodes, thereby reducing the lifetime, one of the crucial issues in the commercialization of fuel cells. In addition, impedance spectroscopy in conjunction with the measurement model analysis was used to gain an insight into the problem of flooding, and drying which adversely affect the performance of the fuel cell.

CHAPTER 2
LITERATURE REVIEW

Fuel cells convert chemical energy of a reaction directly into electrical energy without combustion. Fuel cells generally have minimum moving parts, which make them highly reliable and long-lasting systems. Theoretically, it creates zero environments and health hazardous. These features make the fuel cell attractive for a large variety of applications, including road vehicles, decentralized power production, residential energy systems, and even smaller potential applications like portable electronics.

Fuel cells have components and characteristics similar to an ordinary battery but they differ in several respects. Generally, batteries cease to produce electrical energy when the limiting chemical reactants are consumed whereas fuel cells produce electrical energy for as long as reactants are supplied. Batteries scale poorly at large sizes while fuel cells scale well from the 1W range (cell phone) to the MW range (power plant). Fuel cells offer potentially higher energy densities, and can be instantly recharged by refueling, while batteries must be thrown away or plugged in for a time-consuming recharge. Materials used in batteries (electrodes) have to go through changes during charing/discharging cycles, which eventually result, into degraded energy output and/or catastrophic failure.[13] The performance of fuel cells is not subject to Carnot efficiency unlike heat engines. Fuel cells are often far more efficient than combustion engines. Combustion also has disadvantages of undesired gases such CO, CO_2, NO_x, SO_x, and particulate emissions.

Although there are different types of fuel cells, PEM fuel cells are regarded as the most suitable fuel cell at moderate temperature (60 - 100°C) due to their high power density, compact design, minimum pollutants emissions. Fuel cells have been known for a long time. In 1839, William Grove, was credited with first developing the principle of the fuel cell. Grove utilized four large cells, each containing hydrogen and oxygen, to produce electrical power and, water as a byproduct.[14] The schematic of a PEMFC is shown in Figure 2-1(a). The fuel cell uses a PEM as an electrolyte. Hydrogen gas as fuel is supplied at the anode and oxygen gas or air as oxidant is supplied at the cathode. The following two half-cell reactions (2–1) and (2–2) take place at the anode and the cathode respectively, and equation (2–3) is the overall reaction in the fuel cell.

$$\mathrm{H_2 \rightarrow 2H^+ + 2e^-} \tag{2–1}$$

$$\mathrm{O_2 + 4H^+ + 4e^- \rightarrow 2H_2O} \tag{2–2}$$

$$\mathrm{O_2 + 2H_2 \rightarrow 2H_2O} \tag{2–3}$$

The main components of the fuel cell are shown in Figure 2-1(b). The fuel cell typically consists of a membrane, two electrodes, gas diffusion layers (GDL), and bipolar plates.

2.1 Electrochemistry and Losses in the Fuel Cell

The change in Gibbs free energy (ΔG) is measure of the maximum work obtainable from the reaction. ΔG for the overall reaction (2–3) in the fuel cell is -237.14 kJ/mole at standard conditions. Cell potential can be calculated by equation (2–4).

$$\Delta G = nFE^0 \tag{2–4}$$

where F is Faraday constant equals to 96485 C/mole, n is number of moles of electrons involved in the reaction, and E^0 is electrode potential. Equation gives value of cell potential as 1.23V which is referred as an open circuit voltage (OCV). ΔG is a function of operating conditions such as operating temperature and pressure, hence the OCV also depends on the operating conditions of the cell. The dependency of the potential is described by the Nernst equation which gives the thermodynamic voltage of fuel cells.

$$E_{nernst} = E^0 + \frac{RT}{nF} ln(\frac{P_{H_2}}{P_{O_2}}) \tag{2–5}$$

where R is Universal gas constant, T is temperature, P_i is pressure for i reactants. The actual voltage output of a fuel cell is less than the thermodynamically predicted (Nernst Equation) voltage due to several irreversible losses.[2] A plot of cell voltage versus current density known as polarization curve (Figure 2-2), which shows various losses taking place in the fuel cell. The actual voltage drawn from the fuel cell should be equal to the

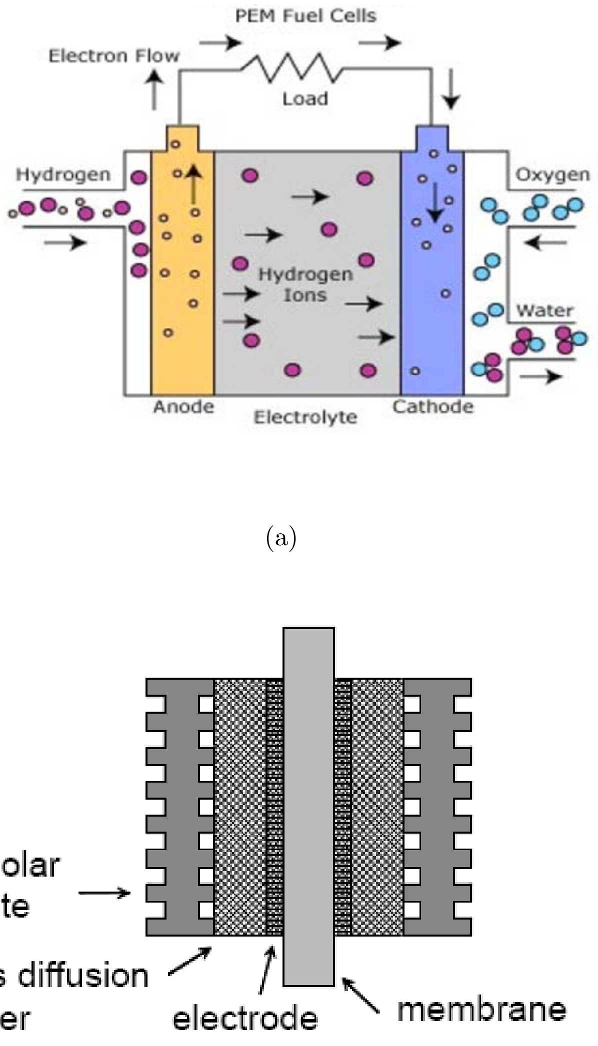

(a)

(b)

Figure 2-1: Illustration of the fuel cell (taken from literature[1]); a) flow diagram; and b) components.

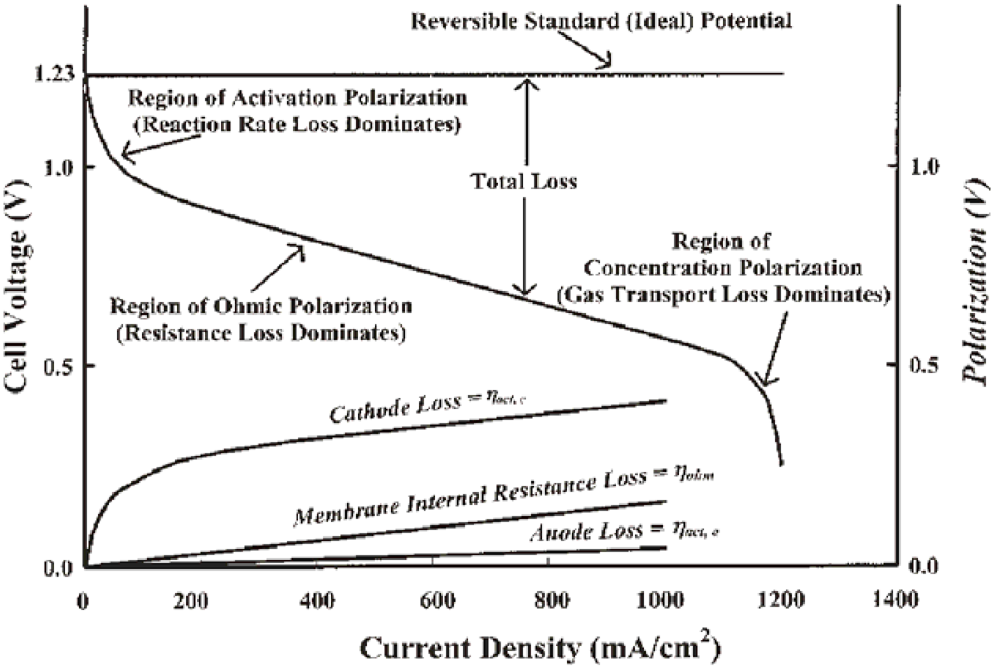

Figure 2-2: A polarization curve for a fuel cell (taken from Lin *et al.*[2]), showing the losses associated with reaction kinetics, internal electrical resistance, and mass transports.

difference of theoretical voltage and the various losses:

$$E_{actual} = E_{nernst} - \eta_{act.} - \eta_{conc.} - IR_e - \eta_{parasite} \tag{2–6}$$

where E_{actual} is actual voltage, E_{nernst} is thermodynamically predicted voltage, $\eta_{conc.}$ is concentration loss, $\eta_{act.}$ is activation loss, $\eta_{parasite}$ is parasite loss and IR_e is Ohmic loss.

2.1.1 Activation Loss

At low current density, the cell voltage drops rapidly due to sluggishness of electrokinetics at electrodes. ORR is slower and can account for most of the activation losses. In addition, competing reactions occur at the oxygen electrode such as oxidation of the platinum, corrosion of carbon support, and oxidation of organic impurities on the electrode can lead to loss of voltage. The activation loss can be derived from the Butler-Volmer equation as:

$$\eta_{act.} = \frac{RT}{\alpha F}\ln(\frac{i}{i_0}) \tag{2–7}$$

where i is current density, i_0 is exchange current density, and α is apparent transfer coefficient.

Activation losses are minimized by maximizing the exchange current density. The exchange current density is a function of the catalyst material and the electrochemical active surface area. The electrodes are made highly porous by dispersing, nano-scale particles of platinum on electronic conductor porous carbon support mixed with an ion conductive electrolyte to enhance the overall active area.

2.1.2 Ohmic Potential Loss

Ohmic losses arise due to the resistance of the materials (electrodes, membrane) to flow of species such as proton transport through the membrane and electrodes, electron transport through electrodes, bipolar plates, and collector plates. It appears as a linear part in the middle of polarization curve. The magnitudes of these potential losses depend on the materials used in the construction of the fuel cell and the operating conditions of the cell. Most of the ohmic loss arises from the ionic resistance in the electrolyte. The thinner the membrane, the lower this loss. Thinner membranes are also advantageous because they keep the anode electrode wet by back-diffusion of water from the cathode, however very thin membrane could lead to pinhole formation and therefore gas crossover.

It is also reported that the interfacial resistance between the gas diffusion layer and the bipolar plate might contribute significantly to the total ohmic resistance, especially when alternative bipolar plate materials such as steel are used.[15]

2.1.3 Concentration Overpotential Loss

At high current densities, the voltage output of the fuel cell once again drops rapidly due to mass-transport limitations at the electrodes. The concentration losses can be evaluated as:

$$\eta_{conc.} = \frac{RT}{\alpha F} \ln(\frac{i_{lim}}{i_{lim} - i}) \tag{2–8}$$

where i_{lim} is limiting current densities.

This loss mainly arises from the mass-transport resistance in catalyst and diffusion layers. However, mass-transport in the diffusion layer can also be affected by the channel geometry of the flow field plate. In addition, at high current density hefty amounts of water are produced, which causes flooding of the cathode surface and inhibits the transport of reactants as well as ionic species.

The physical properties of the diffusion layers such as porosity can be affected by several factors, which may result into mass-transport overpotential. At high current densities, the porosity is reduced compared to the dry state by the presence of liquid water. The porosity of the diffusion layers is also affected by the compression force applied while assembling the fuel cell. Excessive compression reduces the porosity which hinders gas-transport, whereas too little compression may cause an increase in contact resistances. The mass-transport loss at very high current densities is also attributed to drying of the anode.[16]

2.1.4 Parasitic Potential Loss

Even in the limit of zero current in the fuel cell, the output voltage of the cell is less than the thermodynamically predicted voltage. This decrease is due to gas crossover and undesired electron leaks across the electrolyte membrane. Fuel crossover is the amount of fuel that crosses the membrane from the anode to the cathode without being oxidized at the anode catalyst layer, which results in a loss of fuel. Internal current is the flow of electron from the anode to the cathode through the membrane instead of going through the external circuit. Many other unknown processes can also contribute to this loss; one of the processes can be proton transport thorough the membrane which defined as convection overpotential given as:[17,18]

$$\eta_{conv.} = F\nu C_{H^+}\frac{l_m}{k} \tag{2–9}$$

where C_{H^+} is proton concentration, ν is water velocity in the membrane, l_m is thickness of membrane, and k is membrane conductivity.

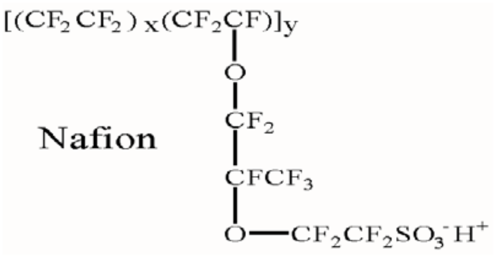

Figure 2-3: Chemical structure of Nafion (taken from Weber and Newman *et al.*[3]).

2.2 PEM Fuel Cell Components

2.2.1 Membrane

A thin electrolyte layer spatially separates the hydrogen and oxygen electrodes and ensures that the two individual half reactions occur in isolation from one another. It must not allow electrons to cross, but must allow protons to pass easily. The membrane should possesses high ionic conductivity, high stability (water management), low fuel crossover, high mechanical strength, good electronic insulation, good separation of reactants, high chemical and thermal stability, and low cost.[19]

The standard membrane is made of sulfonated poly-tetra-flouroethylene (PTFE) as backbone where some of the fluorine atoms are partially substituted by chains containing sulfonic acid. This membrane material produced by DuPont carries the brand name as Nafion. Molecular formula of Nafion is shown in Figure 2-3. The backbone (hydrophobic phase) provides Nafion with an excellent oxidative stability, mechanical integrity, and limits the swelling of membrane while sulphonic group (hydrophilic phase) helps proton transport. The high electronegativity of the fluorine atoms bonded to the same carbon atom as the sulfonic acid group makes the $-SO_3H$ a superacid.

The exact structure of Nafion is not known however, it is reported that electrostatic interactions (between the ions and the ion-pairs) cause the ionic groups to aggregate and form tightly packed regions referred as clusters. These interactions enhance the intermolecular forces and considerably influence the properties of the parent polymer.

Small angle X-ray scattering and neutron scattering experiments can be used to indicate ionic clustering in Nafion.

The proton conductivity of Nafion is dependant on its hydration state. In the dry state, Nafion is a poor ion conductor, but ionic conductivity increases sharply with water content.[3] In dry state, protons may migrate from one acid group to another in the network; the associated activation energy is relatively high, resulting in relatively low ionic conductivity. However, when water fills the pore network, the protons are solvated by one or more water molecules. Water solvation partially screens the proton charge, thus lowering the activation energy for migration. To ensure membrane hydration humidified gases are generally fed into the fuel cell.

Nafion dehydrates at temperature above 80°C; the dehydration can cause membrane to shrink, reducing contact between electrodes and membrane therefore higher contact resistance. The shrink may also cause pinholes formation, leading to reactant crossover.[20] Nafion also shows considerable deterioration in the conductivity and the mechanical strength above the glass transition temperature (ca. 110°C).

A lifetime of over 60,000 hours under fuel cell conditions has been achieved with commercial Nafion membranes. However, even extremely stable Nafion can suffer from degradation. Using XPS analysis of the MEA before and after fuel cell operation Huang *et al.*[21] has found that $-CF_2-$ groups of Nafion are destroyed under electrochemical stress, yielding the $-HCF-$ or $-CCF-$ configurations. Under the anode potential, the hydrophobic part (e.g., fluorocarbon) may react with carbon or hydrogen atoms, resulting finally in the degradation of the electrolyte. Also, this kind of hydrocarbon membranes are prone to oxidative degradation by peroxide intermediates. The high cost and high methanol permeability of the fluorinated polymers also urge the necessity to develop alternative proton-conducting polymers.

A great number of polymer materials have been prepared and functionalised for possible electrolytes for fuel cells. Improvements in the membrane structure and conductivity were achieved by producing composite membranes. Usually, PTFE is added into Nafion to improve mechanical strength, therefore much thinner layer of PTFE blended Nafion can be used which has advantage of low Ohmic drop as compared to pure Nafion. However, thinner PTFE doped Nafion has larger permeation rate thus low OCV.[22] The larger permeation results in higher crossover of reactants, and heat generated by reaction due to local hot spots create localized membrane drying, and higher membrane resistance. The crossover of reactants have been utilized to make these membrane self-humidifying by providing highly dispersed Pt particles in the membrane which enables localized formation of water though uniform distribution of Pt is not achieved. To exploit this idea, very thin layers of Pt/C have been used both side of the membrane which reduces the crossover as well as ensure formation of water to humidify membrane.[22]

Also, a compound $Cs_{2.5}H_{0.5}PW_{12}O_{40}$ has been investigated to incorporate into Nafion/PTFE composite, better performance observed is attributed to strong acidic and hydrophilic nature of the compound which enhance water retention capacity.[23] A composite membrane by blending Nafion with poly(vinylidene fluoride) is investigated though the observed proton conductive is much lower than Nafion which is due extreme hydrophobicity of fluoride components. To improve water affinity and proton conductivity, the composite is chemically modified by dehydrofluorination and treatment with $\mathbf{H}_2SO_4$.[24] W.L. Gore and Asahi Chemicals have successfully reinforced perfluorosulfonic acid membranes with Teflon fabric.[25] Carbon nanotubes have been proposed to incorporate into Nafion to increase mechanical stability due to their exceptional enforcing fibre strength, low density and high aspect ratio, however, since carbon is electronic conductor which can lead to electronic short-circuit thus reducing the OCV.[26]

By operating fuel cells at higher temperature, the oxygen reduction kinetics and carbon monoxide poisoning problems are improved. Composites are made by swelling the perfluorinated ionomeric membrane with an ionic liquid to improve its high temperature stability.[27] To improve the hydration characteristics of Nafion, nanoparticles of hygroscopic metal oxides such as Silicon oxide is incorporated into Nafion. The water retention capacity is improves which enable use of this composite at elevated temperature however, the composite shows higher ohmic resistance may be due to disruption of proton conduction path in Nafion by presence of silicon oxide particles.[20]

Non-Nafion membranes were also investigated for intermediate-temperature operation of fuel cells.[28,29] Usually, phosphate based proton conductors are blended with inorganic compound such as silicate or metal which provide mechanical stability to the composite. Since PO_4^{-3} is thermally stable above 200 °C while proton sources (SO_4^{-2}) in Nafion decomposes above 200 °C. Several composite membranes for high temperature applications[30–37] are investigated. Composite membrane were explored by doping Nafion with different heteropolyacids such as phosphotungstic acid, silicotungstic acid, phosphomolybdic acid, and silicomolybdic acid.[32] Heteropolyacids typically exist in the hydrated phase with 30 to 6 water molecules per acid molecule; the rationale behind using these acids is to utilize the additional water molecule for humidification of membrane especially at higher temperature. Very little improvement in the performance is recorded which is attributed to larger particles of these additives which are unable to help conduction of protons through the membrane cluster. It is also reported that these acids dissolve; Molybdate atoms are observed on catalyst layer which may be due to migration of molecules to catalyst layer though additives with Tungsten is relatively stable in the membrane. To improve above disadvantages, these acids are stabilized by cations which ensure uniform dispersion of smaller acid particles and therefore help create effective bridging between ionic domains.[32]

Heterocyclic aromatic polymer are used due to their excellent thermal and chemical resistance and superior mechanical integrity. Some of the most promising candidates for proton-exchange membranes are high performance polymers, ie. polyimides, poly(ether ketone)s, poly(arylene ether sulfone)s, polybenzimidazoles, etc. Advantages of using these materials are lower cost than perfluorinated membranes, inclusion of polar groups to improve water uptake over a range of temperatures, and the possibility of recycling by conventional methods.

The six-membered ring of the naphthalenic polyimide is much more stable to hydrolysis, this membrane is better suited for fuel cell applications[38] while five-membered ring polyimides which may undergo hydrolysis of the phthalimide structure under strong acid conditions quickly leads to chain scission and causes the membrane to become brittle.[39] This indicates that the stability of the highly cross-linked membranes is not only caused by cross-linking of the polystyrene chains, which slows down the loss of $-\mathrm{SO}_3H$ from the membranes, but also by reduced gas crossover and, therefore, reduced $\mathrm{HO}_2\bullet$ and OH^- formation. High degrees of cross-linking (more than 12) could improve the stability, however, the simultaneous increase of membrane resistance might not be tolerable. The optimum membrane thickness, which, as a compromise between gas crossover and resistance, must be found. Another crucial point is the $\mathrm{C}-\mathrm{O}-\mathrm{C}$ bond breaking, initiated by attack of OH^-. In the presence of both OH^- radicals and oxygen, complete degradation of the aromatic rings can be achieved within a few hours. In view of this, the saturated and perfluorinated Nafion which is much more inert has an inherent advantage over the new membranes based on aromatic hydrocarbons.

2.2.2 Electrodes

The major requirements for an effective catalyst are high activity, high electrical conductivity, high proton conductivity, low corrosion, high porosity, high mechanical strength, and highly porous to ensure good gas access. State-of-the-art catalysts utilize nano-sized platinum particles (3-10 nm) supported on a high surface area carbon powder (30-50 nm). While platinum provides the catalytic activity, the carbon provides the electrical conductivity necessary to harvest electrons to/from the active sites. The carbon-supported platinum (Pt/C) structure offers a high catalytic surface area, significantly reducing the

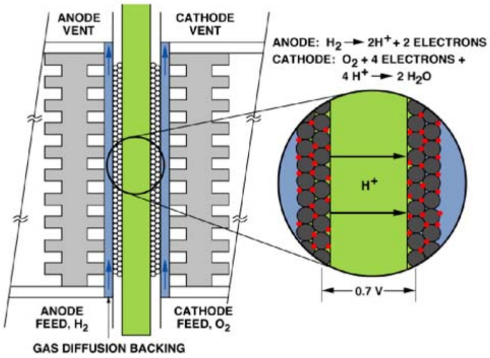

Figure 2-4: A schematic representation of membrane electrode assembly(MEA)(taken from literature[1]).

required platinum loading (generally less than 0.5mg Pt/cm^2). The Pt/C powder is mixed with small quantity of the Nafion electrolyte to ensure proton conduction. In practice, the thickness of the catalyst layer is between 10-50 micron. While a thin layer is preferred for better reactants diffusion and catalyst utilization, a thick layer incorporates higher catalyst loading thus catalyst layer optimization requires a delicate balance between mass transport and catalytic activity concerns. To distribute Pt on Carbon uniformly, a surfactant is suggested which stabilizes the nanoparticles of Pt and prevent aggregation.[40] Also, use of an optimum amount of ammonium carbonate as an additive to catalyst layer is suggested which aids in pore forming thus improves the mass-transport limitations.[41]

To reduce the cost of cathode catalyst, alloys such as Platinum-Iridium ($Pt - Ir$),[42] Pt-Cobalt ($Pt - Co$),[43] Pt-Iron Phosphate ($Pt - FePO_4$)[44] have been investigated as possible cathode materials. The problem with these transition metal alloys are durability, these are unstable in acidic environment of the fuel cell. Addition of Ni in Pt-alloy (Pt_3Ni_1), was observed to shorten the Pt-Pt interatomic distance, thus resulting in stronger bonding reducing dissolution and loss of catalyst. However, the alloy shows higher interfacial resistance, and dissolution of metal in fuel cell environment, and subsequent diffusion of Ni into membrane can degrade the lifetime of fuel cell.[45] Similarly, less expensive catalysts by alloying Pt with $Fe - Ni - Co$ were explored; the initial activities for $Pt - Fe$ was found to be the highest; however, dissolution and subsequent leaching of metal into the membrane were found to cause additional deterioration of MEA and therefore reduce the lifetime.[46,47]

Non-platinum materials such as Zirconium oxide[48] and Tantalum oxynitride[49] is also investigated for cathode catalyst. Sol derived[50] materials with transition metal such as Cobalt (Co) on carbon support when added with aromatic ligand 1,2-phenylenediamine can also be used as a cathode catalyst. Tungsten Carbide (WC) with addition of Tantalum (Ta) is also investigated for a catalyst; the Tantalum is added to enhance the corrosion resistance of the carbide. It is reported that Tantalum forms an alloy $(W - Ta)$ with Tungsten which enhances electroactivity and corrosion resistance of the material.[51] A single-walled carbon-nanotube-based proton exchange membrane assemblies for hydrogen fuel cells was also explored.[52]

The ideal carbon support should possess high chemical/electrochemical stability, good electronic conductivity, and a suitably high surface area and pore size distribution.[53] A carbon black commercially known as Vulcan XC72(Cabot Corp.) is the most common used catalyst support. However, it has random structure and broad pore-size distribution which lead to even distribution of Nafion. Also, the micro-pore can not be filled by Nafion because Nafion particles are usually bigger than the pore size, therefore Pt particles inside the micro-pore are not accessible to electrochemical reaction thus reduces catalyst utilization.[54] Better performance is observed using oriented Carbon nanotubes (CNTs) instead of the conventional carbon as catalyst support. Electronic conductivity and gas permeability are expected to be much higher along the CNTs than across the tube, and also oriented CNTs may exhibit superhydrophobicity, which can facilitate water removal within the electrode; these factors may be attributed to the improvement in the performance.[55] It is also reported that Pt/CNTs has better lifetime compared to Pt/C.[56] However, carbon nanotubes consist of hollow cylinder, so higher dispersion of Pt particles are difficult inside the nanotubes because of diameter-to-length ratio in a single nanotubes. To overcome this problem, catalyst support based on carbon aerogel-based was explored and better performance was observed.[54]

Gold has been also investigated as a possible catalyst support which shows comparable electrochemical active area and so the performance with Carbon on much lower Pt loadings though the cost of Gold is a concern.[57] A conducting polymer composite[58] for catalyst support material, was tested. The composite consists of an electronic conductive end (e.g. polyprrole, poly(3,4-ethylenedioxythiophene)), and a proton conducting end (e.g. polystyrenesulfonate). It has excellent performance for oxygen reduction reaction however; a decimal performance is observed for hydrogen oxidation because at anode potential the electronic conducting functional group becomes inactive. Tungsten Oxide (WO_3) was also proposed as a possible catalyst support as it is a stable oxide and not prone to **PtO** formation compared to conventional catalyst support.[59] It is also more thermally stable than Carbon which enables its use in high temperature operation of the fuel cell. Polyaniline doped trifluoromethane sulfonic acid is investigated as a proton conducting material to be used in catalyst instead Nafion. Its fibrous nature helps distribute particles uniformly, and ensures better connection of reaction sites, and thus enhances Pt utilization compared to Nafion.

Optimization of catalyst composition with respect to Pt, and Nafion loadings has been investigated thoroughly. An optimal composition of Nafion has observed; to little Nafion was insufficient for proton conduction thus increases ionic resistance, on the other hand, too much Nafion, may cover Pt particles forming a films that hinders electron transport to Pt therefore reduces catalyst utilization. Also, it fills carbon pores hindering gas transport and water removal. Since Nafion is not mechanically stable at higher water content so in case of flooding too much Nafion can lead to break-down of catalyst layer. Nafion loading usually results in Ohmic and mass-transport (diffusion) limitation in the fuel cell operation.

An optimal film thickness for given Nafionn loading was suggested.[60] A Nafion loading of 1.3 mg/cm^2 was found to correspond to the optimal film thickness sufficient to transport proton without hindering electron and gas transport. Nafion loading greater than the optimal value results in an additional arc at low frequency in impedance response representing gas-diffusion limitation.[61] Further improvement in Nafion loading is obtained to 0.8 mg/cm^2 by using a catalyst support between catalyst layer and gas diffusion layer in the fuel cell.[61] Electrodes consisting of two layers with different Nafion loading was also proposed, but no better performance was obtained.[62]

2.2.3 Gas Diffusion Layers

The functions of the gas diffusion layers are to provide structural support for the catalyst layers, passages for reactant gases to reach the catalyst layers and transport of water to or from the catalyst layers, electron transport from the catalyst layer to the bipolar plate in the anode side and from the bipolar plate to the catalyst layer in the cathode side, and heat removal from the catalyst layers. The common materials for the GDL are carbon paper and carbon cloth which incorporates a hydrophobic material, such as PTFE to prevent water from pooling within the pore of the backing layer. Furthermore, PTFE creates a non-wetting surface within the passages of the backing material which facilitates product water removal on the cathode.

The physical properties such as pore size and structure, hydrophobicity, and thickness of GDL play major role in mass-transport processes. Kong *et al.*[63] report that macropores prevent flooding and thus improves performance. To modify pore structure, pore-forming agents such as Li_2CO_3 were investigated. Some authors[64–66] suggested using a two-layer structure as a gas backing. The layer closer to the electrode is know as the diffusion layers and should have a finer structure to ensure that as many catalyst particles as possible are in electric contact. Capillary action associated with the finer pore structure enhance transport of reactants to the catalyst sites. The diffusion layer distributes reactants more uniformly, enhances mechanical compatibly with catalyst layer, and reduces contact resistance.[67] The layer facing the flow field plate is known as the backing layer. It should be thicker and should have a coarser structure.

Application of an optimum compression force while assembling the fuel cell has been advocated.[66] The compressive force should be estimated based on GDL thickness and gasket compression: too much compressive force might reduce the porosity changing water hold up and thus reducing electrochemical active area and creating mass-transport problems, whereas too little force might increase contact resistances. It was also reported that the compression particulary reduces porosity and thickness of GDL under land portion (of channel) which specially influences higher current density by limiting transport of oxygen.[18] Sintered Titanium was also suggested to be as a GDL material due to its lower cost, though it has high contact resistance with MEA. The resistance can be reduced by applying Pt coating on the GDL surface.[68]

2.2.4 Bipolar Plates

A plate in contact with the GDL is known as bipolar plate. The plate usually incorporates flow channel for reactants feed and may contain conduits for heat transfer. The desired characteristics of bipolar plate materials are high electrical conductivity, impermeability to gases, high thermal conductivity, lightweight, high corrosion resistant, and easy to manufacture.

The common materials used for bipolar plates are graphite, and metals such as stainless steel, aluminum, or composite material. Graphite plates meet most of the requirements for optimal fuel cell performance but the flow-channel machining of graphite is so expensive that graphite plates can take up to half the cost of a fuel cell system. Metallic plates are cheap and easy to manufacture, however, these have a high contact resistance due to the formation of metal oxide layer between the plate and the GDL. Pozio *et al.*[69] has reported that Iron, a contamination in stainless steel (SS316L) bipolar plates, reacts with electrolyte (Nafion) and degrades it. A ferrite stainless steel sample with different composition of Chromium has been reported as bipolar plate, it has found that the sample with highest chromium content was better material for bipolar plate. Composites can offer the combined advantages of high electrical and thermal conductivity of graphite plates, and low manufacturing cost of metallic plate.[70] Middleman *et al.*[71] has reported graphite filled polymer composite for possible bipolar plate material developed by Nedstack (Arnhem, The Netherlands). Oh *et al.*[72] have studied electrical and physical properties of polymer composite material with Pd-Ni coating for bipolar plate. These materials have lower electrical interfacial resistance and higher surface roughness when compared with conventional resin-impregnated graphite material.

The functions of the bipolar plate are to provide the pathways for reactant gas transport, and electron conduction paths from one cell to another in the fuel cell stack, separate the individual cells in the stack, carry water away from the cells, and provide cooling passages. Plate material and topologies facilitate these functions. Common topologies used are straight, serpentine, or inter-digitated flow fields. Serpentine is the most common geometry found in fuel cell prototypes. The advantage of the serpentine pattern lies in the water removal capability. Only one flow path exists in the pattern, so liquid water is forced to exit the channel. However, in large area cells, a serpentine design leads to a large pressure drop. Several variations of the serpentine design have been investigated, such as the parallel-serpentine configuration. The interdigitated design promotes forced convection of the reactant gasses through the gas diffusion layer. Subject to much recent attention, research has shown that this design provides far better water management, leading to improved mass transport.[73] But the forced convection through the gas diffusion layer leads to significant pressure drop losses. However, there is evidence that this major disadvantage might be partially overcome by employing extremely small rib spacing.[74]

2.3 Degradation Mechanisms in Fuel Cells

The durability is one of the most critical issues in commercialization of fuel cells.[75] The degradation and performance loss can be affected by several factors, some of them are discuss in following sections.

2.3.1 Hydrogen Peroxide Formation

Hydrogen peroxide, a strong oxidizing agent, degrades materials thus limits the performance and lifetime of the fuel cell. The peroxide can be formed by two-electron reduction of oxygen in the fuel cell environment as following suggested by researchers.[7,8,76]

$$\mathrm{O_2 + 2H^+ + 2e^- \rightarrow H_2O_2} \tag{2–10}$$

Evidence of the peroxide formation has investigated rigorously. A rotating-ring-disk-electrode study[77] revealed that formation of the peroxide on platinum particles supported on carbon (catalyst used in the fuel cell) is quite possible by two-electron reduction while the formation was not observed on clean bulk platinum. The peroxide formation was reported to be more pronounced on Pt/C as compared with pure Pt surface and the formation is greatly enhanced by a decrease in the agglomeration of Pt particles.[77] An experimental arrangement was illustrated to detect in-situ hydrogen peroxide formation in the fuel cell.[78] The recorded in-situ CV have two peaks one corresponding to peroxide formation and other PtO formation. They also found that thinner membrane has higher peroxide concentration which is possible by Oxygen crossover from the cathode to the anode.[78] In processing, the membrane (Nafion) is usually pre-treated in boiling peroxide which can also be a source for peroxide in membrane to trigger formation of these radicals leading to degradation.[79] The peroxide formation has been also reported in case of air bleed. In case of CO contamination in fuel, air-bleed is done to promote oxidation of CO to CO_2 (cleansing) but only a small fraction of fed oxygen is used for the oxidation, while major fraction of oxygen competes with ORR and produces hydrogen peroxide.[80]

The formation of peroxide at cathode has been reported due to crossover of hydrogen from anode to cathode. The effect of temperature and humidity on peroxide formation kinetics was studied showing higher concentration of peroxide at the cathode compared to at the anode.[81] The peroxide formation inside the membrane was also observed due to presence of platinum band.[82] The formation of Pt band is possible due to dissolution and migration of Pt particles from electrodes and redeposition inside membrane.

The hydrogen peroxide initiates formation of reactive radicals such as Hydroxyl and hydroperoxyl in presence of Fe^{+3}, Cu^{+2}, etc. as follows[81,83]

$$H_2O_2 + M^{+2} \rightarrow M^{+3} + OH \bullet + OH^- \tag{2–11}$$

$$H_2O_2 + OH\bullet \rightarrow OOH \bullet + H_2O \tag{2–12}$$

To investigate the formation of these radical in the fuel cell, electron spin resonance (ESR) study has been used by Endoh et al.[84] They have also found that these radicals degrade catalyst by attacking carbon in catalyst layer. These radicals attack side-chain of membrane forming HF therefore fluorine emission rate (FER) is proposed as an indication of membrane degradation.[81,9,85] However, peroxide concentration can not be directly related to membrane degradation because degradation results from a series of reactions: formation of peroxide, followed by formation of radicals, finally attack of these radicals on side-chain. Also, formation of radicals require presence of metal ions.[78] These ions are typical contamination from piping, tubes, and storage tanks of the fuel cell. Fe^{+3} can also arise from bipolar plate contamination.[69] FER represents material erosion and decomposition across the overall cell may not accurately reflect local degradation of membrane which depends on local temperature, hydration level, contamination concentration, etc.[86] The formation of cross-linking $S - O - S$ is reported which can be due to dissolution of acidic group of Nafion ($-SO_3H$; pendent side-chain) provoked by peroxide leading to degradation.[87] The loss of acidic sites, reduction in proton conductivity of membrane was observed.

2.3.2 Platinum Oxidation and Dissolution

Platinum dissolves[10] in the fuel cell environment, which can also leads to the loss of catalytic activity and, consequently, the degradation of the electrode of the fuel cell and hence loss in performance.[88] A scheme for dissolution of platinum was suggested by Meyers et al.[10] as follows.

$$\mathrm{Pt} + \mathrm{H_2O} \rightleftarrows \mathrm{PtO} + 2\mathrm{H^+} + 2\mathrm{e^-} \tag{2–13}$$

in which PtO is formed, followed by a chemical dissolution reaction

$$\mathrm{PtO} + 2\mathrm{H^+} \rightarrow \mathrm{Pt^{+2}} + \mathrm{H_2O} \tag{2–14}$$

The first step leads to formation of a protective layer of PtO which reduces active surface area by blocking reaction sites. In the second step, the PtO oxide dissolves to form Pt ion leading to loss of catalyst particles. The formation of the platinum oxide is supposed to have an indirect influence on the ORR at the cathode by changing the effective rate constant for the reaction.

Another scheme for PtO formation in presence of water/oxygen was advocated along with different reactive radicals which degrade membrane, catalyst, and catalyst support used in the fuel cell.[89] Effect of humidity on PtO formation was reported; formation of PtO was observed even in absence of oxygen at the cathode.[90] The oxide formation was proposed to follow

$$\mathrm{Pt} + \mathrm{H_2O} \rightarrow \mathrm{Pt - OH} + \mathrm{H^+} + \mathrm{e^-} \tag{2–15}$$

$$\mathrm{Pt - OH} \rightarrow \mathrm{PtO} + \mathrm{H^+} + \mathrm{e^-} \tag{2–16}$$

with a larger amount of PtO observed at lower humidity.

The formation of PtO, and $\mathrm{PtO_2}$ was reported to follow.[91]

$$\mathrm{Pt} + \mathrm{H_2O} \rightarrow \mathrm{PtO} + 2\mathrm{H^+} + 2\mathrm{e^-} \tag{2–17}$$

with

$$E_0 = 0.98 - 0.059\mathrm{pH} \tag{2–18}$$

and

$$\mathrm{PtO} + \mathrm{H_2O} \rightarrow \mathrm{PtO_2} + 2\mathrm{H^+} + 2\mathrm{e^-} \tag{2–19}$$

with

$$E_0 = 1.05 - 0.059\mathrm{pH} \tag{2–20}$$

Pt dissolution in a the fuel cell conditions under potential cycle was investigated and the solubility of Pt was presented as a function of different factors such as temperature, pH, and oxygen partial pressure.[92] The dissolution reaction was found to be an exothermic reaction, and solubility of Pt increased with temperature. The solubility increase with decrease in pH and solubility significantly increases with presence of oxygen in atmosphere according to:

$$\mathrm{PtO} + \frac{1}{2}\mathrm{O_2} + 2\mathrm{H^+} + \mathrm{H_2O} \rightarrow \mathrm{Pt(OH)_3^+} \tag{2–21}$$

The finite solubility of Pt in acidic medium enables its movement into Nafion. The movement of Pt particles can be accomplished by diffusion, migration and possibly by convection.[93] Pt particles dissolve in catalyst layer and subsequent aggregated into bigger particles the process is govern by Ostwald ripening. Once particles have grown bigger (in micro-size) they can migrate by diffusion in catalyst layer and/or into membrane.[94] Inside the membrane, the movement can also be considered by convection mode. A mathematical model for Pt movement in membrane is illustrated based on dilute-solution theory though it has ignored several realistic factors such effect of double-layer charging, convection Brownian motion of Pt particles, and potential dependency on the charge movement.[95]

Several other researchers have advocated platinum oxidation and dissolution under normal the fuel cell operating conditions.[87, 96–98, 93, 90, 99] Experimental results have also confirmed coarsening of the Pt particles after 500 hours of operation.[100] The platinum oxidation and dissolution may result in decreases of electrochemically active surface area and have also attributed to metal catalyst cluster formation or/and loss of the catalyst support,[101] platinum dissolution and redepositing at the catalyst/electrolyte interface,[100] and migration of the platinum particles to the membrane interface.[94]

Pt concentration increases monotonically until 1.1 V due to formation of a protective film of PtO but after 1.1 V PtO can dissolve to form PtO_2 and so a decrease in Pt concentration is possible. It is also reported that this PtO has finite solubility that can diffuse leaving bare Pt for further formation of PtO.[97] Pt growth and aggregation is not found when Al was used as a catalyst support used instead of carbon. Carbon was proposed to help electron transfer between smaller and bigger particles of Pt which completes aggregation.[99] Pt was observed at catalyst-membrane interface due to migration of particles,[96] is also reported inside the membrane due to diffusion and redeposition. A band of Pt is reported inside the membrane. The location of the band can be calculated by equating fluxes of hydrogen and oxygen from respective electrodes which was further validated by SEM-TEM.[93]

Other factors such as corrosion of carbon support

$$\mathrm{C} + \mathrm{H_2O} \rightarrow \mathrm{CO_2} + 4\mathrm{H^+} + 4\mathrm{e^-} \tag{2–22}$$

may cause permanent loss of catalyst support, loss of catalytic activity, and, in extreme cases, a structural collapse of the electrolyte may lead to degradation of the fuel cell.[11] More details of carbon corrosion and corrosion products at different temperature can be found elsewhere.[102]

Silica is used as a gasket (seal) material to assemble the fuel cell. It was reported that silicon slowly leaches and deposits on the catalyst; however, it did not degrade the catalyst. The deposited Silicon was found to block oxygen transport due to its hydrophobicity.[103] Presence of traces of various gases as impurities in the fuel has also been reported to have a detrimental effect on the performance and lifetime of the fuel cell.[104]

2.4 Electrochemical Impedance Spectroscopy

Impedance spectroscopy is a very useful diagnostic tool because it is a non-invasive technique and can procure information about the processes inside the fuel cell. It is a powerful characterization technique which allows separating different processes occurring in the system depending on time constant of the process and could be used to study complex system like fuel cell. Impedance spectroscopy[105, 64, 106, 107] is often used to characterize processes in fuel cells. The impedance study has been reported to characterize solid oxide fuels cells (SOFCs)[108–113] and also to characterize methanol fuel cells.[114, 115] An extensive impedance investigation for PEMFCs has been reported in literature.

Springer *et al.*[64] have reported a typical impedance response of the cathode includes two arc, a high frequency arc reflecting the combination of an effective charge transfer resistance and a double-layer capacitance in the catalyst layer and a low-frequency arc reflecting mass-transport limitations within the backing layer. Cirreanu *et al.*[107] have conducted rigorous kinetics study for the fuel cell by the impedance techniques. Merida *et al.*[116] and Le Canut *et al.*[12] have described the use of impedance spectroscopy for fuel-cell diagnostics. Lee *et al.*[60] used impedance to evaluate the optimum Nafion loading in the catalyst active layer (CAL). Song *et al.*[61] used impedance to evaluate the optimal composition of the catalyst layer support material. Cha *et al.*[117] studied flooding of a micro flow channel. Effects of repetitive freezing of water residing in PEMFC, on the characteristics of the fuel cell were investigated by Cho.[118] Some research groups[119–123] have also used the impedance to characterize CO tolerance of the fuel cell. A descriptive review of literature related to impedance investigations of various aspects of the fuel cell is presented in Chapter 3

Application of this technique to fuel cells has been hampered because the experiments are difficult to perform and are prone to artifacts, and fundamental interpretation models are not available. The fuel cells are sensitive to anything inside the cell, so it is difficult to determine if data from instrumentation inside the cell is due to cell behavior or due to the artifact of instrument. The measurement model was used to analyze possible error in the impedance response of the fuel cell which is discussed in Chapter 4.

2.4.1 Measurement Model Analysis

The model was introduced as a means to resolve recurring issues in regression of impedance data, *e.g.,*[124–127]

1. identification of the most appropriate weighting strategy for regression,
2. assessment of the noise level in the measurement, and
3. identification of the frequency range unaffected by instrumental artifacts or non-stationary behavior.

The errors in an impedance measurement can be expressed in terms of the difference between the observed value $Z(\omega)$ and a model value $\widehat{Z}(\omega)$ as

$$\begin{aligned} \varepsilon_{\text{res}}(\omega) &= Z(\omega) - \widehat{Z}(\omega) \\ &= \varepsilon_{\text{fit}}(\omega) + \varepsilon_{\text{bias}}(\omega) + \varepsilon_{\text{stoch}}(\omega) \end{aligned} \tag{2–23}$$

where ε_{res} represents the residual error, $\varepsilon_{\text{fit}}(\omega)$ is the systematic error that can be attributed to inadequacies of the model, $\varepsilon_{\text{bias}}(\omega)$ represents the systematic experimental bias error that cannot be attributed to model inadequacies, and $\varepsilon_{\text{stoch}}(\omega)$ is the stochastic error with expectation $\mathbb{E}\left\{\varepsilon_{\text{stoch}}(\omega)\right\} = 0$.

A distinction is drawn, following Agarwal *et al.,*[124–126] between stochastic errors that are randomly distributed about a mean value of zero, errors caused by the lack of fit of a model, and experimental bias errors that are propagated through the model. The experimental bias errors, assumed to be those that cause lack of consistency with the Kramers-Kronig relations,[128–130] may be caused by nonstationarity or by instrumental artifacts. The problem of interpretation of impedance data is therefore defined to consist of two parts: one of identification of experimental errors, which includes assessment of consistency with the Kramers-Kronig relations, and one of fitting, which entails model identification, selection of weighting strategies, and examination of residual errors. The error analysis provides information that can be incorporated into regression of process models.

The measurement model method for distinguishing between bias and stochastic errors is based on using a generalized model as a filter for non-replicacy of impedance data. The measurement model is composed of a superposition of line-shapes which can be arbitrarily chosen subject to the constraint that the model satisfies the Kramers-Kronig relations. The model composed of Voigt elements in series with a solution resistance, *i.e.,*

$$Z = R_0 + \sum_{k=1}^{K} \frac{R_k}{1 + j\omega\tau_k} \tag{2–24}$$

has been shown to be a useful measurement model. With a sufficient number of parameters, the Voigt model was able to provide a statistically significant fit to a broad variety of impedance spectra.[124]

The measurement model is used first to filter lack of replication of repeated impedance scans. The statistics of the residual errors yields an estimate for the variance (or standard deviation) of stochastic measurement errors. This experimentally-determined variance is then used to weight subsequent regression of the measurement model to determine consistency with the Kramers-Kronig relations. If the data can be represented by a model that is itself consistent with the Kramers-Kronig relations, the data can be considered to be consistent. The concept of using a generalized measurement model to assess consistency with the Kramers-Kronig relations, first introduced by Agarwal *et al.,*[124,126,131] was also employed by Boukamp and Macdonald[132] and by Boukamp[133] using weighting strategies based on an assumed error structure. The experimental determination of the stochastic error structure as used here, however, allows formal quantification of the extent of agreement with the Kramers-Kronig relations.

Other transfer-function models can be used as a measurement model so long as they are consistent with the Kramers-Kronig relations. Shukla and Orazem have demonstrated that the stochastic error structure determined from replicated impedance measurements is independent of the type of measurement model used.[134] While the regressed parameters may not be associated unequivocally with a set of deterministic or theoretical parameters for a given system, the measurement model approach has been shown to represent adequately the impedance spectra obtained for a large variety of electrochemical systems.[124] Regardless of their interpretation, the measurement model representation can be used to filter and thus identify the non-stationary (drift) and high-frequency (noise) components contained in an impedance spectrum.

The measurement model has been applied in previous work to assess the error structure of a variety of systems including electrohydrodynamic impedance,[135] electrochemical impedance data for reduction of ferricyanide on a Pt rotating disk,[136] for corrosion of cast iron in Evian water,[137] for corrosion of aluminum in orange juice,[127] and for charging of electroactive polymers.[138]

2.4.2 Interpretation Model

Mathematical models are needed to interpret the impedance data, including the low-frequency inductive loops, in terms of physical processes. Gomadam *et al.*[139] have reported an exclusive review of important literature for different approaches to model the impedance response of the fuel cell and have also presented a concise comparison of continuum-mechanics-based and equivalent-circuit based approach modeling. The most quantitative of the impedance models reported in the literature have emphasized detailed treatment of the transport processes, but use of simple electrochemical mechanisms precluded prediction of the inductive loops. As the oxygen reduction reaction (ORR) at the cathode is the rate-determining step, most models emphasize the reaction kinetics at the cathode. The one-dimensional models proposed by Springer *et al.*[64,140] considered the cathode to be a thin film on agglomerated catalyst particles. They studied the role of water accumulation in the gas diffusion layer and oxygen diffusion in the gas phase. These models considered only a single-step irreversible ORR at the cathode. The impedance models by other researchers[141–143] also treated a single-step kinetics for the ORR.

Several models for the impedance response of PEM fuel cells have considered a more detailed reaction mechanism. The model developed by Eikerling and Kornyshev[19] considered a single-step ORR to be reversible at the cathode. Antoine *et al.*[144] has proposed an impedance model with a three-step ORR kinetics in acidic medium on platinum nanoparticles though reaction intermediates were unspecified and kinetics at the anode was not considered in their model. They explained that the low-frequency inductive loops were a result of the second relaxation of the adsorbed species involved in the different steps of the ORR. More recently, Wiezell *et al.*[145] considered a two-step hydrogen oxidation reaction (HOR) and have reported low-frequency inductive loops. They explained that the inductive loops were the result of changing factors such as water concentration, membrane thickness, hydrogen pressure and the HOR kinetics.

The role of intermediates in the ORR is supported by independent observation of hydrogen peroxide formation in PEM fuel cells.[7–9] A rotating-ring-disk-electrode study[77] revealed that formation of the peroxide on platinum particles supported on carbon (catalyst used in the fuel cell) is quite possible by two-electron reduction while the formation is not an option on clean bulk platinum. The hydrogen peroxide formed as an intermediate causes chemical degradation of the membrane.[9] Other reactions have also been reported which could potentially account for the low-frequency features observed in the impedance data. Platinum dissolution, for example, has been observed in PEM fuel cells[10] which can lead to the loss of catalytic activity and, consequently, to the degradation of the fuel cell performance.[88] Side reactions and the associated intermediates can degrade fuel cell components such as membranes and electrodes, thereby reducing the lifetime, one of the crucial issues in the commercialization of fuel cells.[146] The influence of side reactions and reaction intermediates on the impedance response is comparatively unexplored.

2.4.3 Flooding in the Fuel Cell

The performance of the fuel cell is influenced by kinetic limitations at low current densities, Ohmic limitations at intermediate current densities, and mass-transfer limitations at high current densities. Kulikovsky[147] and Berg *et al.*[148] have described in detail the critical role of water management in operation of the fuel cell. To maintain proton conductivity, the fuel cell membrane must remain hydrated. To achieve hydration, the relative humidity of inlet gasses is typically held at a large value. Water, however, is also a product of the cathodic reaction; thus, an excess of water in the cathode is commonly observed, which can lead to condensation and subsequent flooding. Flooding increases the resistance associated with the gas diffusion layer and may even block flow channels, reducing the availability of oxygen.[149] Condensed water may be removed by gas flow. Thus, changes in design of reactant flow channels and gas diffusion layers have been proposed to reduce the influence of flooding.

Pressure drop has been reported to provide a suitable diagnostic tool for monitoring flooding in the fuel cell.[150] Flooding was also investigated by correlating the appearance of flooding to the Faradaic resistance.[151] Barbir *et al.*[152] have investigated the relationship between pressure drop and cell resistance to make a distinction between flooding and drying. They observed that both pressure drop and cell resistance changed in case of drying; whereas, only pressure drop changed under flooding conditions. Ge *et al.*[153] observed that the anode flooding is mainly due to water-droplet condensation at channel walls in contrast to flooding at the cathode which is usually attributed to condensation in gas diffusion layer (GDL). They have also reported that use of a hydrophilic GDL and elevated anode plate temperature could mitigate anode flooding. The onset of flooding may be seen in steady-state measurements, but the impedance response is even more sensitive to appearance of flooding conditions. The impedance technique has recently been used to detect membrane drying, flooding, and anode poisoning of fuel cell stacks.[12] Merida *et al.*[116] have also investigated failure modes (drying and flooding) of the fuel cell using the impedance technique. The approach taken by LeCanut *et al.*[12] and Merida *et al.*[116] was to detect flooding by observing increases in the value of the impedance as compared to a normal impedance measured at the beginning of cell operation. The advantage of their approach is that a physical model is not needed. The difficulties with normalizing the impedance to the impedance measured at the beginning of cell operation are that steady-state operation will generally not be established during this measurement, that there may be other reasons for increases in cell impedance with time, and that flooding may already be taking place during the initial measurement.

Locally-resolved impedance spectroscopy and NMR imaging have been used to investigate flooding and drying in the fuel cell by Schneider *et al.*[154–156] The authors reported that, for co-flow configurations, membrane drying was evident near the gas inlet and flooding was severe near the gas outlet.[155] The authors have also reported that drying and flooding were more pronounced in co-flow as compared to counter-flow configurations.[156] Fouquet *et al.*[157] fitted a Randles-like equivalent circuit to impedance data and correlated circuit values to the state-of-health (flooding and drying) of the fuel cell. The Randles-like circuit, however, cannot account for all the phenomena taking place in the fuel cell. While there are differences in the specific approaches taken, the underlying concept for each of these approaches was that one can detect flooding by observing increases in the value of the impedance.

2.4.4 Evaluation of Interfacial Capacitance

Electrical circuits invoking Constant-Phase Elements (CPE) are often used to fit impedance data because the associated distribution of time constants provides an improved fit.[158–160] The distribution of time constants has been attributed to surface heterogeneity[161,162] or to continuously distributed time constants for charge-transfer reactions.[163–167] The CPE parameters may give insight into surface disorder and surface roughness,[168] electrode porosity,[169] and non-uniform potential and current distribution.[170,171]

Electrical circuits invoking CPEs have been used to model the impedance response of PEM fuel cells. Ciureanu *et al.*[106] used the impedance technique to study the oxidation of hydrogen and hydrogen-CO mixture in a fuel cell and fitted the result using CPE parameters. The effect of CO on the performance of the fuel cell has been reported by impedance technique and the impedance response has been fitted using CPE parameters to illustrate physical processes.[120] The CPE parameters have also been used to fit the impedance response of electrocatalysts for the anode of the fuel cell.[172] Meland *et al.*[173] studied effect of water on the anode reaction in the fuel cell by impedance and have fitted impedance response using the CPE parameters, have reported parameters as a function of operating potential. The CPE parameters have been used to model impedance study for characterizing different methods for catalytic ink preparation for the fuel cell.[174] The CPE approach has also been exploited to characterize carbon-nanotube-supported electrocatalyts for anodes,[175] to study anode materials for the solid oxide fuel cells,[176] and to model the impedance response of the porous anode of a methanol fuel cell.[177] The depressed semicircle seen in Nyquist plots has been attributed to non-homogeneity of electrode surface.[178] Fouquet *et al.*[157] have attempted to correlate parameters to the state-of-health (flooding and drying) of a PEM fuel cell though the parameters were again estimated by fitting impedance data. The interfacial capacitance was estimated employing graphical methods to interpret impedance response in term of physical processes such flooding and drying which is to be submitted as a technical article.[179]

CHAPTER 3
EXPERIMENTAL

Details of experimental methods and materials are described in this chapter. Impedance and polarization data collected on the fuel cell are presented and discussed. A concise review of literature related to experimental investigations of various aspects of the fuel cell such as reaction kinetics, transport mechanisms, performance and lifetime analysis has also been outlined.

3.1 Introduction

Impedance spectroscopy is often used to characterize processes in fuel cells, including PEM fuel cells.[64,105–108] Springer *et al.*[64] have reported a typical impedance response of the cathode for the fuel cell which includes two arcs, a high frequency arc reflecting the combination of an effective charge transfer resistance and a double-layer capacitance in the catalyst layer and a low-frequency arc reflecting mass-transport limitations within the backing layer. The straight-line portion in the high frequency arc is attributed to distributed ionic resistance and distributed capacitance in the catalyst layer. Paganin *et al.*[65] used impedance spectroscopy to study the effect of cell temperature, oxygen partial pressure, electrode composition, and membrane thickness on the fuel cell performance. Andreaus *et al.*[180] used impedance data obtained under high current densities to estimate performance losses in the fuel cell. They used membranes with different thickness and ionic density (equivalent weight) to prove that loop at low frequency in impedance response can also be due to anode drying out which lead to low proton mobility in addition to oxygen transport limited by flooding. Ciureanu[181] has examined the ohmic resistance of Nafion membranes as function of humidification conditions for low current density (0-400 mA /cm^2). For well-humidified cathode, they have reported that the resistance was small and relatively constant to the presence of the anodic humidification while for non-humidified cathodes the membrane resistance was high and strongly dependent on current and anodic humidification. Dehydration of the Nafion present in the cathode catalytic layer resulted in an increase of the polarization resistance in addition to the ohmic resistance of the membrane; the apparent deactivation of the cathode electrocatalyst appears to be due to a decrease of the electrochemically active surface area.

Lee *et al.*[60] used impedance to evaluate the optimum Nafion loading in the CAL. Song *et al.*[61] used impedance to evaluate the optimal composition of the catalyst support material. The study conducted by Hombrados *et al.*[182] has discussed impedance measurements for kinetics analysis of both the cathode and the anode reaction mechanisms. They have suggested a equivalent-circuit model to fit the impedance data, and have evaluated parameters such as membrane conductivity, and charge transfer resistance as a function of operating conditions like humidification temperature, and reactant flow rate. Three-step hydrogen kinetics consisting of diffusion-adsorption of hydrogen molecule, formation of proton, and proton hydration (combination of proton with water) is proposed by Meland *et al.*[173] They find the proton hydration as a rate-determining step at higher temperature where due to less amount of water time constant for this step becomes larger and therefore collapsed into high frequency arc. Abe *et al.*[183] used impedance to analyze the effect of humidity in the oxygen stream at the cathode of the fuel cell. Lefebvre *et al.*[58] have used the impedance to characterize proton-conducting and electron-conducting polymer particles for catalyst support for fuel cells. They evaluated catalytic activities of the catalyst support toward hydrogen and methanol oxidation and oxygen reduction in the fuel-cell-type gas diffusion electrodes. They have reported that the activities for oxygen reduction comparable to that obtained with a commercial carbon-supported catalyst were observed, whereas those for hydrogen and methanol oxidation were significantly inferior, although still high for prototype catalysts. The preparation and the fuel cell evaluation of sPSU based MEAs at varying temperatures was investigated by Kraemer *et al.*[184] They have reported that the MEA has low resistance though it showed mass transport limitations in the range of 600-800 mA/cm^2, most probably caused by abundant water due to the overhumidified measuring conditions.

Paganin *et al.*[65] have reported one arc and have explained the low-frequency arc has been superimposed on the higher-frequency arc. The overall impedance response has been explained as the effect of the double-layer capacitance and the charge transfer resistance of oxygen reduction reaction (ORR). Song *et al.*[61] have reported two capacitive loops for the impedance response of the fuel cell. Impedance response reported by Springer *et al.*[64] includes two arcs. The study conducted by Cirreanu *et al.*[185] has investigated the impedance response of the fuel cell with different cell voltage, humidification temperature of reactants, and airflow rate. They have reported impedance spectra with two loops: the high-frequency loop was attributed to the effect of reaction kinetics and oxygen transport in the CAL, and the low-frequency loop was attributed to mass transport limitations of gases and water in the GDL. The group has also suggested a circuit analog model to explain the experimental results and have calculated the parameters such as surface exchange current density and Tafel slopes. Many authors *e.g.,* Castanña *et al.*[186] and Li *et al.,*[62] reported only one capacitive loop. Castanna *et al.*[186] have reported an exponential decrease in the charge transfer resistance with increases in the overpotential. They also have reported the decreases in the double-layer capacitance with the increases in the overpotential and the capacitance reaches a constant value once the performance is controlled by ohmic effects. The higher value of the capacitance observed in the kinetics control region could be due to charging-discharging processes in the region.

Some research groups[119–123] have also used the impedance to characterize CO tolerance of the fuel cell. Jiang *et al.*[119] have reported the impedance study to characterize CO tolerance of electrocatalyst as a function of DC bias potential, temperature and relative humidity while Kim *et al.*[120] have used the impedance to investigate the effect of CO on the performance of the fuel cell and have reported that charge-transfer resistance as well as hydrogen dissociation resistance increase with an increase in the CO concentration but it has little effect on low frequency arc of the impedance spectra. Yang *et al.*[121] have applied a three-electrode arrangement to investigate effect of the CO on the fuel cell performance. They have reported that the overpotential of anode in presence of the CO increases due to increase in both charge-transfer resistance and ohmic resistance in the catalyst layer. Mazurek *et al.*[123] have conducted the impedance study to characterize the CO tolerance of carbon-supported Pt and carbon-supported Ru for the anode electrocatalyst. They have reported that the carbon-supported Ru catalyst have better catalytic activity than the Pt and also the smaller particle size of Ru better performance was observed.

The influence of carbon monoxide poisoning on the platinum and platinum-ruthenium anode was investigated by Wagner and Schulze[187] using the impedance spectroscopy. They found that the degradation of the fuel cell performance during the poisoning with CO was dominated by an increase of anodic charge transfer resistances and an increase of the finite diffusion impedance. They have also observed that impedance spectra exhibit pseudo-inductive contributions at the low frequency part of the spectra, which increase during the experiment. The increasing pseudo-inductive behavior has been explained because of a surface relaxation process due to the competitive oxidation of hydrogen and carbon monoxide at the anode. Cirreanu *et al.*[107] have conducted rigorous kinetics study for the fuel cell by the impedance techniques. They have also reported the effect of carbon monoxide on the anode kinetics, and the fuel cell performance. The influence of carbon monoxide poisoning on platinum and platinum-ruthenium anodes was investigated using impedance spectroscopy.[187, 188]

Impedance investigations have also been reported for different fuel cell applications such as studies of the effect of membrane thickness on the conductivity of the Nafion,[189] characterization of electrosprayed Nafion films,[190] performance evaluation of self-humidified composite membranes,[191] and characterization of single-walled carbon-nanotube-based proton exchange membrane assemblies for hydrogen fuel cells.[52] It has also been used to study ion exchange capacity of composite membranes for high temperature applications,[30]to determine conductivity of composite membranes for intermediate temperature fuel-cell applications,[34] to study the effect of temperature on resistance and proton conductivity of composite membranes,[35,36] to measure ionic and electronic resistibility of composite electrode catalyst for the fuel cell application.[37] Using the impedance, Li *et al.*[115] have investigated a reference electrode to resolve effects at the anode and cathode and within the membrane the fuel cell.

The object of this chapter is to provide a comprehensive analysis of performance of the fuel cell in terms of impedance and polarization results as a function of several factors. The factors analyzed include operating conditions such as current density, temperature, and backpressure, and design parameters such as flow channels, and GDLs. Brief of techniques, methods, and materials used is also presented.

3.2 Experimental

The experimental system and the impedance instrumentation used are presented in this section.

3.2.1 Materials and Chemicals

The MEA (purchased from Ion Power, Inc., New Castle, DE) employed 0.0508 mm (2 mils) thick Nafion N112 with catalyst layers of about 0.025 mm on both sides of the membrane. The active surface area was 5 cm^2. One more MEA with the same thickness of the membrane, and catalyst but embeded GDL both side of the catalyst layers was used which was supplied by fuelcellstore (San Diego, CA). The catalyst layers were platinum supported on carbon with a Pt catalyst loading of 0.4 mg/cm^2 on both the anode and the cathode sides. Two types of GDL were used during assembling the MEA. Both have an effective thickness of 0.284 mm, and were made of carbon cloth, but one was uniformly macro-porous while the other has variable porosity. The nonuniform GDL was micro-porous to the catalyst side and macro-porous to the channel side. Similar GDL structures have been reported in the literature.[64–66] The material of the flow channel (flow configurations are shown in Figure 3-1) used was made of graphite with the outlet lower than the inlet to facilitate removal of condensed water. Hydrogen gas was used as

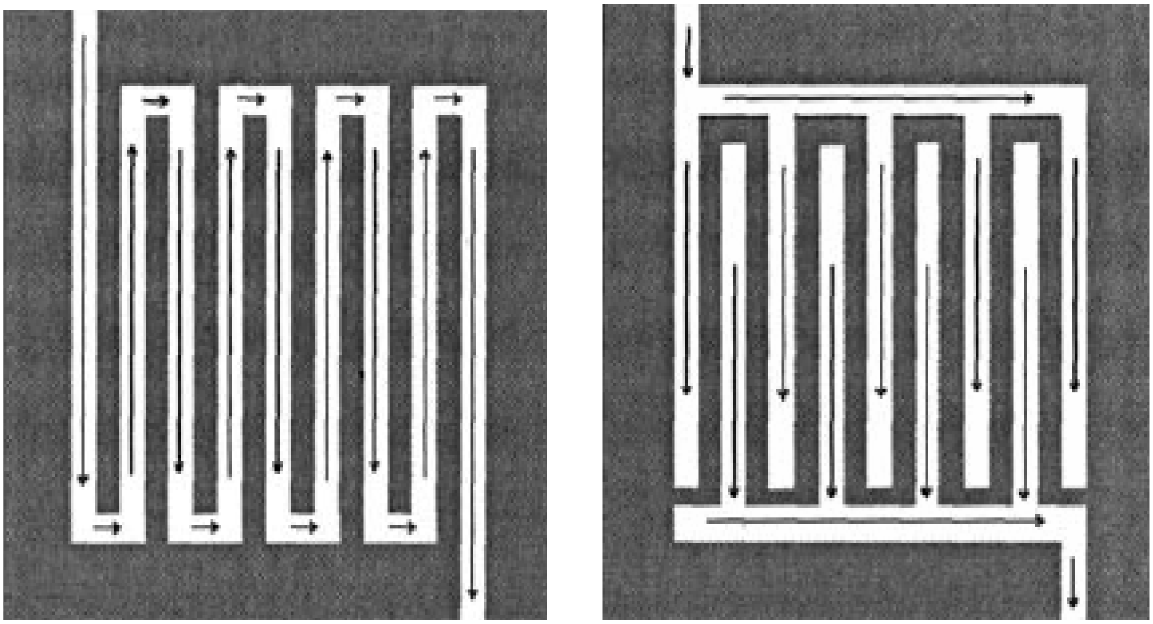

(a) (b)

Figure 3-1: The configurations of flow channels;[4] a) serpentine; and b) interdigitated.

fuel and compressed air was used as oxidant. Compressed N_2 was used for purging of the fuel cell before and after experiments. A Barnstead E-Pure Water System with an ion resistivity of 14.9 $M\Omega cm$ was used as a source of deionized water delivered to the anode and the cathode humidifiers.

An 850C fuel-cell test station (supplied by Scribner Associates, Southern Pines, NC) was used to control reactant flowrates and temperatures. The test station was connected to a computer by an interface for data acquisition. The gas flow to the anode was held at temperature of 40 ± 0.1 °C, and the gas flow to the the cathode was held at a temperature of 35 ± 0.1 °C. The gas flows were humidified to 100 percent relative humidity at the respective temperatures. The cell temperature was held at 40 ± 0.1 °C. The hydrogen flow rate was 0.1 liters/min and the air flow rate was 0.5 liters/min. The maximum stoichiometry for hydrogen and air was 1.5 and 2.5, respectively, and the cell was operated at the fully-humidified condition.

3.2.2 Electrochemical Impedance Measurements

Impedance measurements were performed using two different systems. The Scribner Associates 850C Fuel Cell Test Stand contains both an electronic load and a frequency response analyzer. Impedance measurements obtained with the 850C were compared to impedance collected using a Gamry Instruments FC350 impedance analyzer coupled with a Dynaload electronic load RBL 100V-60A-400W. All electrochemical measurements were performed with a two-electrode cell in which the anode was used as a pseudo-reference electrode.

The protocol recommended by Ramani *et al.*[192] was used to ensure that the system reached steady-state operation before impedance measurements were taken. The protocol consisted of two steps:

1. Upon startup, the current was swept from zero to the maximum value in forward and reverse directions until hysteresis in the polarization curve was no longer evident. This procedure was intended to ensure complete hydration of the MEA. This step required up to 48 hours (break-in time) for a new MEA and 1.5 hours for a system that had been recently used.
2. Once the hysteresis in the polarization curve was no longer evident, the current was set and the potential was monitored. Impedance measurements were conducted after the potential was stabilized. This step required 30 minutes.

The polarization curves were obtained by stepping the current from zero to the maximum current with an increment of 10 mA/30 sec. A typical polarization curves is presented in Figure 3-2.

Repeated impedance measurements were performed at several points on the polarization curve. The impedance measurements were conducted in galavanostatic mode for frequency range of 3 kHz to 1 mHz with a 10 mA peak-to-peak sinusoidal perturbation. The corresponding potential perturbation ranged from 0.04 mV at high frequency to 0.4 mV at low frequency. The frequencies were spaced in logarithmic progression with 10 points per frequency decade. Impedance scans were conducted in auto-integration mode with a minimum of 2 cycles per frequency measured. Each scan required 5 hours for the Scribner system and 3 hours for the Gamry system. The difference in time required can be attributed to differences in impedance settings. The long time required at lower frequencies made measurements at these frequencies susceptible to being influenced by nonstationary behavior.

3.2.3 Other Electrochemical Techniques

Linear sweep voltammetry (LSV)[31,32] was performed to measure the hydrogen crossover through the membrane. In this experiment, the fuel cell was polarized in a potential range of 0 to +0.4V in which all hydrogen present is assumed to be oxidized. The fuel-cell test station was used for basic control of flow rate and temperature of reactant gases, and the voltage scan was conducted with a Solaratron 1286 Potentiostat, which was coupled with the test station. The experiment was performed in the two-electrode configuration in which the anode was treated as a reference and the cathode was treated as a working electrode. inductively coupled plasma-mass spectroscopy (ICP-MS) was applied to estimate the platinum concentration[94] in the outlet water of the cathode of the fuel cell.

Cyclic voltammetry was conducted to evaluate the electrochemically active surface area[101,142,31] of the catalyst. The experimental setup discussed for the LSV was used for this experiment. In this experiment, the fuel cell potential was swept both in forward direction (0 to 0.8 V) and then in reverse direction (0.8 to 0 V). Results from these techniques relevant to this work is presented in Chapter 5.

3.2.4 Surface Analysis

Several microstructural characterizations techniques were employed to study the morphology, agglomeration, and oxidation state of elements in the catalyst and the membrane of the MEA. Details of techniques used are presented in following section though the results obtained are described in Chapter 5.

3.2.4.1 Scanning electron microscope

The surface characteristic of the MEA was studied with the scanning electron microscope (SEM).[101,31] For sample preparation, a small portion from the center of the both fresh and used MEA was cut with sharp razor and the SEM images were taken with the JOEL JSM 6400 available at MAIC in the University of Florida.

3.2.4.2 Transmission electron microscope

The TEM was used for atomic-scale micro-structural and chemical characterization of the MEA.[100,94,33] For sample preparation, a small portion from the center of the both fresh and used MEA was cut with sharp razor and was embedded on epoxy resin (Araldite 5002) for 48 hours at 60°C. Thin (90 nm) sections from the membrane-electrodes interfaces were cut with a diamond knife on Reichert OMU3 ultramicrotome at room temperature. The samples were mounted on Cu grid (mesh size 200) prior to TEM study. More details on sample preparation can be found elsewhere.[193] TEM study was performed with a JOEL JSM-2010F Field Emission Electron Microscope available at MAIC in the University of Florida, which is equipped with an energy dispersive spectrometer (EDS) for compositional analysis. The TEM micrographs were taken at 200 kV accelerating voltage for several magnifications in bright field mode (transmitted electrons).

3.2.4.3 X-ray photoelectron spectroscopy

The XPS was used to inspect possible elements and compounds at the surface (5-15 atomic layers) of the MEA. For sample preparation, a small portion (1cm X 1cm of thickness equivalent to MEA) from the center of the both fresh and used MEA was cut with sharp razor and the XPS scans were taken with the PHI 5100 ESCA system by Perkin-Elmer available at MAIC in the University of Florida. X-ray source was Mg anode with a work function 4.8 eV. The emitted electrons were collected at 45 ^{0} with respect to the sample. The sample was scanned at 300 watts power in energy range of 1000-0 eV (binding energy) with a step of 0.5 eV and 30 mSec/step. The survey (full scan) was generated at pass energy 89.45 eV whereas narrow scans (high resolution) for several

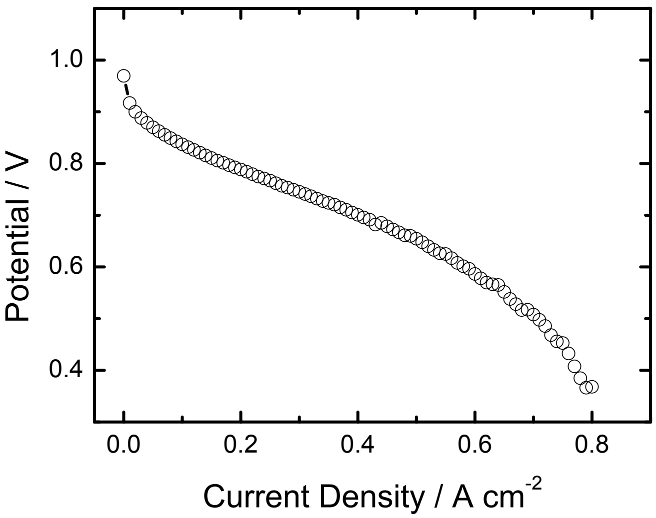

Figure 3-2: Polarization curves recorded with the 850C for an interdigitated channel as a function of current densities at the cell temperature 40 °C. The anode and the cell temperatures were set at 40 °C and the cathode temperature at 35 °C.

peaks were performed at pass energy of 22.36 eV. The atoms were assigned according to binding energy of visible peaks and atomic composition of elements were evaluated by relatives intensities of the peaks.

3.3 Results

Steady-state measurements (polarization curves) and impedance responses of the fuel cell are presented as a function of different operating parameters.

3.3.1 Current Density as a Parameter

Impedance measurements were performed at several points along the polarization curve presented in Figure 3-2. Two different trends in the impedance response were observed. As shown in Figure 3-3, the impedance decreased with increasing current density for low current density ($i < 0.5$ A/cm^2). As shown in Figure 3-3, the impedance increased with increasing current density for high current density ($i > 0.5$ A/cm^2). These trends are consistent with changes in the slope of the polarization curve with current density. It was found that the impedance was the lowest in case of intermediate current followed by the lower current and the impedance was found the highest at the higher current of the fuel cell, which was consistent with our previous findings.[194]

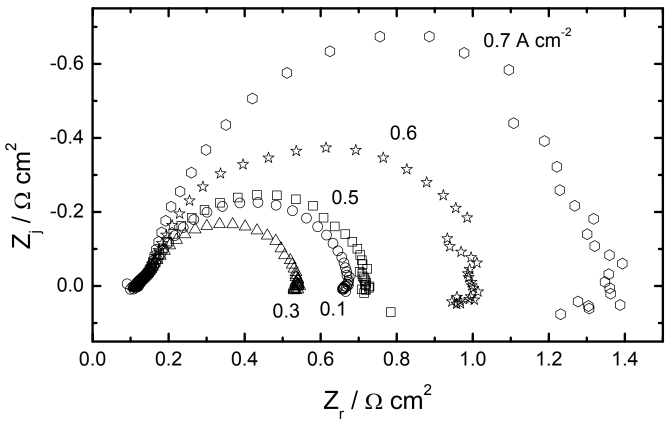

Figure 3-3: Impedance responses collected with the 850C for an interdigitated channel as a function of current densities at the cell temperature 40 °C. The anode and the cell temperatures were set at 40 °C and the cathode temperature at 35 °C.

3.3.2 Temperature as a Parameter

The performance of the fuel cell as function of the cell temperature with an interdigitated flow channel was investigated and is presented in Figure 3-4. An increase in the performance was observed with an increase in the cell temperature. Proton conductivity of the membrane increases with temperature, other transport properties such as diffusivity, electroosmotic coefficient also increase with temperature, which could enhance the performance at elevated temperatures.[3,195] The increase in the performance for the cell temperature is also explained as the enhanced reaction rate due to increased temperature.[4]

The impedance response decreased with the temperature as shown in Figure 3-5, which supported the better performance with an increase in the temperature.

3.3.3 Backpressure as a Parameter

Polarization curves and impedance measurements were obtained as functions of the backpressure applied on the anode and cathode. Polarization curves generated as a function of applied backpressure is presented in Figure 3-6(a). As evident in Figure 3-6(a), the effect of the BP can be especially discerned at higher current densities (mass-transfer region). It was observed that the performance improves by increasing BP from 30 to 40

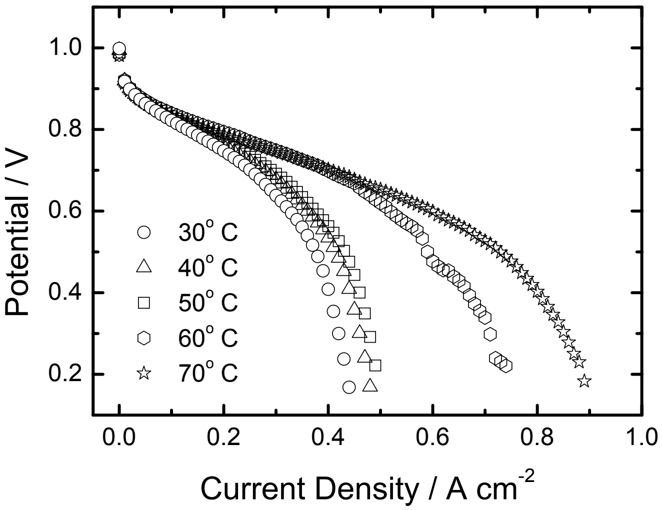

Figure 3-4: Polarization curves recorded as a function of cell temperature by the steady state measurement with the 850C for H_2 as reactant at the anode and air as oxidant at the cathode. The anode the cathode temperature at were fixed at 70 °C. The fuel cell was assembled with a serpentine channel.

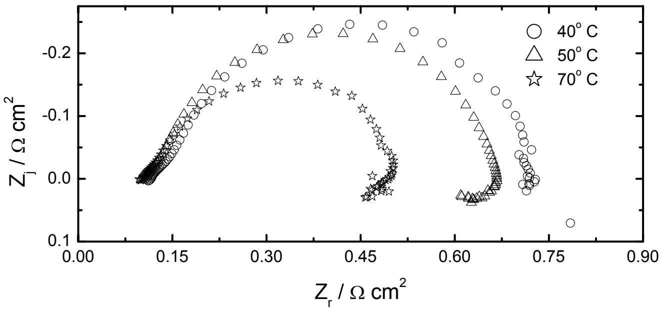

Figure 3-5: Impedance responses as a function of temperature at 0.5 A/cm^2 collected with the 850C with a serpentine channel.

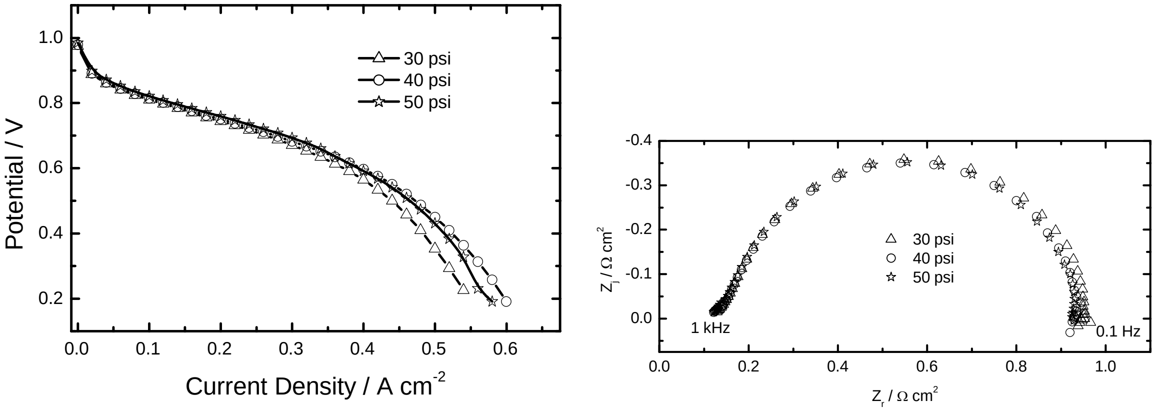

(a) (b)

Figure 3-6: Cell performance as a function of backpressure. The measurements were conducted with 850C for H_2 as reactant at the anode and air as oxidant at cathode. The anode reactant stream and cell temperatures were set at 60 ^{0}C and the cathode reactant stream temperature at 55 ^{0}C. The fuel cell was assembled with a serpentine channel; a) polarization curve generated from the steady-state measurement; and b) impedance response recorded at 0.1 A/cm^2.

psi, but when BP was increased further (from 40 to 50 psi) a decrease in the performance was recorded.

To explore further, the impedance responses as a function of applied backpressure were measured at several steady-state points on the polarization curve. Impedance response recorded at 0.1 A/cm^2, 0.2 A/cm^2, and 0.4 A/cm^2 are presented in Figures 3-6(b), 3-7(a), and 3-7(b) respectively. These current densities were chosen to be representative of the kinetic, ohmic, and mass-transfer controlled regions of the polarization curve. It was observed that the applied BP has no effect on the impedance response recorded in kinetic region (as seen in Figure 3-6(b)) but the impedance responses at other regions were affected by the applied backpressure. It was discerned that the impedance decreased (better performance) as the BP was increased from 30 to 40 psi but, as it was increased to 50 from 40, there was an increase in the impedance, which suggested that there could a optimum backpressure for cell performance. The effect of the BP was not observed in Ohmic region on the polarization curves, but, on the corresponding impedance spectra the effect was evident.

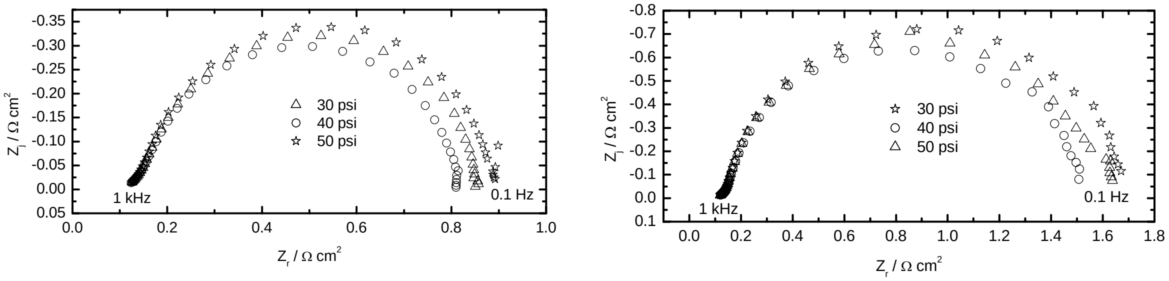

(a) (b)

Figure 3-7: Cell performance as a function of backpressure. The measurements were conducted with 850C for H_2 as reactant at the anode and air as oxidant at cathode. The anode reactant stream and cell temperatures were set at 60 ^{0}C and the cathode reactant stream temperature at 55 ^{0}C. The fuel cell was assembled with a serpentine channel; a) impedance response recorded at 0.2 A/cm^2; and b) impedance response recorded at 0.4 A/cm^2.

Backpressure concentrates reactants at the electrode, which could affect physical properties such as local surface tension leading to higher capillary rise and thus better transport of reactants.[196] However, at higher backpressure the performance would controlled by electrode kinetics resulting in no enhancement of cell performance. In addition, reactant crossover such as of hydrogen has been reported at enhanced backpressure,[197] which can reduce the performance of the cell.

3.3.4 Hysteresis Behavior and Impedance Response

Galvanodynamic curves were measured in forward and reverse directions. The forward and reverse directions of the resulting hysteresis curves are defined in the literature to be the water-imbibition and the water-drainage cycles, respectively.[198] A hysteresis curve obtained at 40 °C for a scan rate of 50 mA/30 s is presented in Figure 3-8(a). In the hysteresis curve, the forward and backward scan directions were not distinguishable for higher current densities due to multiple crossing of water-imbibition and water-drainage cycles. The multiple crossing of the two cycles could be attributed to random movement of water-droplets, which characterizes flooding to be a stochastic process. A zoomed picture of the flooding region (high current density) is shown in Figure 3-8(b).

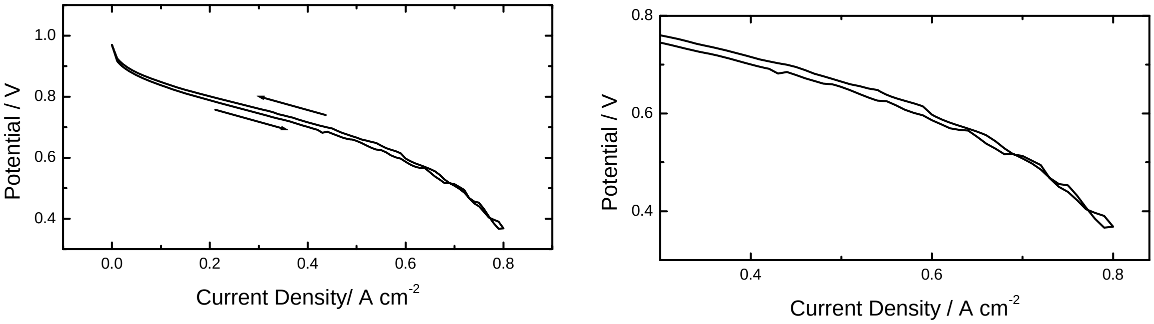

(a) (b)

Figure 3-8: Galvanodynamic curves recorded at a cell temperature of 40 °C using the 850C for H_2 as reactant at the anode and air as oxidant at the cathode: a) hysteresis curve for scan rate 50 mA/30 s; and b) the flooding region of the hysteresis curve.

Impedance response recorded for different current densities at 40 °C is presented in Figure 3-9. The low-frequency impedance response at higher current densities has significant scatter; whereas, the low-frequency impedance response at lower current densities has comparatively less scatter. The enhanced disturbance in the low-frequency impedance response at higher current densities may be attributed to stochastic processes such as flooding. The scatter in the high-frequency portion of the impedance spectra was unaffected by changes in current density. The size of the intermediate-frequency and the low-frequency arcs increased with increased current which could, as suggested in the literature,[12,157] be partially due to effect of flooding. Similar observations were recorded at other temperatures. Figure 3-10(a) shows a hysteresis curve obtained at 50 °C, and the corresponding impedance response is presented in Figure 3-10(b).

3.3.5 Time as a Parameter

The performance of the fuel cell was also investigated with time in term of polarization curves and impedance responses. As presented in Figure 3-11, the a sharp decrease in the current density was observed with time especially apparent in the ohmic and mass transport regimes of the polarization. Impedance response is presented in Figure 3-12, overall increase in the impedance was recorded and also the different features in the impedance spectra were observed.

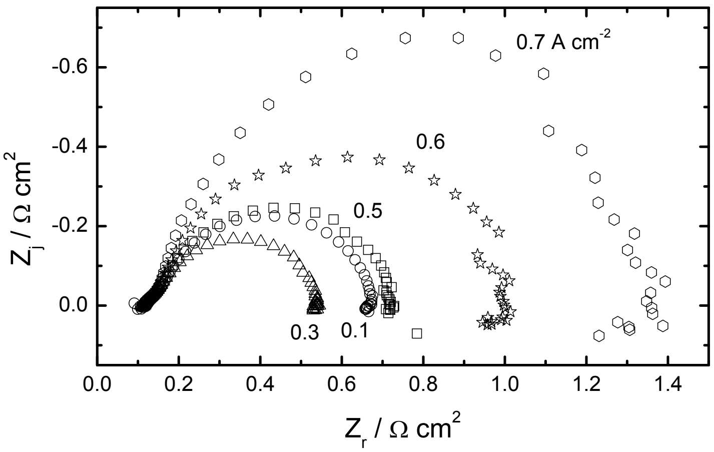

Figure 3-9: The measurement recorded with the 850C for H_2 as reactant at the anode and air as oxidant at the cathode. The anode, the cathode and cell temperatures were set at 40 °C; a) hysteresis curve for scan rate 50 mA/30 Sec.; and b) impedance responses as a function of current densities.

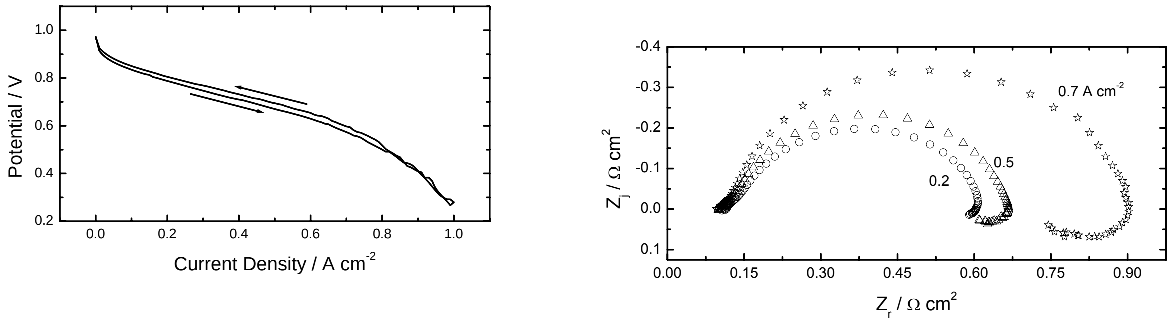

(a) (b)

Figure 3-10: The measurement recorded with the 850C for H_2 as reactant at the anode and air as oxidant at the cathode. The anode, the cathode and cell temperatures were set at 50 °C; a) hysteresis curve for scan rate 50 mA/30 Sec.; and b) impedance responses as a function of current densities.

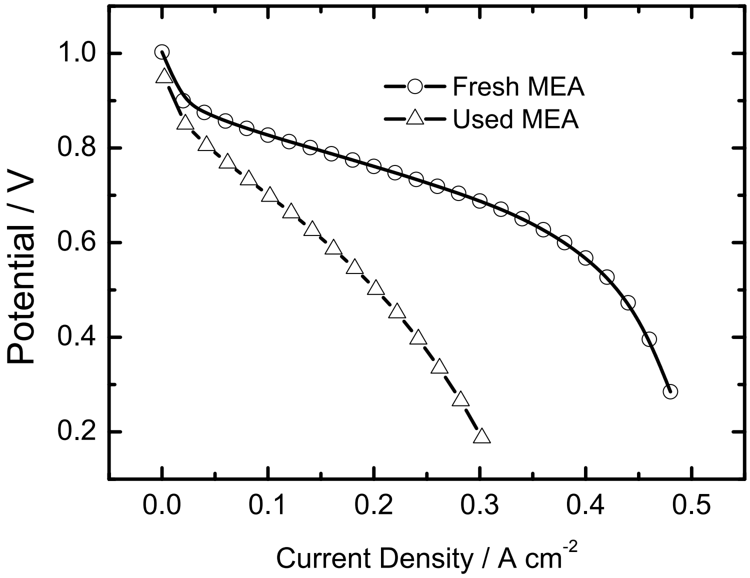

Figure 3-11: Polarization curve generated from the steady-state measurement as a function of time with 850C for H_2 as reactant at the anode and air as oxidant at cathode. The anode reactant stream and cell temperatures were set at 40 ^{0}C and the cathode reactant stream temperature at 35 ^{0}C. The fuel cell was assembled with a serpentine flow channel, and a uniform porous GDL.

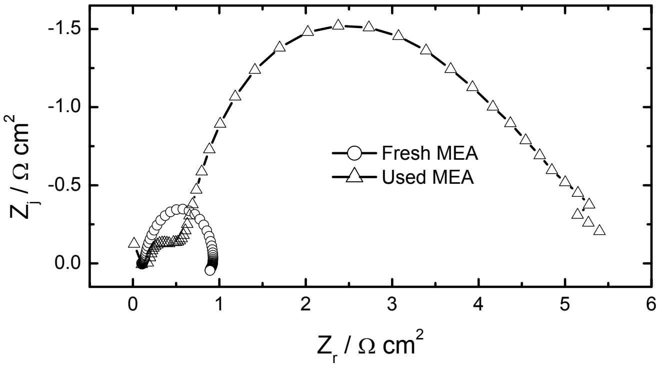

Figure 3-12: Impedance responses collected as a function of times a function of time with 850C for H_2 as reactant at the anode and air as oxidant at cathode. The anode reactant stream and cell temperatures were set at 40 ^{0}C and the cathode reactant stream temperature at 35 ^{0}C. The fuel cell was assembled with a serpentine flow channel, and a uniform porous GDL.

3.3.6 Flow Channel as a Parameter

The reactant flow channel design is one of the prominent factors that influences mass-transport. Condensed water may be removed by gas flow. Thus, changes in reactant flow channel design have been proposed to reduce the flooding. A comprehensive review of various flow-field designs developed by researchers and companies has been reported in the literature.[199] Several authors[149,200–205] have investigated performance of the fuel cell with different flow channels and have reported better performance in case of an interdigitated flow channel. Hsieh *et al.*[200] has reported better performance in case of an interdigitated channel as compared with a serpentine flow pattern in the fuel cell although they have proposed a new flow design. The better performance of the interdigitated flow channel was interrelated as a result of convective flow promoted by the interdigitated flow design which allowed a better utilization of catalyst.[201] The local concentration polarization due to non-uniform distribution of reactants in a parallel flow pattern is possible reason of less performance as compared to a serpentine channel in the fuel cell.[202] The theoretical study reported by Kazim *et al.*[206] has showed that the limiting current density of the fuel cell with an interdigitated flow field was about three times the current density with a conventional flow field.

In spite of the fact that the interdigitated flow field performs better, very limited experimental studies have been published. Wang *et al.*[4] has presented a systematic experimental study on the performance of the fuel cell with an interdigitated flow field by investigating the effect of cell temperature, gas humidification, operating pressure and reactant gas flow rates. The interdigitated flow field has advantage of convective transport in addition of the diffusive and capillary transport in the conventional flow fields though the pressure drop created between non-interconnecting inlet and outlet, promotes flooding[149] because the pressure in downstream is low, which pose difficulty in removing water. There have been several theoretical studies[73,74,150,207] published to address the

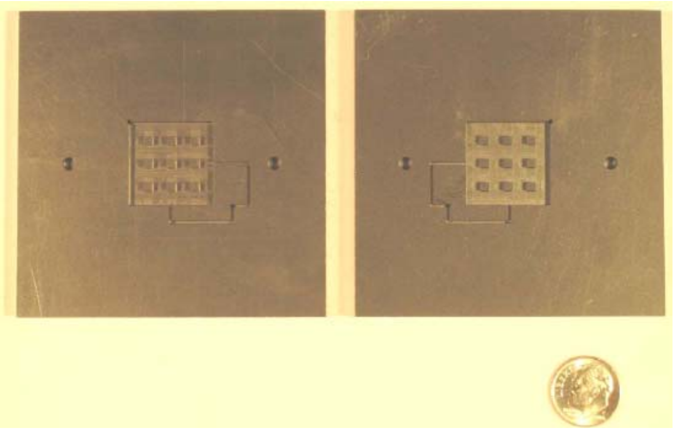

Figure 3-13: The configuration of the post flow channel.

problem of flooding in the interdigitated flow field though no experimental study has been reported.

The performance of two conventional channels in term of polarization curves and impedance spectra is presented in this section. In addition, a post flow channel design, (shown in Figure 3-14) was proposed and performance of the new channel was compared with the conventional channel. The polarization curves obtained for two channels from steady-state measurement on the fuel cell is presented in Figure 3-14. The limiting current obtained in the interdigitated flow channel was about double of the current obtained for the serpentine flow channel, which confirmed the interdigitated channel better performer. This observation was consistent with the reported literature.[201,206] The impedance response obtained for two channels in the fuel cell is presented in Figure 3-15. The impedance spectra have general form consisted of one high-frequency capacitive loop and one incomplete low-frequency inductive loop. The impedance in case of the interdigitated flow channel was found a lot less than the serpentine flow channel for same operating conditions.

The performance of the post channel was compared with the interdigitated channel for similar conditions. A comparison of polarization curves are presented in Figure 3-16. As seen in this figure, the open-circuit potentials were comparable in both channels; however, a reduced performance was noticed in both Ohmic and mass transfer regimes of

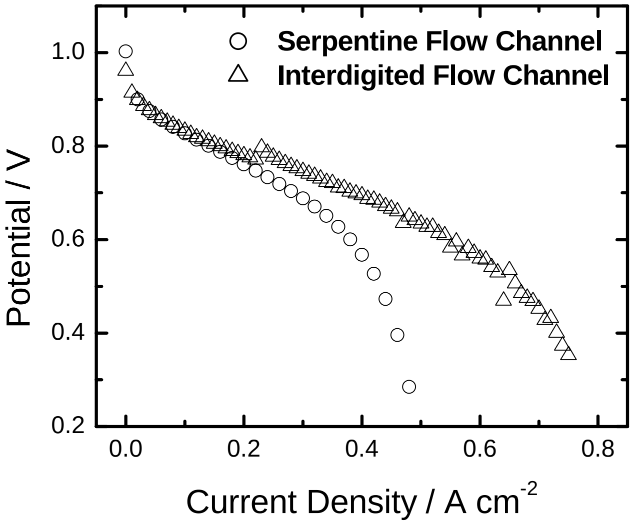

Figure 3-14: Polarization curves generated for two flow channels from the steady-state measurement with the 850C for H_2 as reactant at the anode and air as oxidant at the cathode. The anode and cell temperatures were set at 40 °C and the cathode temperature at 35 °C. The fuel cell was assembled with a uniform porous GDL.

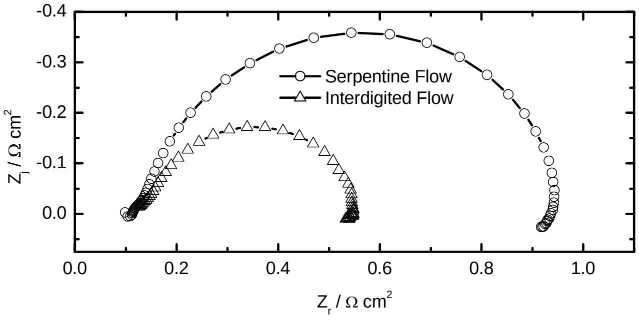

Figure 3-15: Impedance responses collected with the 850C for two flow channels with the 850C for H_2 as reactant at the anode and air as oxidant at the cathode. The anode and cell temperatures were set at 40 °C and the cathode temperature at 35 °C. The fuel cell was assembled with a uniform porous GDL.

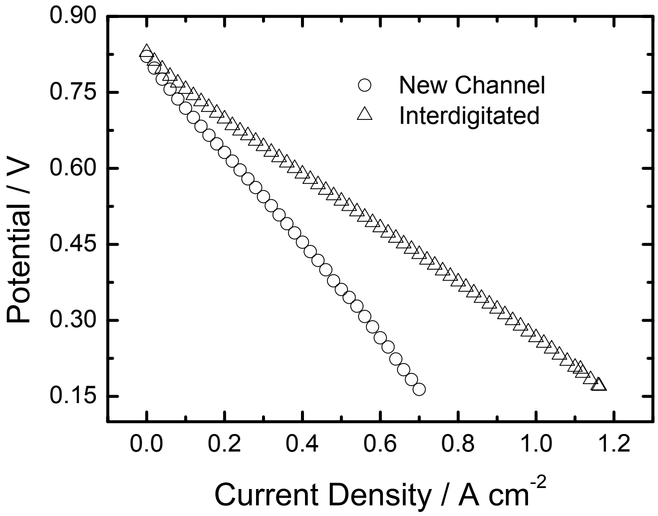

Figure 3-16: Polarization curves generated for the new and a conventional flow channels from the steady-state measurement with the 850C for H_2 as reactant at the anode and air as oxidant at the cathode. The anode and cell temperatures were set at 40 °C and the cathode temperature at 35 °C. The fuel cell was assembled with a uniform porous GDL.

polarization curve of the new channel. Lower performance in theses two regimes could be ascribed to poor contact and water management issues in the new channel.

The impedance response of the new channel was also compared as presented in Figure 3-17(b) for two channels. Higher high-frequency response (HFR) was registered in impedance response of the new channel which could be imputed to higher contact resistance in the new channel. Impedance response for current densities as parameter was also collected for the new channel which is presented in Figure 3-17(a). It was observed that impedance response especially at high current densities have exhibited much more scattering. The scattering was much pronounced at low frequency portion which could be possible consequences of water management issues i.e., flooding.

Based on investigations, it was concluded that the new channel design was worse than the conventional channel in terms of performance, though the design may be treated as a pseudo-1D channel. The following issues could have limited the performance of the new channel:

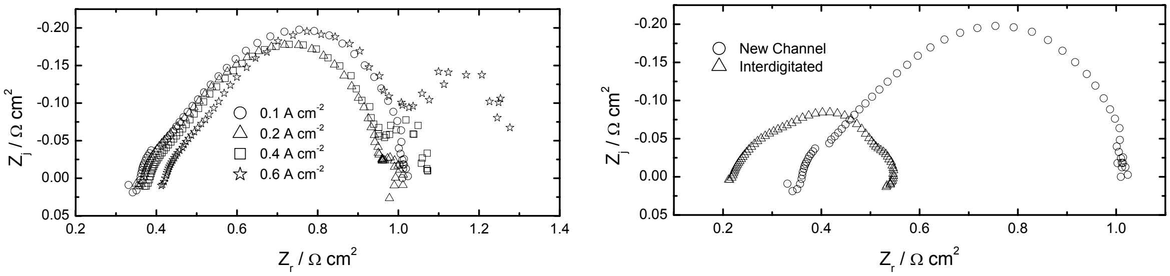

(a) (b)

Figure 3-17: Impedance response of the new flow channel with 850C for H_2 as reactant at the anode and air as oxidant at cathode. The anode and the cell temperatures were set at 50 °C and the cathode temperature at 45 °C. The fuel cell was assembled with a uniform porous GDL; a) impedance response generated for the new channel as a function of current density; and b) impedance response recorded at 0.4 A/cm^2 for the two channels.

1. Contact resistance: The higher HFR manifested in impedance response of the new channel could be ascribed to poor contact between the channel and the MEA.

2. Mass transport limitation: The low limiting current observed using the post channel may be attributed to poor water management.

3. Flooding: Excessive noise discerned in the impedance response at higher current densities could be attributed to stochastic processes such as flooding.

CHAPTER 4
ERROR ANALYSIS OF IMPEDANCE RESPONSE

The measurement-model-based error structure analysis of impedance data is presented in this chapter.

4.1 Introduction

Impedance spectroscopy is often used to characterize processes in fuel cells, including PEM fuel cells.[105,64,106–108] Low-frequency inductive features[144,208,209] are commonly seen in impedance spectra for the fuel cell (see, for example, Figure 3 reported by Makharia *et al.*[208]). Makharia*et al.*[208] suggested that side reactions and intermediates involved in the fuel cell operation can be possible causes of the inductive loop seen at low frequency. However, such low-frequency inductive loops could also be attributed to non-stationary behavior, or, due to the time required to make measurements at low frequencies, non-stationary behavior could influence the shapes of the low-frequency features. Impedance spectra typically exhibit inductive features at high frequency, and some authors report inductive loops at low frequencies. The high-frequency inductive features are understood to be caused by instrument artifacts, but the interpretation of the low-frequency inductive loops is less clear. While the low-frequency loops have been tentatively attributed to side reactions,[146] they could also be caused or influenced by nonstationary phenomena. The objective of this part of the work was to use the measurement model concept[124–127] to assess the error structure of the impedance measurements taken for the fuel cell.

A recent impedance study reported by Makharia *et al.*[208] revealed a capacitive loop at intermediate frequencies and an inductive loop at low frequency. The capacitive loop was attributed to the response of electrochemical reactions occurring in the fuel cell, and the inductive loops were tentatively attributed to side reactions and relaxation of associated reaction intermediates. Their interpretation is consistent with that suggested by Antoine *et al.*,[144] who proposed the presence of unspecified reaction intermediates. They suggested that low-frequency inductive loops were a result of the relaxation of adsorbed species involved in different steps of the oxygen reduction reaction. More

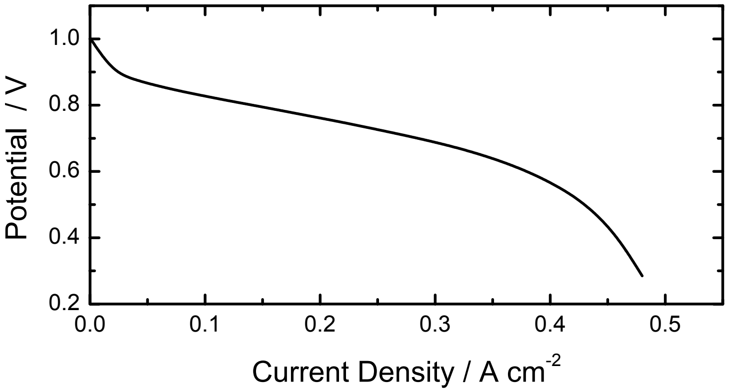

Figure 4-1: Polarization curve generated from the steady-state measurement with 850C for H_2 as reactant at the anode and air as oxidant at cathode. The anode reactant stream and cell temperatures were set at 40 ^{0}C and the cathode reactant stream temperature at 35 ^{0}C.

recently, Wiezell *et al.*[145] considered a two-step hydrogen oxidation reaction and reported low-frequency inductive loops. They have explained that the inductive loops were the result of changing different factors such as water concentration, membrane thickness, hydrogen pressure and the hydrogen oxidation kinetics. The influence of carbon monoxide poisoning on platinum and platinum-ruthenium anodes was investigated using impedance spectroscopy.[187,188] The reported impedance response exhibited low frequency pseudo-inductive behavior which was attributed to a surface relaxation process of competitive oxidation of hydrogen and carbon monoxide at the anode.

The inductive loops reported in the literature are typically seen at very low frequencies, *e.g.,* 1 mHz, at which system stationarity must be questioned. The objective of this work was to use the measurement model developed by Agarwal *et al.*[124–127] to determine whether the low-frequency inductive loops were due to or influenced by non-stationary behavior.

The time required to make the measurement at each frequency is shown in Figure 4-2. The long time required at lower frequencies made measurements at these frequencies susceptible to being influenced by nonstationary behavior.

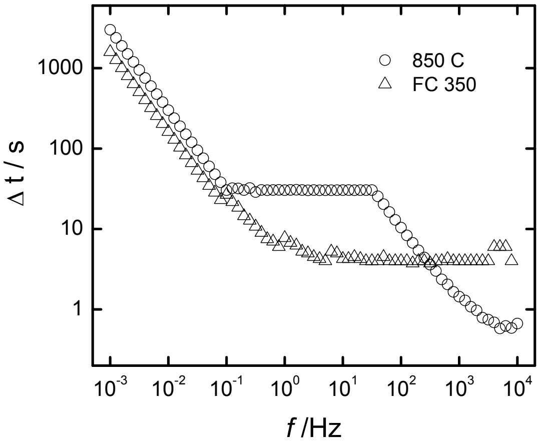

Figure 4-2: The average time required for impedance measurement at each frequency. The error bars associated with the standard deviation obtained from four experiments is smaller than the symbols used in the figure.

4.2 Results

Representative impedance scans and error analysis are presented in this section. The stochastic error structure obtained from replicated measurements was used to weight subsequent regressions to assess consistency with the Kramers-Kronig relations. The experimentally-determined stochastic error structure was also used to assess the quality of the regressions and to calculate the confidence interval for model predictions.

The error analysis procedure described by Agarwal *et al.*[124–126] was applied to sets of repeated impedance spectra. The procedure is illustrated in the subsequent sections for five repeated impedance spectra, shown in Figure 4-3, collected at a current density of 0.2 A/cm^2 with the FC350.

4.2.1 Evaluation of Stochastic Errors

Following the procedure described by Agarwal *et al.*,[125] the measurement model explained in equation (2–24) was fitted to each spectrum shown in Figure 4-3 using a frequency-independent weighting. The number of parameters was constrained by the need to have the same number of parameters for each spectrum and the requirement that no parameter had a $\pm 2\sigma$ (95.4 percent) confidence interval that included zero. Typically, 6 Voigt elements could be regressed to a spectrum. The standard deviation of the residual

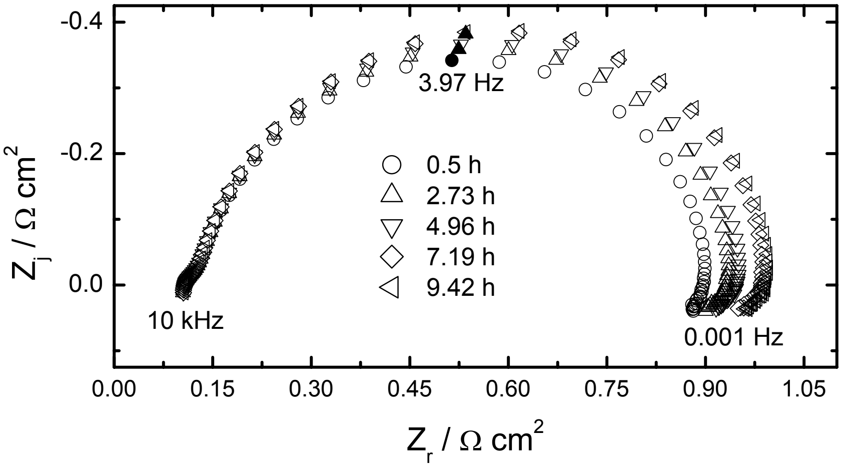

Figure 4-3: Five scans of impedance data collected at a current density of 0.2 A/cm^2 with the FC350.

errors was used as an estimate for the standard deviation of the stochastic measurement errors. The same procedure was applied to impedance measurements collected using the Scribner 850C. The results are presented in Figure 4-4(a). Here, the comparison of results of the error analysis is based on the impedance data collected at 0.2 A/cm^2 for both the 850C and the FC350.

The level of stochastic errors was very similar for the impedance collected using the Gamry FC350 and the Scribner 850C. Standard deviations normalized by the modulus of the impedance are presented in Figure 4-4(b). As shown in Figure 4-4(b), the noise level of the measurements varied with frequency but was generally less than 0.3 percent of the modulus.

A similar procedure was applied to determine the structure of stochastic errors in impedance measurements collected at different currents along the polarization curve. For a given system, an error structure model could be determined following the general model described by Orazem *et al.*,[210] *i.e.*,

$$\sigma_r = \sigma_j = \alpha|Z_j| + \beta|Z_r| + \frac{\gamma|Z|^2}{R_m} + \delta \tag{4–1}$$

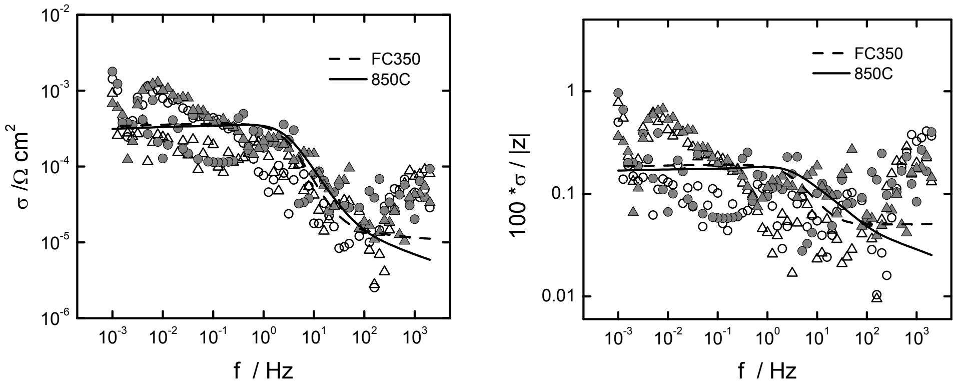

(a)

(b)

Figure 4-4: Comparison of error structures for the FC350 (filled symbols) and the 850C. The ○ represents the standard deviation of the real part of the impedance, and the △ represents the imaginary part of the impedance. The dashed and solid lines represents the empirical model of the error structure given by equation 4–1. a) standard deviations in units of impedance; and b) standard deviations normalized by the modulus of the impedance.

where R_m is the current measuring resistor corresponding to a given current range and α, β, γ, and δ are constants determined for a given instrument and set of measurement parameters. For the Gamry FC350, all adjusted parameters were equal to zero with the exception of $\gamma = 0.679$. For the Scribner 850C, all adjusted parameters were equal to zero with the exception of $\alpha = 0.00213$ and $\gamma = 0.679$. Lines corresponding to equation (4–1) are given in Figures 4-4(a) and 4-4(b). Equation (4–1) was used to weight subsequent regressions to assess consistency with the Kramers-Kronig relations.

4.2.2 Evaluation of High-Frequency Bias Errors

In principle a complex fit of the measurement model could be used to assess the consistency of impedance data. Sequential regression to either the real or the imaginary parts was shown to provide greater sensitivity to lack of consistency.[126] The measurement model approach developed by Agarwal *et al.*[126] was used to assess the consistency of high-frequency data with the Kramers-Kronig relations. The Voigt model was fitted to the real part of the measurement with a weighting based on the experimentally determined stochastic error structure. The parameters so obtained were then used to predict the

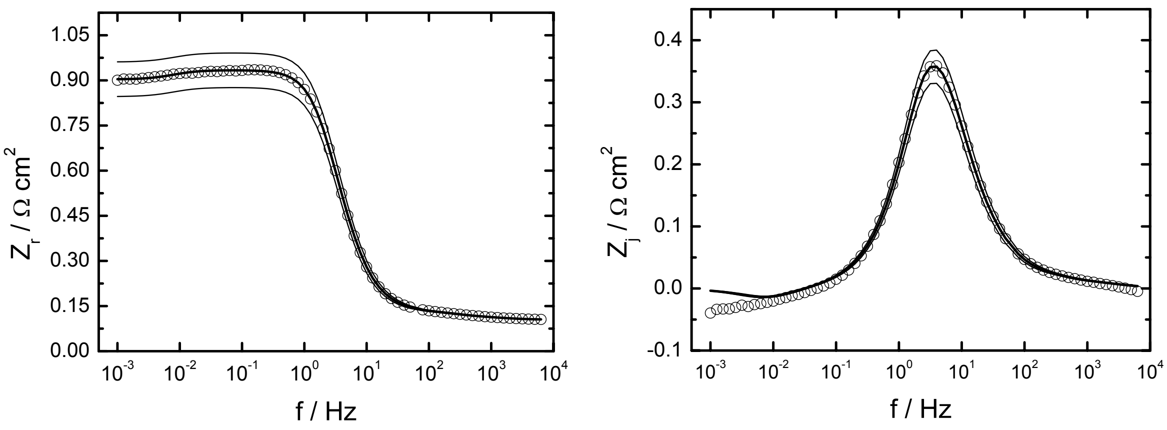

(a) (b)

Figure 4-5: Regression of the Voigt model to the real part of the impedance corresponding to the second of five scans given in Figure 4-3: a) fit to the real part of the measurement; and b) prediction of the imaginary part. The ∘ represents the experimental data, the heavy solid line represents the measurement model fit, and the thin solid lines represent confidence intervals.

imaginary part of the measurement, and a confidence interval for the prediction was calculated based on the estimated confidence intervals for the regressed parameters. Data that fell outside of the confidence interval were deemed to be inconsistent with the Kramers-Kronig relations.

This process is illustrated in Figure 4-5 for the second impedance scan shown in Figure 4-3. The fit to the real part of the impedance is given in Figure 4-5(a) where the thin solid lines represent the confidence interval for the regression. The prediction of the imaginary part of the measurement is given in Figure 4-5(b). The prediction of the imaginary part of the impedance is excellent at intermediate frequencies, but a discrepancy is seen in Figure 4-5(b) at both high and low frequencies. Regression to the real part of the impedance generally provides fewer parameters than does regression to the imaginary part. For this reason, the discrepancy seen at low frequencies was not considered to be significant.[126] The discrepancy at high frequency is seen where the real part of the impedance approaches asymptotically a finite value corresponding to a solution resistance.

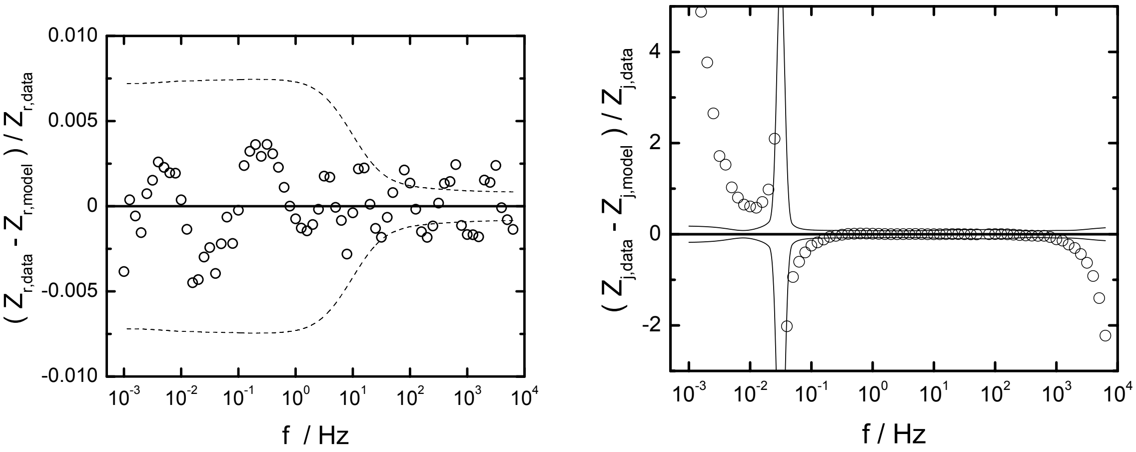

(a)

(b)

Figure 4-6: Normalized residual errors for the regression presented in Figure 4-5: a) fit to the real part, where dashed lines represent the $\pm 2\sigma$ bound for the stochastic error; and b) prediction of the imaginary part, where solid lines represent the 95.4% confidence intervals for the model obtained by Monte Carlo simulations.

The discrepancy is seen more clearly in the plots of normalized residual error, given in Figure 4-6(a) for the fitting errors and in Figure 4-6(b) for the prediction errors. The normalization by the experimental value of the impedance causes the confidence-interval lines shown in Figure 4-6(b) to tend toward $\pm\infty$ at the point where the imaginary impedance changes sign. The analysis shows that the nine highest frequencies fell outside the 95.4 percent confidence interval. These data were removed from the regression set. The conclusion that these points were inconsistent with the Kramers-Kronig relations is supported by the observation that the number of parameters that could be obtained from a complex regression increased when the high-frequency data were removed. In other words, deletion of data that were strongly influenced by bias errors increased the amount of information that could be extracted from the data. The bias in the complete data set induced correlation in the model parameters which reduced the number of parameters which could be identified. Removal of the biased data resulted in a better conditioned data set that enables reliable identification of a larger set of parameters.[126]

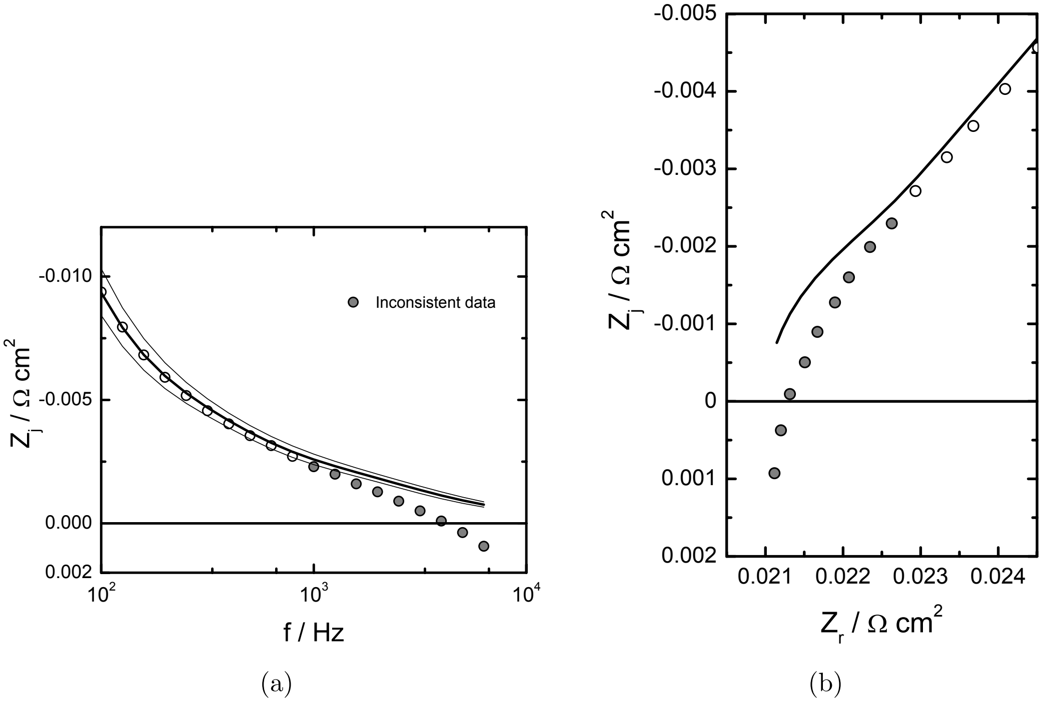

Figure 4-7: Detailed representation of impedance data showing the inconsistency observed at high frequency: a) expanded view of Figure 4-5(b); b) expanded view of a Nyquist representation (see Figure 4-3 for a complete spectrum). The filled symbols correspond to data that were deemed inconsistent with the Kramers-Kronig relations.

A similar analysis was performed for the first and second measurements obtained by both the FC350 and the 850C instruments. For all measurements, data measured at frequencies above 1000 Hz were found to be inconsistent with the Kramers-Kronig relations. These data were removed from the data used in subsequent regressions.

It is important to note that removal of data for which the imaginary impedance had a positive value was not sufficient to eliminate inconsistency with the Kramers-Kronig relations. As shown in Figure 4-7(a), the influence of the artifact extended well into the domain in which the imaginary impedance had a negative value. The filled symbols in Figure 4-7(a) correspond to data that were deemed inconsistent with the Kramers-Kronig relations. The result may be seen as well in the Nyquist plot given as Figure 4-7(b).

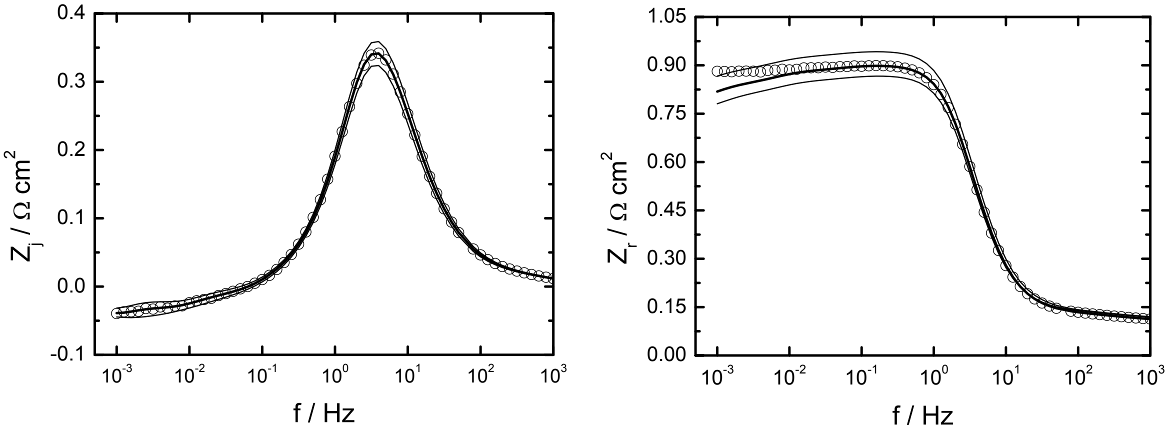

(a) (b)

Figure 4-8: Regression of the Voigt model to the imaginary part of the impedance corresponding to the first of five scans given in Figure 4-3: a) fit to the imaginary part of the measurement; and b) prediction of the real part. The ∘ represents the experimental data, the heavy solid line represents the measurement model fit, and the thin solid lines represent confidence intervals.

4.2.3 Evaluation of Low-Frequency Bias Errors

To test the consistency of the impedance data at low frequency, the imaginary part of the impedance data was fitted using a weighting strategy based on the empirical model for error structure given as equation (4–1). The parameter set so identified was used to predict the real part of the impedance. The confidence interval for the prediction was obtained by a Monte Carlo simulation based on the confidence interval of the regressed parameters. The procedure is described by Awarwal *et al.*[126]

The Voigt measurement model was regressed to the imaginary part of the impedance data corresponding to the first scan of the impedance data presented in Figure 4-3. The results, given in Figure 4-8(a), show that the measurement model could provide an excellent fit to the imaginary part of the data, even at the low frequencies that revealed inductive loops, characterized by positive values of imaginary impedance. The parameter values obtained from regression to the imaginary part of the impedance were used to predict the real part, as shown in Figure 4-8(b). The solid lines shown in Figure 4-8(b) represent the upper and lower bounds of the 95.4 percent (2σ) confidence interval obtained

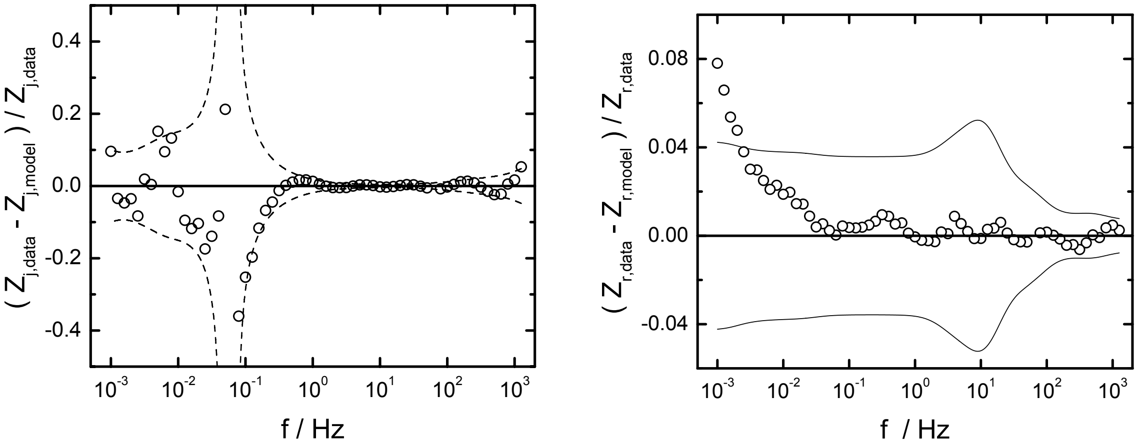

(a)

(b)

Figure 4-9: Normalized residual errors for the regression presented in Figure 4-8: a) fit to the imaginary part, where dashed lines represent the ±2σ bound for the stochastic error; and b) prediction of the real part, where solid lines represent the 95.4% confidence intervals for the model obtained by Monte Carlo simulations.

for the model prediction. The low-frequency data that are outside the confidence interval can therefore be considered inconsistent with the Kramers-Kronig relations.

A more precise view of the regression quality and the level of agreement with the predicted values can be seen in plots of residual errors. The normalized residual error for the regression to the imaginary part of the impedance is shown in Figure 4-9(a) where the dashed lines indicate upper and lower bounds for the stochastic noise level for the measurement. The dashed lines were calculated as $\pm 2\sigma$ where σ was obtained from equation (4–1). The normalization by the experimental value of the impedance causes the dashed lines to tend toward $\pm\infty$ at the point where the imaginary impedance changes sign. The quality of the regression is indicated by the observation that the residual errors for the regression fall within the noise level of the experiment. The normalized residual errors for the predicted real value are shown in Figure 4-9(b), where the solid line represents the upper and lower bounds of the 95.4 percent (2σ) confidence interval obtained for the model prediction. A lack of agreement between predicted and experimental values is seen for frequencies below 0.05 Hz. The data for the four lowest

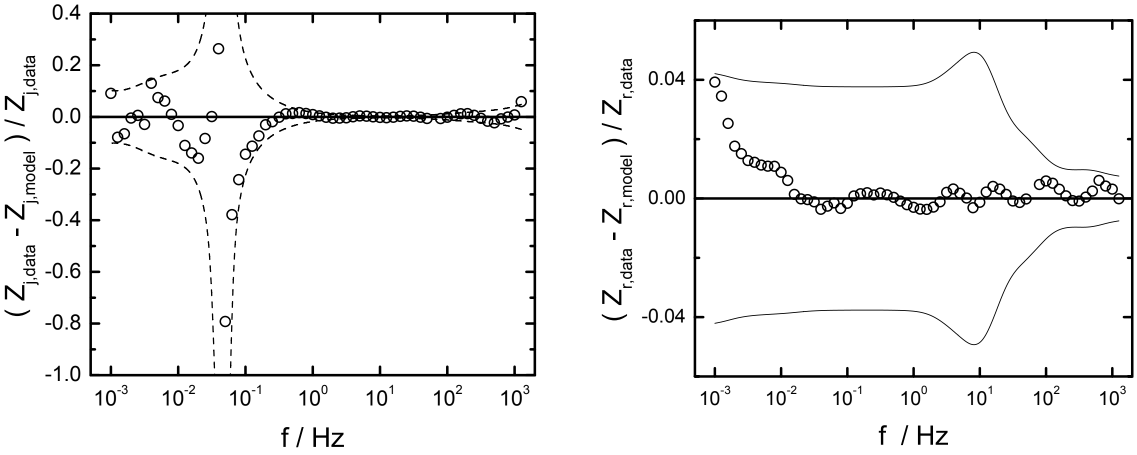

(a)

(b)

Figure 4-10: Normalized residual errors for the fit of the measurement model to the second scan of impedance data presented in Figure 4-3: a) fit to the imaginary part, where dashed lines represent the $\pm 2\sigma$ bound for the stochastic error; and b) prediction of the real part, where solid lines represent the 95.4% confidence intervals for the model obtained by Monte Carlo simulations.

frequencies are seen to fall outside the confidence interval for the prediction. These points can be described as being inconsistent with the Kramers-Kronig relations.

Similar bias error analyses were performed for subsequent impedance scans. Figure 4-10(a), for example, shows the normalized residual error for the imaginary part of the second scan, and the Figure 4-10(b) shows associated predicted error in the real part of the second scan. The agreement between predicted and experimental values is better for the second scan, shown in Figure 4-10(b), than for the first, shown in Figure 4-9(b). All data shown in Figure 4-10(b) fall inside the 95.4 percent confidence interval for the prediction. The second and subsequent scans were found to be consistent with the Kramers-Kronig relations.

The measurement model was also used to test the impedance data collected with the 850C for consistency with the Kramers-Kronig relations. In this case as well, some low-frequency data were found to be inconsistent with the Kramers-Kronig relations for the first of a series of repeated measurements. All data in the second and subsequent scans were found to be consistent with the Kramer-Kronig relations. The fit of the Voigt

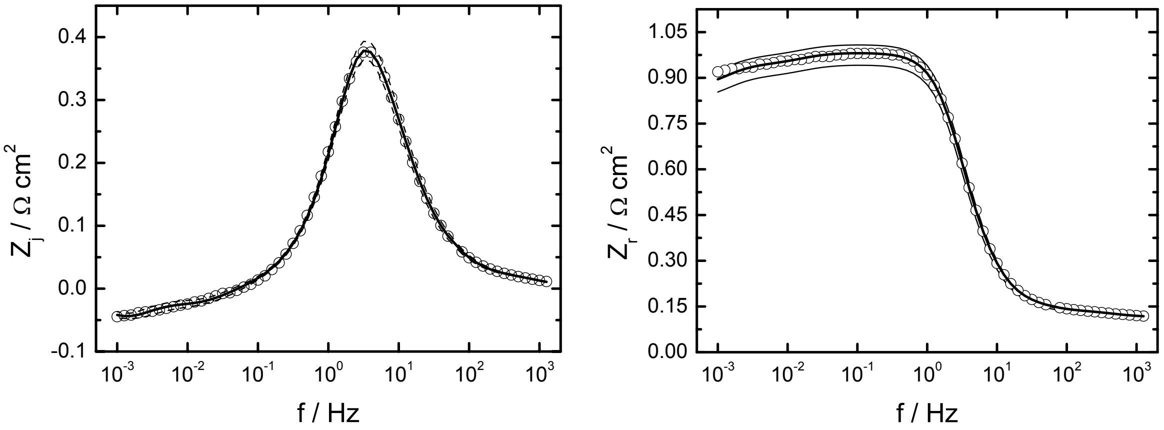

(a)

(b)

Figure 4-11: Regression of the Voigt model to the imaginary part of the impedance for the second scan of the impedance data collected at 0.2 A/cm^2 with the 850C: a) fit to the imaginary part of the measurement; and b) prediction of the real part. The ○ represents experimental data, the thick solid lines represent the measurement model fit, and the thin solid lines represent confidence intervals.

measurement model to the imaginary impedance data for the second scan of the series, for example, is shown in Figure 4-11(a). The predicted value for the real part of the impedance is compared to experimental values in Figure 4-11(b). The corresponding plots of normalized residual error are given in Figures 4-12(a) and 4-12(b). The data were found to be consistent with the Kramers-Kronig relations at all frequencies below 1000 Hz.

4.2.4 Impedance Response after Error Analysis

An example is presented in Figure 4-13 of the results of a complex regression of the measurement model to a data set in which data were removed that were found to be inconsistent with the Kramers-Kronig relations. The number of Voigt elements obtained by the regression was increased from 6 to 8 by deleting the inconsistent data. The weighting applied for the regression was based on the experimentally determined stochastic error structure. The data were collected using the Scribner 850C at 0.2 A/cm^2. The arrow in Figure 4-13 shows the impedance estimated from the slope of the polarization curve at the respective current density. The zero-frequency asymptote for the impedance can be expected to be equal to the slope of the polarization curve at that current density so long

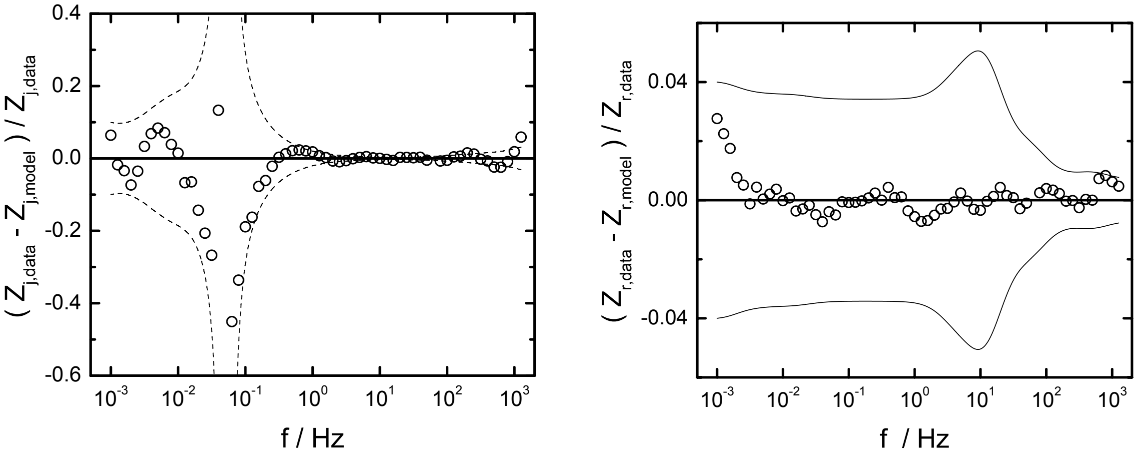

(a)

(b)

Figure 4-12: Residual errors for the regression presented in Figure 4-11: a) fit to the imaginary part, where dashed lines represent the ±2σ bound for the stochastic error; and b) prediction of the real part, where solid lines represent the 95.4% confidence intervals for the model obtained by Monte Carlo simulations.

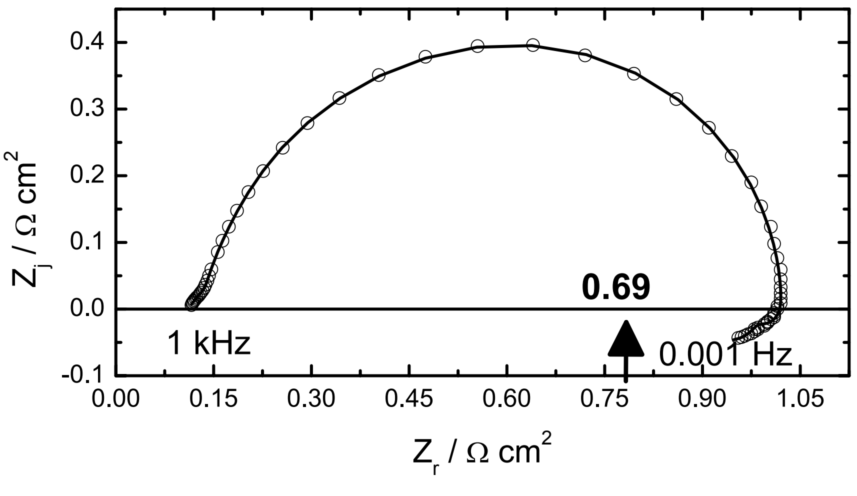

Figure 4-13: The results of complex regression of the measurement model to the second scan of the impedance data collected at 0.2 A/cm^2 with the Scribner 850C. The ∘ represents the experimental data and the solid line represents the measurement model fit.

as the polarization curve is measured in such a way as to represent a steady-state behavior. Kramers-Kronig-consistent low-frequency inductive loops were found at all current densities for both instruments.

4.3 Discussion

The determination of error structure presented in this work involved two steps. In the first, an estimate was obtained from replicated impedance scans for the standard deviation of stochastic errors in the measurement. This error structure was used to weight the regressions employed to check for consistency with the Kramers-Kronig relations. Determination of the standard deviation of stochastic errors in the measurement can be used to guide purchase of instrumentation or to guide selection of measurement parameters. For the parameters selected here, the two impedance systems provided comparable levels of noise.

The lack of consistency of high-frequency data with the Kramers-Kronig relations was observed for all measurements. The inconsistency at high frequencies is likely due to instrument and measurement system artifacts. As seen in Figure 4-7, the influence of the artifact extended well into the domain in which the imaginary impedance had a negative value. Removal of data with a positive imaginary impedance is not sufficient to eliminate the influence of high-frequency instrument artifacts in impedance measurements.

The lack of consistency of low-frequency data with the Kramers-Kronig relations, seen for the first impedance measurement in Figure 4-9(b), is likely associated with start-up transients. As described in Section 3.2.2, impedance measurements were conducted after repeated current-voltage cycling to hydrate the membrane. The first impedance scan was then measured after the specified current had been set for thirty minutes and the corresponding potential was stabilized. The impedance results indicate that the fuel cell had not reached steady-state operation due perhaps to changes to the humidification of the membrane and/or changes in consumption of reactants in the flow channels. The second scan of the impedance data, see Figure 4-10(b), showed improved consistency of low-frequency data with the Kramers-Kronig relations. These data were collected approximately after 3 hours of cell operation at the specified current.

The established start-up procedures,[192] including stabilization of potential at a set current, were not sufficient to ensure the steady-state condition. Impedance spectroscopy is seen to be much more sensitive to the condition of the fuel cell. This work demonstrates the utility of the measurement-model error analysis for identifying steady-state operation.

Not all low-frequency inductive loops were free of artifacts caused by nonstationary behavior, but, once a steady-state operation was established, the low-frequency inductive loops were found to be consistent with the Kramers-Kronig relations. The low-frequency inductive loops in the fuel cell can therefore be attributed to the response of physical processes occurring within the fuel cell.

CHAPTER 5
INTERPRETATION OF IMPEDANCE RESPONSE

Impedance models were developed to interpret the impedance response presented in Chapter 4. The models were formulated to account the fundamental processes of the fuel cell. The model response were compared with the experimental results. The details of ex-situ measurements used to support the proposed mechanism are presented in Chapter 6.

5.1 Introduction

In Chapter 4, the measurement model approach was used to demonstrate that, for the fuel cell under steady-state operation, the low-frequency inductive loops were consistent with the Kramers-Kronig relations. This work[194] demonstrated that, independent of the instrumentation used, the low-frequency features could be consistent with the Kramers-Kronig relations. Therefore, the low-frequency inductive loops could be attributed to process characteristics and not to non-stationary artifacts.

The objective of this work was to identify chemical and electrochemical reactions that could account for the low-frequency inductive impedance response and could therefore be incorporated into mechanistic models for the impedance response of the fuel cell. The model responses were compared to experimental results. Independent investigations were also conducted to support the possibility of the formation of the intermediates identified in the reaction mechanisms. The preliminary model development was reported in our previous work.[211]

5.2 Class of Model Development

Two classes of models, one with a cathodic reaction and intermediate involving hydrogen peroxide formation, and other related to catalyst deactivation evoked by platinum oxide formation, were considered in the work. More details about the reaction mechanisms can be found in Section 2.3. Side reactions and intermediates involved in the overall electrochemical reactions have been shown to result in low-frequency inductive loops.[212] Kinetic models accounting for reaction intermediates were addressed in greater detail in publication by Armstrong *et al.*[213] and Epelboin *et al.*[212] Impedance response for coupled reactions involving intermediate under potentiostatic control has been also illustrated elsewhere.[214]

5.3 Model Framework

The development of impedance models for specific hypothesized reaction sequences is presented in this section. The mass-transfer problem was simplified significantly by assuming that the membrane properties were uniform, that issues associated with flooding and gas-phase transport could be neglected, and that the heterogenous reactions took place at a plane, *e.g.,* the interface between the catalyst active layer and the the proton exchange membrane. This preliminary approach does not account for the spatial distribution of the catalyst particles in the catalyst layer, but this simplified treatment is sufficient to explore the role of specific reaction on impedance features, such as the low-frequency inductive loops.

5.3.1 Polarization Curve

The current density can be expressed as a function of electrode potential V, concentrations of reactants $c_i(0)$ at electrode surface, and surface coverage γ_k as

$$i = f(V, c_i(0), \gamma_k) \tag{5–1}$$

The reactants and products were assumed to diffuse through ionomer agglomerates in the catalyst layer. Concentrations of reactants and products at the reaction plane were calculated from the bulk concentrations $c_i(\infty)$ and the mass-transfer-limited current densities i_{lim} using

$$\bar{c}_i(0) = c_i(\infty)(1 - \frac{\bar{i}}{i_{\text{lim}}}) \tag{5–2}$$

where

$$i_{\text{lim}} = \frac{nFD_i c_i(\infty)}{\delta_i} \tag{5–3}$$

δ_i is the diffusion film thickness, F is Faraday's constant, D_i is the diffusivity of the reactant through ionomer agglomerates in the catalyst layer, and n is the number of electron exchanged in the reaction. The steady-state surface coverage was calculated by material balance of the intermediates involved in the proposed reaction mechanism.

The steady-state current for each reaction was calculated as function of overpotential using the values of the steady-state surface coverage and concentrations. The total steady-state current was calculated by adding current contributions from all participating reactions at the cathode, and the total current at the anode was equated to the total current from the cathode to calculate the anode overpotential η_a, *i.e.*,

$$\eta_a = \frac{1}{b_{\mathrm{H}_2}} \log \left(\frac{\bar{i}_{T,c}}{K_{\mathrm{H}_2} c_{\mathrm{H}_2}(\infty) \left(1 - \frac{\bar{i}_{T,c}}{i_{\mathrm{lim}}}\right)} \right) \tag{5–4}$$

where $\bar{i}_{T,c}$ is the total cathode current, K_{H_2} is the rate constant for the HOR defined as in equation (5–18), c_{H_2} is the concentration of the hydrogen, and b_{H_2} is the Tafel constant for the HOR. The cell potential U was given by

$$U = U_{eq.} - \eta_c - (-\eta_a) - IR_e \tag{5–5}$$

where η_c is the cathode overpotential and R_e is the frequency-independent ohmic resistance.

5.3.2 Impedance Response

The Faradaic current density can be expressed in terms of a steady state contribution $\bar{i}$ and an oscillating contribution $\widetilde{i}$ as

$$i_f = \bar{i}_f + \mathrm{Re}\left\{\widetilde{i}_f \exp\left(j\omega t\right)\right\} \tag{5–6}$$

where $j = \sqrt{-1}$, t is time, and ω is the frequency in units of s^{-1}. A Taylor series expansion of equation (5–1) about the steady-state value yields

$$\widetilde{i}_f = \left[\left. \frac{\partial f}{\partial V} \right|_{c_i(0),\gamma_k} \right] \widetilde{V} + \left[\left. \frac{\partial f}{\partial c_{i,0}} \right|_{V,c_{j\neq i}(0),\gamma_k} \right] \widetilde{c}_i(0) + \left[\left. \frac{\partial f}{\partial \gamma_k} \right|_{V,c_i(0),\gamma_{j\neq k}} \right] \widetilde{\gamma}_k \tag{5–7}$$

where $\widetilde{V}$,$\widetilde{c}_i(0)$ and $\widetilde{\gamma}_k$ were assumed to have small magnitudes such that the higher-order terms in the expansion can be neglected.

An expression for $\widetilde{c}_i(0)$ was found in terms of $\widetilde{i}_f$ using

$$\widetilde{i}_f = nFD_i \frac{\partial c_i}{\partial y} \tag{5–8}$$

or

$$\widetilde{c}_i(0) = \frac{\widetilde{i}_f \delta_i}{nFD_i} \left(-\frac{1}{\theta_i'(0)} \right) \tag{5–9}$$

where $\theta_i'(0)$ represents the dimensionless gradient of the oscillating concentration $\theta = \widetilde{c}_i / \widetilde{c}_i(0)$. Under the assumption that mass transfer is through a Nernst stagnant diffusion layer,

$$\frac{-1}{\theta_i'(0)} = \frac{\tanh \sqrt{jK_i}}{\sqrt{jK_i}} \tag{5–10}$$

where

$$K_i = \frac{\omega \delta_i^2}{D_i} \tag{5–11}$$

The Faradaic current was calculated by summing contributions from all the reactions in accordance with the reaction stoichiometry. The total current was found by summing the interfacial charging current and the Faradaic current, *i.e.*,

$$i = i_f + C_0 \frac{dV}{dt} \tag{5–12}$$

where C_0 is the interfacial capacitance. For a small-amplitude sinusoidal perturbation, the total current was written as

$$\widetilde{i} = \widetilde{i}_f + j\omega C_0 \widetilde{V} \tag{5–13}$$

An analytical expression for impedance was calculated for each model using

$$Z = \frac{\widetilde{U}}{\widetilde{i}} = R_e + \frac{\widetilde{V}}{\widetilde{i}} \tag{5–14}$$

where U is the cell potential, and V is the electrode potential.

5.4 Impedance Response for Proposed Reaction Mechanisms

The relationship between the fuel cell geometry and an equivalent circuit diagram for proposed reaction sequences is presented in Figure 5-1, where the boxes represent

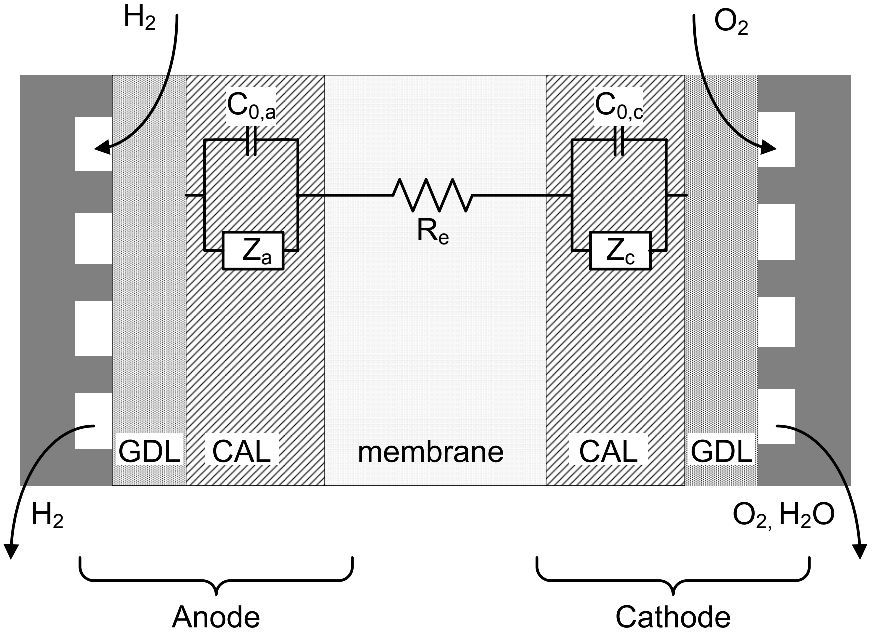

Figure 5-1: A schematic representation of the relationship between the fuel cell geometry and an equivalent circuit diagram for proposed reaction sequences where the boxes represent Faradaic impedances determined for specific reaction mechanisms.

Faradaic impedances that are to be determined for the specific assumed reaction mechanisms. Three impedance models were investigated for the interpretation of low-frequency inductive loops. Model 1 incorporates a single-step ORR at the cathode and a single-step HOR at the anode. Model 2 treats hydrogen peroxide formation in a two-step ORR at the cathode along with a single-step HOR at the anode, and Model 3 includes the single-step ORR coupled with the platinum catalyst dissolution at the cathode along with a single-step HOR at the anode. The literature suggests that the rate should be of the order of 3/2 with respect to proton concentration and of the order of 1 with respect to the oxygen concentration.[144] For the present work, the surface concentration of the proton was assumed to be constant and was therefore incorporated into the effective reaction rate constant.

5.4.1 Model 1: Simple Reaction Kinetics

The ORR

$$\mathrm{O_2} + 4\mathrm{H^+} + 4\mathrm{e^-} \rightarrow 2\mathrm{H_2O} \tag{5–15}$$

was assumed to take place at the cathode. The steady-state current density expression corresponding to this reaction was assumed to be

$$\bar{i}_{O_2} = -K_{O_2}\bar{c}_{O_2}(0)\exp\left(-b_{O_2}\eta_{O_2}\right) \tag{5–16}$$

where $K_{O_2} = nFk_{O_2}$, k_{O_2} is the rate constant, $n = 4$ is the number of electron exchanged in the reaction, $b_k = \alpha_k F/RT$, α_k is the apparent transfer coefficient for reaction k, R is the universal gas constant, T is absolute temperature, $\bar{c}_{\mathrm{i}}(0)$ is the concentration at electrode surface, $\eta_i = V - V_{eq.,i}$, η_i is the surface overpotential, and $V_{eq.,i}$ is the equilibrium potential.

The single-step HOR

$$\mathrm{H_2} \rightarrow 2\mathrm{H}^+ + 2\mathrm{e}^- \tag{5–17}$$

was assumed to take place at the anode. The corresponding steady-state current expression was

$$\bar{i}_{H_2} = K_{H_2}\bar{c}_{H_2}(0)\exp\left(b_{H_2}\eta_{H_2}\right) \tag{5–18}$$

where $K_{H_2} = nFk_{H_2}$, k_{H_2} is the rate constant, and $n = 2$.

The overall impedance was calculated as

$$Z = R_e + \frac{1}{\left(R_{t,H_2} + Z_{D,H_2}\right)^{-1} + j\omega C_0, a} + \frac{1}{\left(R_{t,O_2} + Z_{D,O_2}\right)^{-1} + j\omega C_0, c} \tag{5–19}$$

where R_e is the frequency independent ohmic resistance, $C_{0,c}$ is the interfacial capacitance at the cathode, $C_{0,a}$ is the interfacial capacitance at the anode, R_{t,O_2} is the charge-transfer resistance for the ORR, *i.e.,*

$$R_{t,O_2} = \left[K_{O_2}\bar{c}_{O_2}(0)b_{O_2}\exp(-b_{O_2}\bar{\eta}_{O_2})\right]^{-1} \tag{5–20}$$

Z_{D,O_2} is the mass-transport impedance for the ORR, *i.e.,*

$$Z_{D,O_2} = \frac{\delta_{O_2}}{\bar{c}_{O_2}(0)b_{O_2}4FD_{O_2}}\frac{-1}{\theta'_{O_2}(0)} \tag{5–21}$$

$R_{t,\mathrm{H_2}}$ is the charge-transfer resistance for the HOR, *i.e.*,

$$R_{t,\mathrm{H_2}} = \left[K_{\mathrm{H_2}}\overline{c}_{\mathrm{H_2}}(0)b_{\mathrm{H_2}}\exp(b_{\mathrm{H_2}}\overline{\eta}_{\mathrm{H_2}})\right]^{-1} \tag{5–22}$$

and $Z_{D,\mathrm{H_2}}$ is the mass-transport impedance for the HOR, *i.e.*,

$$Z_{D,\mathrm{H_2}} = \frac{\delta_{\mathrm{H_2}}}{\overline{c}_{\mathrm{H_2}}(0)b_{\mathrm{H_2}}2FD_{\mathrm{H_2}}}\frac{-1}{\theta'_{\mathrm{H_2}}(0)} \tag{5–23}$$

The term $-1/\theta'_i(0)$ was given by equation (5–10). Equations (5–20-5–23) represent lumped parameters that can be expressed in terms of parameters used to define the steady-state polarization curve.

The impedance response for Model 1 can be expressed as the equivalent circuit shown in Figure 5-2(a) for the anode where $R_{t,\mathrm{H_2}}$ is given by equation (5–22) and $Z_{D,\mathrm{H_2}}$ is given by equation (5–23) and in Figure 5-2(b) for the cathode, where $R_{t,\mathrm{O_2}}$ is given by equation (5–20) and $Z_{D,\mathrm{O_2}}$ is given by equation (5–21).

5.4.2 Model 2: Hydrogen Peroxide Formation

The ORR was assumed to take place in two steps in accordance to the reaction scheme as discussed in the literature.[8] The first reaction

$$\mathrm{O_2} + 2\mathrm{H^+} + 2\mathrm{e^-} \rightarrow \mathrm{H_2O_2} \tag{5–24}$$

involves formation of hydrogen peroxide (H_2O_2) which reacts further to form water, *i.e.*,

$$\mathrm{H_2O_2} + 2\mathrm{H^+} + 2\mathrm{e^-} \rightarrow 2\mathrm{H_2O} \tag{5–25}$$

Crossover of hydrogen to the cathode is reported to facilitate the reaction of oxygen and hydrogen at the cathode, generating hydroxyl and hydroperoxyl radicals which react further to produce hydrogen peroxide at the cathode.[100] The hypothesis that H_2O_2 may be formed at the cathode of fuel cell is supported by the results of Inaba *et al.*[77] They reported that formation of peroxide by a two-electron path was favored over formation of water by a four-electron path in ORR on nanoparticles of Pt supported on carbon at

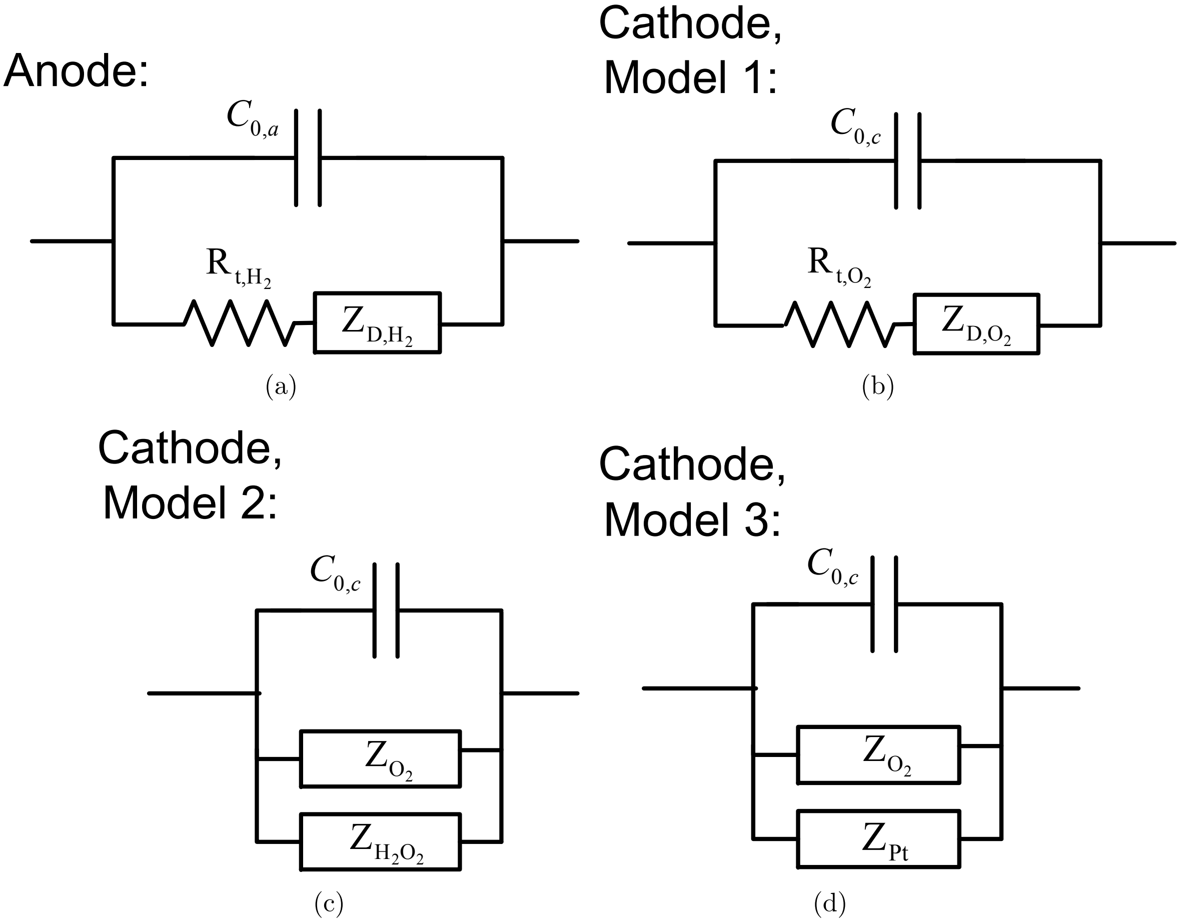

Figure 5-2: Equivalent circuit diagrams for proposed reaction sequences where the boxes represent diffusion impedances or Faradaic impedances determined for specific reaction mechanisms: a) anode for all models; b) cathode for Model 1; c) cathode for Model 2; and d) cathode for Model 3.

cathodic potential. While their work supports formation of peroxide at the cathode of the fuel cell, peroxide formation at the anode is also possible due to O_2 crossover. A more inclusive impedance model could be developed by accounting for peroxide formation at the anode.

The steady-state current for reaction (5–24) can be expressed as

$$\bar{i}_{\mathrm{O}_2} = -K_{\mathrm{O}_2}\bar{c}_{\mathrm{O}_2}(0)\left(1-\gamma_{\mathrm{H}_2\mathrm{O}_2}\right)\exp\left(-b_{\mathrm{O}_2}\eta_{\mathrm{O}_2}\right) \tag{5–26}$$

where $K_{\mathrm{O}_2} = nFk_{\mathrm{O}_2}$ with the same notation defined for Model 1, $n = 2$, and $\gamma_{\mathrm{H}_2\mathrm{O}_2}$ is the fractional surface coverage of hydrogen peroxide. The current density corresponding to the reaction (5–25) can be expressed as

$$\bar{i}_{\mathrm{H}_2\mathrm{O}_2} = -K_{\mathrm{H}_2\mathrm{O}_2}\gamma_{\mathrm{H}_2\mathrm{O}_2}\exp\left(-b_{\mathrm{H}_2\mathrm{O}_2}\eta_{\mathrm{H}_2\mathrm{O}_2}\right) \tag{5–27}$$

where $K_{\mathrm{H}_2\mathrm{O}_2} = nF\Gamma k_{\mathrm{H}_2\mathrm{O}_2}$, $n = 2$, and Γ is the maximum surface coverage. The electrochemical reaction at the anode was given as reaction (5–17), and the corresponding current expression was given as equation (5–18). Diffusion of peroxide away from the catalyst surface was ignored in the present work. Thus, the peroxide produced by reaction (5–24) was subsequently consumed in reaction (5–25) to form water.

The overall impedance was calculated as

$$Z = R_e + \frac{1}{\frac{1}{R_{t,\mathrm{H}_2}+Z_{D,\mathrm{H}_2}} + j\omega C_0,a} + \frac{1}{\mathrm{Z}_{\mathrm{eff}} + \frac{A}{j2\Gamma F\omega - B} + j\omega C_0,c} \tag{5–28}$$

where

$$\mathrm{Z}_{\mathrm{eff}} = \frac{1}{R_{t,\mathrm{O}_2} + Z_{D,\mathrm{O}_2}} + \frac{1}{R_{t,\mathrm{H}_2\mathrm{O}_2}} \tag{5–29}$$

$$A = \left[\frac{1}{(R_{t,\mathrm{O}_2}+Z_{D,\mathrm{O}_2})(1-\bar{\gamma}_{\mathrm{H}_2\mathrm{O}_2})} - \frac{1}{R_{t,\mathrm{H}_2\mathrm{O}_2}\bar{\gamma}_{\mathrm{H}_2\mathrm{O}_2}}\right]\left[\frac{1}{R_{t,\mathrm{O}_2}+Z_{D,\mathrm{O}_2}} - \frac{1}{R_{t,\mathrm{H}_2\mathrm{O}_2}}\right] \tag{5–30}$$

and

$$B = \left[\frac{1}{(R_{t,\mathrm{O}_2}+Z_{D,\mathrm{O}_2})(1-\bar{\gamma}_{\mathrm{H}_2\mathrm{O}_2})} - \frac{1}{R_{t,\mathrm{H}_2\mathrm{O}_2}\bar{\gamma}_{\mathrm{H}_2\mathrm{O}_2}}\right] \tag{5–31}$$

In equation (5–29), R_{t,O_2} is the charge-transfer resistance for the first step of the ORR, *i.e.*,

$$R_{t,\mathrm{O}_2} = \left[K_{\mathrm{O}_2}\bar{c}_{\mathrm{O}_2}(0)b_{\mathrm{O}_2}(1-\overline{\gamma}_{\mathrm{H}_2\mathrm{O}_2})\exp(-b_{\mathrm{O}_2}\overline{\eta}_{\mathrm{O}_2})\right]^{-1} \tag{5–32}$$

Z_{D,O_2} is the mass-transfer impedance for the first step of the ORR, *i.e.*,

$$Z_{D,\mathrm{O}_2} = \frac{\delta_{\mathrm{O}_2}}{\bar{c}_{\mathrm{O}_2}(0)b_{\mathrm{O}_2}2FD_{\mathrm{O}_2}}\frac{-1}{\theta'_{\mathrm{O}_2}(0)} \tag{5–33}$$

and $R_{t,\mathrm{H}_2\mathrm{O}_2}$ is the charge-transfer resistance for the second step of the ORR, *i.e.*,

$$R_{t,\mathrm{H}_2\mathrm{O}_2} = \left[K_{\mathrm{H}_2\mathrm{O}_2}b_{\mathrm{H}_2\mathrm{O}_2}\gamma_{\mathrm{H}_2\mathrm{O}_2}\exp(-b_{\mathrm{H}_2\mathrm{O}_2}\overline{\eta}_{\mathrm{H}_2\mathrm{O}_2})\right]^{-1} \tag{5–34}$$

The steady-state surface coverage of the peroxide is given as:

$$\overline{\gamma}_{H_2O_2} = \frac{K_{\mathrm{O}_2}\bar{c}_{\mathrm{O}_2}(0)b_{\mathrm{O}_2}\exp(-b_{\mathrm{O}_2}\overline{\eta}_{\mathrm{O}_2})}{K_{\mathrm{O}_2}\bar{c}_{\mathrm{O}_2}(0)b_{\mathrm{O}_2}\exp(-b_{\mathrm{O}_2}\overline{\eta}_{\mathrm{O}_2}) + K_{\mathrm{H}_2\mathrm{O}_2}b_{\mathrm{H}_2\mathrm{O}_2}\exp(-b_{\mathrm{H}_2\mathrm{O}_2}\overline{\eta}_{\mathrm{H}_2\mathrm{O}_2})} \tag{5–35}$$

Expressions for R_{t,H_2} and Z_{D,H_2} were given by equations (5–22) and (5–23), respectively, as defined in Model 1.

The impedance response for Model 2 can be expressed as the equivalent circuit shown in Figure 5-2(a) for the anode and Figure 5-2(c) for the cathode. The boxes in Figures 5-2(a) represent a diffusion impedance corresponding to transport of hydrogen, and the boxes in Figure 5-2(c) represent the Faradaic impedances corresponding to the proposed reaction sequence. The term Z_c in Figure 5-1 is given by

$$Z_c = \left(\frac{1}{Z_{\mathrm{O}_2}} + \frac{1}{Z_{\mathrm{H}_2\mathrm{O}_2}}\right)^{-1} \tag{5–36}$$

It should be emphasized that Z_{O_2} is not the sum of R_{t,O_2} and Z_{D,O_2} due to the surface coverage. Similarly, $Z_{\mathrm{H}_2\mathrm{O}_2}$ cannot be considered to be a frequency-independent $R_{t,\mathrm{H}_2\mathrm{O}_2}$.

5.4.3 Model 3: Platinum Dissolution

The platinum dissolution was assumed to occur by a reaction scheme similar to that reported by Darling *et al.*,[10] *i.e.*, by an electrochemical reaction

$$\mathrm{Pt} + \mathrm{H_2O} \rightleftarrows \mathrm{PtO} + 2\mathrm{H}^+ + 2\mathrm{e}^- \tag{5–37}$$

in which PtO is formed, followed by a chemical dissolution reaction

$$\mathrm{PtO} + 2\mathrm{H}^+ \rightarrow \mathrm{Pt}^{+2} + \mathrm{H_2O} \tag{5–38}$$

The model developed by Darling and Meyers resulted in an equilibrium oxide coverage by PtO.[10] A similar reaction scheme for Pt dissolution with PtO as an intermediate at the cathodic potential of the fuel cell has also been reported by Dam *et al.*[91] Also, Xu *et al.*[215] have reported two schemes for Pt oxidation at the cathode, both having PtO as an intermediate.

The current density corresponding to reaction (5–37) was given by

$$\bar{i}_{\mathrm{Pt}} = K_{\mathrm{Pt},f}(1-\gamma_{\mathrm{PtO}})\exp\left(b_{\mathrm{Pt},f}\eta_{\mathrm{Pt},f}\right) - K_{\mathrm{Pt},b}\gamma_{\mathrm{PtO}}\exp\left(-b_{\mathrm{Pt},b}\eta_{\mathrm{Pt},b}\right) \tag{5–39}$$

where $K_{\mathrm{Pt},f} = nF\Gamma k_{\mathrm{Pt},f}$, $K_{\mathrm{Pt},b} = nFk_{\mathrm{Pt},b}$, $n = 2$, Γ is the maximum surface coverage, and γ_{PtO} is the fractional surface coverage by PtO. The dissolution of PtO was assumed to occur according to

$$r_{\mathrm{PtO}} = K_3\gamma_{\mathrm{PtO}} \tag{5–40}$$

and the corresponding material balance for the PtO was expressed as

$$\Gamma\frac{\partial\gamma_{\mathrm{PtO}}}{\partial t} = \frac{i_{\mathrm{Pt}}}{2F} - r_{\mathrm{PtO}} \tag{5–41}$$

The formation of the platinum oxide was proposed to have an indirect influence on the ORR at the cathode by changing the effective rate constant for the reaction. Thus,

$$K_{\mathrm{eff}} = K_{\mathrm{Pt}} + (K_{\mathrm{PtO}} - K_{\mathrm{Pt}})\gamma_{\mathrm{PtO}} \tag{5–42}$$

where K_{Pt} is the rate constant on a platinum site and K_{PtO} is the rate constant on a platinum oxide site. The ORR was assumed to take place according to reaction (5–15) with a steady-state current density given by

$$\bar{i}_{\mathrm{O}_2} = -K_{\mathrm{eff}}\bar{c}_{\mathrm{O}_2}(0)\exp\left(-b_{\mathrm{O}_2}\eta_{\mathrm{O}_2}\right) \tag{5–43}$$

where K_{eff} is defined by equation (5–42).

The overall impedance was calculated to be

$$Z = R_e + \frac{1}{\frac{1}{R_{t,\mathrm{H}_2}+Z_{D,\mathrm{H}_2}} + j\omega C_0, a} + \frac{1}{Z_{\mathrm{eff}} + \frac{A}{2F(j\Gamma\omega+K_3)+B} + j\omega C_0, c} \tag{5–44}$$

where

$$Z_{\mathrm{eff}} = \frac{1}{R_{t,\mathrm{O}_2} + Z_{D,\mathrm{O}_2}} + \frac{1}{R_{\mathrm{Pt},f}} + \frac{1}{R_{\mathrm{Pt},b}} \tag{5–45}$$

$$A = \left[\frac{(K_{\mathrm{PtO}} - K_{\mathrm{Pt}})}{K_{\mathrm{eff}} b_{\mathrm{O}_2}} - \frac{1}{R_{\mathrm{Pt},f} b_{\mathrm{Pt},f}(1-\bar{\gamma}_{\mathrm{PtO}})} - \frac{1}{R_{\mathrm{Pt},b} b_{\mathrm{Pt},b}\bar{\gamma}_{\mathrm{PtO}}}\right]\left(\frac{1}{R_{\mathrm{Pt},f}} + \frac{1}{R_{\mathrm{Pt},b}}\right) \tag{5–46}$$

and

$$B = \frac{1}{R_{\mathrm{Pt},f} b_{\mathrm{Pt},f}(1-\bar{\gamma}_{\mathrm{PtO}})} + \frac{1}{R_{\mathrm{Pt},b} b_{\mathrm{Pt},b}\bar{\gamma}_{\mathrm{PtO}}} \tag{5–47}$$

In equation (5–45), R_{t,O_2} is the charge-transfer resistance for the ORR, *i.e.*,

$$R_{t,\mathrm{O}_2} = \left[K_{\mathrm{eff}}\bar{c}_{\mathrm{O}_2}(0) b_{\mathrm{O}_2}\exp(-b_{\mathrm{O}_2}\bar{\eta}_{\mathrm{O}_2})\right]^{-1} \tag{5–48}$$

Z_{D,O_2} is the mass-transport impedance for the ORR, *i.e.*,

$$Z_{D,\mathrm{O}_2} = \frac{\delta_{\mathrm{O}_2}}{\bar{c}_{\mathrm{O}_2}(0) b_{\mathrm{O}_2} 4F D_{\mathrm{O}_2}} \frac{-1}{\theta'_{\mathrm{O}_2}(0)} \tag{5–49}$$

$R_{\mathrm{Pt},f}$ is the charge-transfer resistance for the forward reaction, *i.e.*,

$$R_{\mathrm{Pt},f} = \left[K_{\mathrm{Pt},f} b_{\mathrm{Pt},f}(1-\bar{\gamma}_{\mathrm{PtO}})\exp(b_{\mathrm{Pt},f}\bar{\eta}_{\mathrm{Pt},f})\right]^{-1} \tag{5–50}$$

and $R_{\mathrm{Pt},b}$ is the charge-transfer resistance for the backward reaction, *i.e.*,

$$R_{\mathrm{Pt},b} = \left[K_{\mathrm{Pt},b} b_{\mathrm{Pt},b}\bar{\gamma}_{\mathrm{PtO}}\exp(-b_{\mathrm{Pt},b}\bar{\eta}_{\mathrm{Pt},b})\right]^{-1} \tag{5–51}$$

The steady-state surface coverage of the platinum oxide is given as

$$\overline{\gamma}_{\mathrm{PtO}} = \frac{K_{\mathrm{Pt},f} b_{\mathrm{Pt},f} \exp(b_{\mathrm{Pt},f} \overline{\eta}_{\mathrm{Pt},f})}{K_{\mathrm{Pt},b} b_{\mathrm{Pt},f} \exp(b_{\mathrm{Pt},f} \overline{\eta}_{\mathrm{Pt},f}) + K_{\mathrm{Pt},b} b_{\mathrm{Pt},b} \exp(-b_{\mathrm{Pt},b} \overline{\eta}_{\mathrm{Pt},b}) + 2FK_3} \tag{5–52}$$

Model 3 was derived for a general expression of K_{eff} as described in equation (5–42) but for $K_{\mathrm{PtO}} << K_{\mathrm{Pt}}$, the expression for K_{eff} reduces to

$$K_{\mathrm{eff}} = K_{\mathrm{Pt}}(1 - \gamma_{\mathrm{PtO}}) \tag{5–53}$$

which simplifies equation(5–46) to

$$A = \left[-\frac{1}{(1-\overline{\gamma}_{\mathrm{PtO}}) b_{\mathrm{O}_2}} - \frac{1}{R_{\mathrm{Pt},f} b_{\mathrm{Pt},f} (1-\overline{\gamma}_{\mathrm{PtO}})} - \frac{1}{R_{\mathrm{Pt},b} b_{\mathrm{Pt},b} \overline{\gamma}_{\mathrm{PtO}}} \right] \left(\frac{1}{R_{\mathrm{Pt},f}} + \frac{1}{R_{\mathrm{Pt},b}} \right) \tag{5–54}$$

and equation (5–45) to

$$R_{t,\mathrm{O}_2} = \left[K_{\mathrm{Pt}} (1 - \overline{\gamma}_{\mathrm{PtO}}) \overline{c}_{\mathrm{O}_2}(0) b_{\mathrm{O}_2} \exp(-b_{\mathrm{O}_2} \overline{\eta}_{\mathrm{O}_2}) \right]^{-1} \tag{5–55}$$

Expressions for R_{t,H_2} and Z_{D,H_2} were given by equations (5–22) and (5–23), respectively, as defined in Model 1.

The impedance response for Model 3 can be expressed as the equivalent circuit shown in Figure 5-2(a) for the anode and Figure 5-2(d) for the cathode. The term Z_c in Figure 5-1 is given by

$$Z_c = \left(\frac{1}{Z_{\mathrm{O}_2}} + \frac{1}{Z_{\mathrm{Pt}}} \right)^{-1} \tag{5–56}$$

As was discussed for Model 2, the surface coverage of PtO influences the impedance contributions of Z_{O_2} and Z_{Pt}.

5.5 Results

The experimental results of the steady-state and impedance measurements are discussed in this section and compared to the impedance response generated by the three mechanistic models discussed in previous sections.

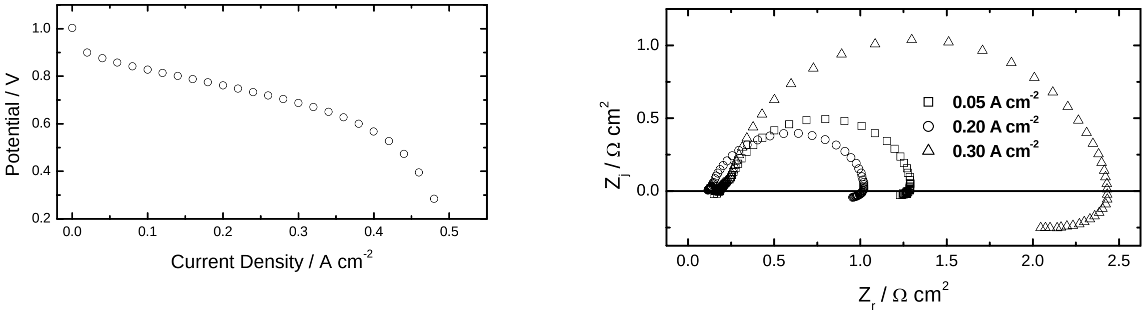

(a) (b)

Figure 5-3: Electrochemical results obtained with H_2 as reactant at the anode and air as oxidant at the cathode. The anode and cell temperatures were 40 °C, and the cathode temperature was 35 °C. a) Polarization curve; and b) impedance response with current density as a parameter.

5.5.1 Experimental Polarization and Impedance Results

The polarization curve for the fuel cell is presented in Figure 5-3(a). The cell response is strongly influenced by reaction kinetics at low current densities. The influence of the Ohmic potential drop is evident at intermediate current densities, and the mass-transfer limitations are evident at large current densities.

To explore the behavior of the fuel cell, the impedance was measured at several points on the polarization curve. Typical impedance spectra are presented in Figure 5-3(b) for current densities chosen to be representative of the kinetic, ohmic, and mass-transfer controlled regions of the polarization curve. The impedance spectra have a general form consisting of one high-frequency capacitive loop and one incomplete low-frequency inductive loop. Similar inductive loops were reported by Makharia *et al.*[208] for small current densities in which kinetic limitations dominate. The present work demonstrates that similar low-frequency inductive loops can be observed for all regions of the polarization curve.

5.5.2 Model Response Analysis

Equations (5–19), (5–28), and **(5–44)** provide mathematical expressions for the impedance response of a fuel cell associated with the reaction mechanisms described in

Table 5-1: Parameters used to calculate the impedance response corresponding to Models 1, 2, and 3.

Parameters	Model 1	Model 2	Model 3
$D_{\mathrm{O}_2}, \mathrm{m}^2/\mathrm{s}$	4×10^{-11}	4×10^{-11}	4×10^{-11}
$D_{\mathrm{H}_2}, \mathrm{m}^2/\mathrm{s}$	4×10^{-9}	4×10^{-9}	4×10^{-9}
$D_{\mathrm{H}_2\mathrm{O}_2}, \mathrm{m}^2/\mathrm{s}$	-	4×10^{-15}	-
δ, m	1×10^{-6}	1×10^{-6}	1×10^{-6}
$R_{\mathrm{e}}, \Omega\mathrm{cm}^2$	0.135	0.135	0.135
C_0, F	0.212	0.212	0.212
b_{H_2}, V^{-1}	65	40	40
b_{O2}, V^{-1}	27	27	45
$b_{\mathrm{H}_2\mathrm{O}_2}, V^{-1}$	-	15	-
b_{Pt}, V^{-1}	-	-	14
$K_{\mathrm{H}_2}, \mathrm{Acm/mol}$	0.55	1.34	1.35
$K_{\mathrm{O}_2}, \mathrm{Acm/mol}$	961.9	10900	10900
$K_{\mathrm{H}_2\mathrm{O}_2}, \mathrm{A/mol}$	-	1900	-
$K_{\mathrm{Pt}}, \mathrm{Acm/mol}$	-	-	6.2
$K_{\mathrm{PtO}}, \mathrm{Acm/mol}$	-	-	0.01
$K_3, \mathrm{mol/s}$	-	-	0.01
$K_{\mathrm{Pt,f}}, \mathrm{A/mol}$	-	-	0.01
$K_{\mathrm{Pt,b}}, \mathrm{A/cm}^2$	-	-	0.01

the previous sections. These models were compared to the experimental polarization and impedance data. The method employed was to calculate the polarization curve that matched closely the experimental results and then to use the same parameters to estimate the impedance response at different currents. Direct regression was not employed as the model does not account explicitly for the non-uniform reaction rates along the length of the serpentine flow channels.

Model parameters are presented in Table 5-1. Constant values were assumed for the interfacial capacitance, ionic resistance in the catalyst layer, membrane resistance, and oxygen permeability through ionomer agglomerates in the catalyst layer. When appropriate, numerical values were taken from the literature.[64] The impedance response for all simulations corresponded to a frequency range of 10 kHz to 0.001 mHz. Calculations at low frequency were used to explore more fully the low-frequency inductive features.

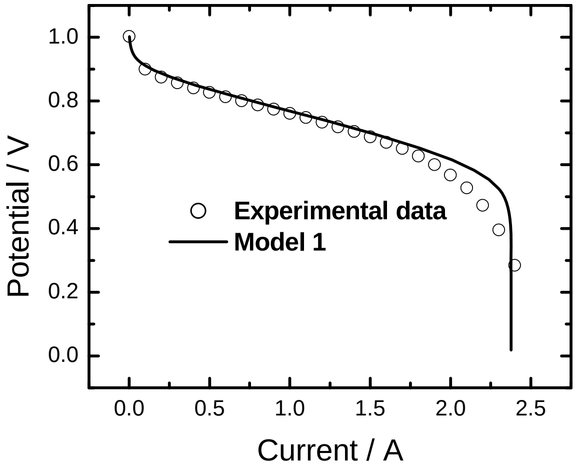

Figure 5-4: Polarization curve generated by Model 1 for 40 °C using parameters reported in Table 5-1 and compared with the experimental data presented in Figure 5-3(a).

5.5.2.1 Model 1

The polarization curve generated from Model 1 is compared to experimental data in Figure 5-4. The parameters used to generate the polarization curve were then used to calculate the impedance response. The results for an intermediate-current (0.2 A/cm^2) are compared in Figure 5-5 to the experimental data. The impedance response for Model 1 consisted of one compressed capacitive loop with a straight-line portion at high frequency. Similar impedance spectra have been reported in the literature.[107,65,216] The capacitive arc can be attributed to the single-step ORR at the cathode. The straight-line portion at the higher frequencies can be attributed to mass transport impedance associated with diffusion of oxygen. Model 1 provides a reasonable representation of the capacitive loops, but cannot account for the inductive loops seen at low frequency.

The inability of Model 1 to account for the low-frequency inductive loops is seen more clearly in Figures 5-6(a) and 5-6(b), where the real and imaginary parts of the impedance are presented, respectively, as functions of frequency. Model 1 provided similar agreement to the experimental results at both lower and higher current densities. Thus, the model

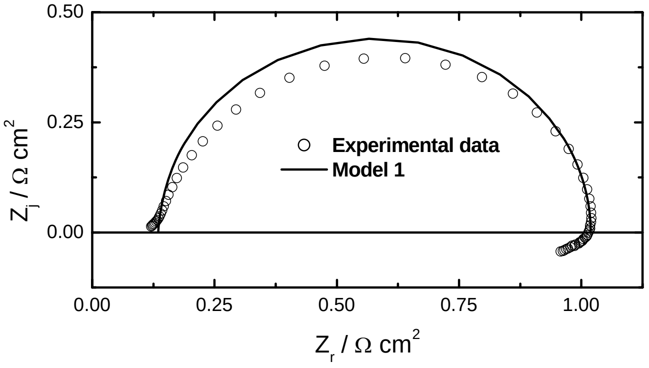

Figure 5-5: Impedance response for 0.2 A/cm^2 generated by Model 1 for 40 °C using parameters reported in Table 5-1 and compared with the experimental data presented in Figure 5-3(b).

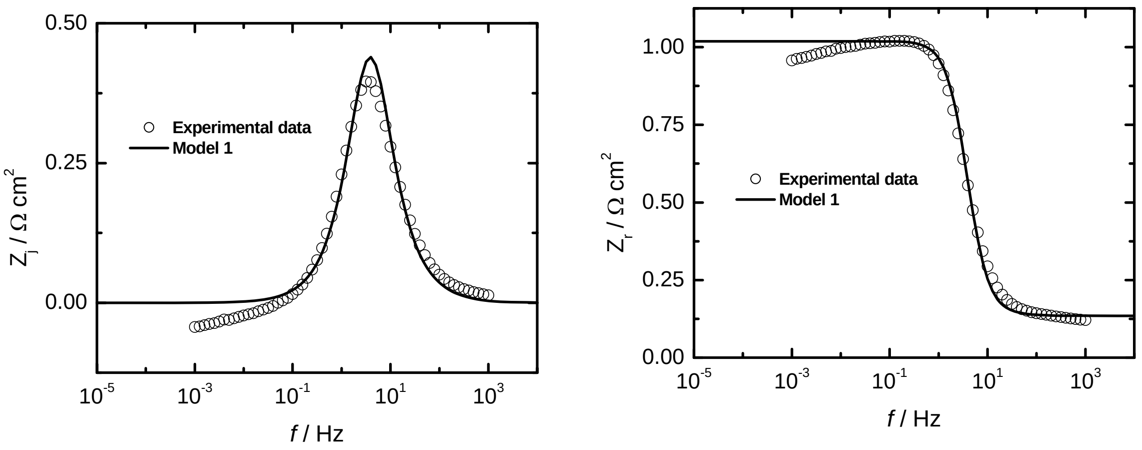

(a) (b)

Figure 5-6: Impedance response for 0.2 A/cm^2 generated by Model 1 for 40 °C using parameters reported in Table 5-1; a) real part of the impedance of the model response compared with the experimental data presented in the Figure 5-3(b); and b) imaginary part of the impedance of the model response compared with the experimental data presented in Figure 5-3(b).

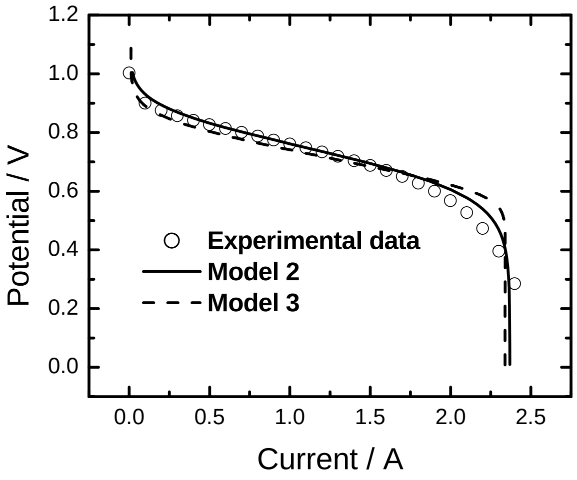

Figure 5-7: Polarization curve generated by Models 2 and 3 for 40 °C using parameters reported in Table 5-1 and compared with the experimental data presented in Figure 5-3(a).

that accounts for only the hydrogen oxidation and oxygen reduction reactions cannot explain the inductive behavior at low frequencies.

5.5.2.2 Models 2 and 3

The polarization curves generated with Models 2 and 3 are presented in Figure 5-7. The presence of the side reactions in the model has little discernable influence on the polarization curve because these reactions are assumed to be taking place at a low rate as compared to the dominant hydrogen oxidation and oxygen reduction reactions. The relative contributions of the different reactions at the cathode are shown in Figure 5-8. As shown in Figure 5-8(a), the two reduction steps in Model 2 contributed equally to the total current because the desorption/loss of peroxide was not considered in the model development. The contribution to total current by platinum dissolution shown in Figure 5-8(b) was found to be negligible as compared to oxygen reduction.

The impedance response for the model with the hydrogen peroxide formation (Model 2) consisted of one high-frequency capacitive loop and one low-frequency inductive loop. The impedance response for the model accounting for platinum dissolution (Model 3) also consisted of one high-frequency capacitive loop and one low-frequency inductive

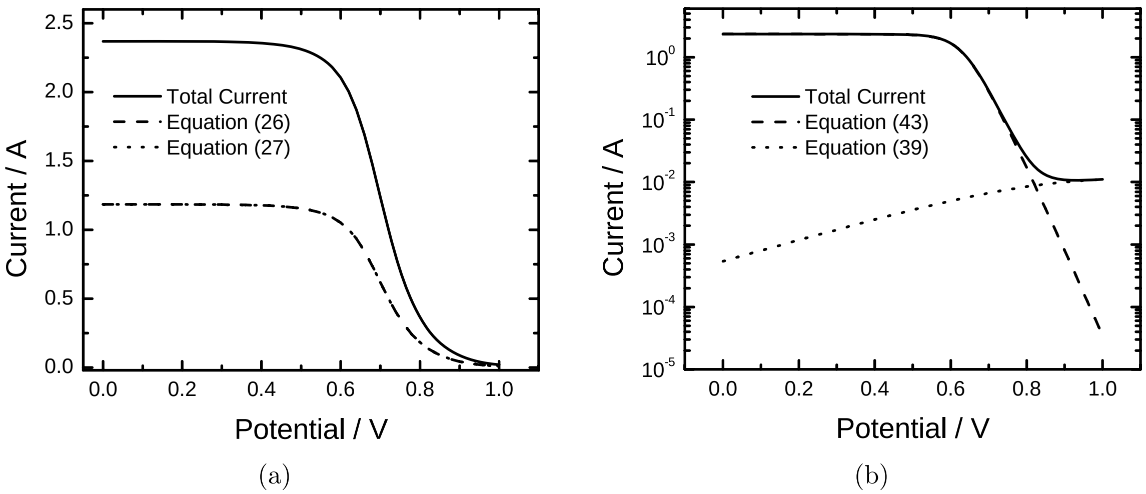

Figure 5-8: Relative contributions of two reactions to total current at the cathode: a) Model 2; and b) Model 3.

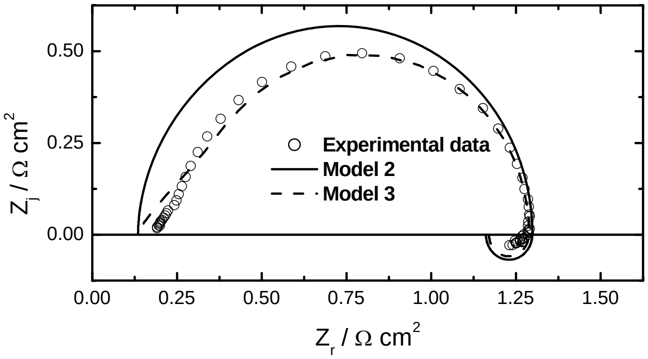

Figure 5-9: Impedance response for 0.05 A/cm^2 generated by Models 2 and 3 for 40 °C using parameters reported in Table 5-1 and compared with the experimental data presented in Figure 5-3(b).

loop. A comparison between the model and experiment is presented in Nyquist-format in Figure 5-9 for current densities in the kinetically controlled part of the polarization curve. The real and imaginary parts of the impedance are presented as functions of frequency in Figures 5-10(a) and 5-10(b), respectively. Similar results are shown in Figures 5-11, 5-12(a), and 5-12(b) for the intermediate current density and in Figures 5-13, 5-14(a), and 5-14(b) for high current densities. Impedance measurements are much more sensitive than polarization curves to the presence of minor reactions. Both Models 2

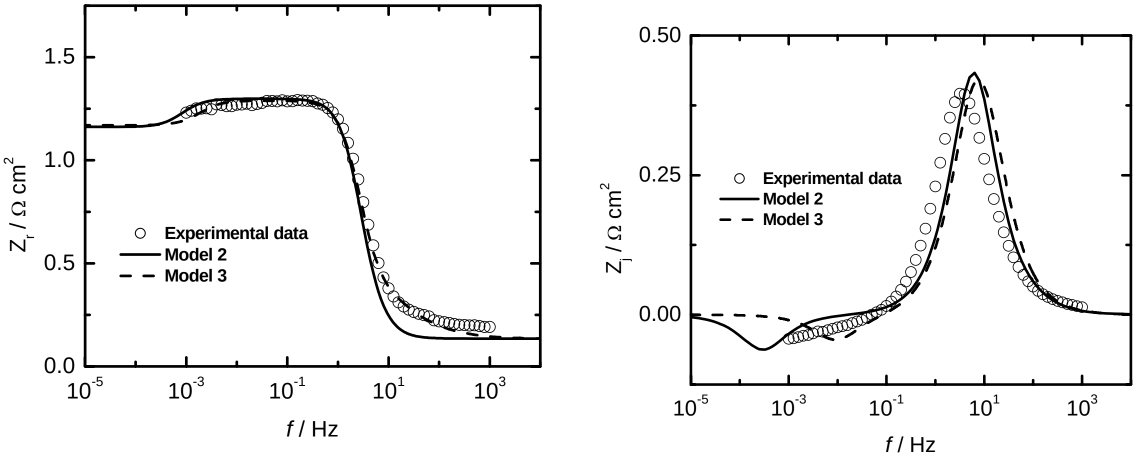

(a) (b)

Figure 5-10: Impedance response for 0.05 A/cm^2 generated by Models 2 and 3 for 40 °C using parameters reported in Table 5-1: a) real part of the impedance of the model response compared with the experimental data presented in Figure 5-3(b); and b) imaginary part of the impedance of the model response compared with the experimental data presented in Figure 5-3(b).

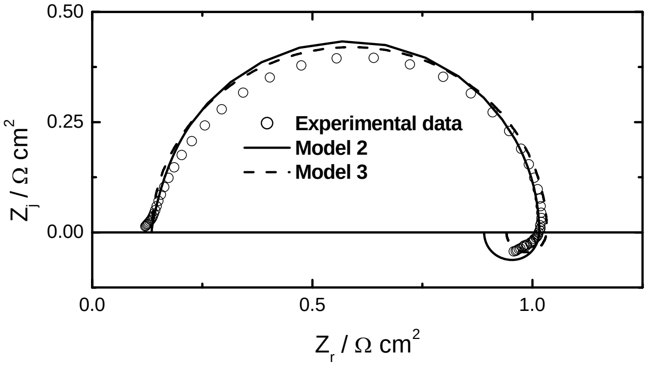

Figure 5-11: Impedance response for 0.2 A/cm^2 generated by Models 2 and 3 for 40 °C using parameters reported in Table 5-1 and compared with the experimental data presented in Figure 5-3(b).

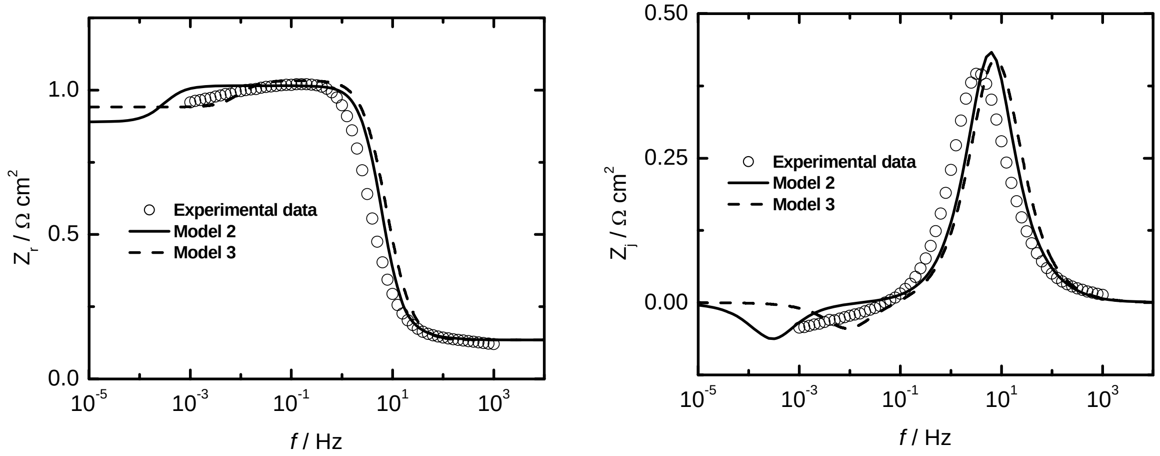

(a)

(b)

Figure 5-12: Impedance response for 0.2 A/cm^2 generated by Models 2 and 3 for 40 °C using parameters reported in Table 5-1: a) real part of the impedance of the model response compared with the experimental data presented in Figure 5-3(b); and b) imaginary part of the impedance of the model response compared with the experimental data presented in Figure 5-3(b).

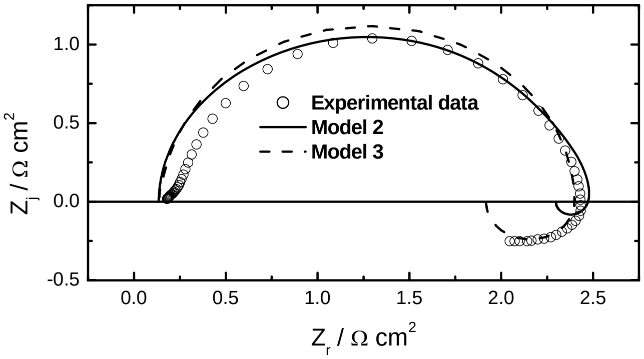

Figure 5-13: Impedance response for 0.3 A/cm^2 generated by Models 2 and 3 for 40 °C using parameters reported in Table 5-1 and compared with the experimental data presented in Figure 5-3(b).

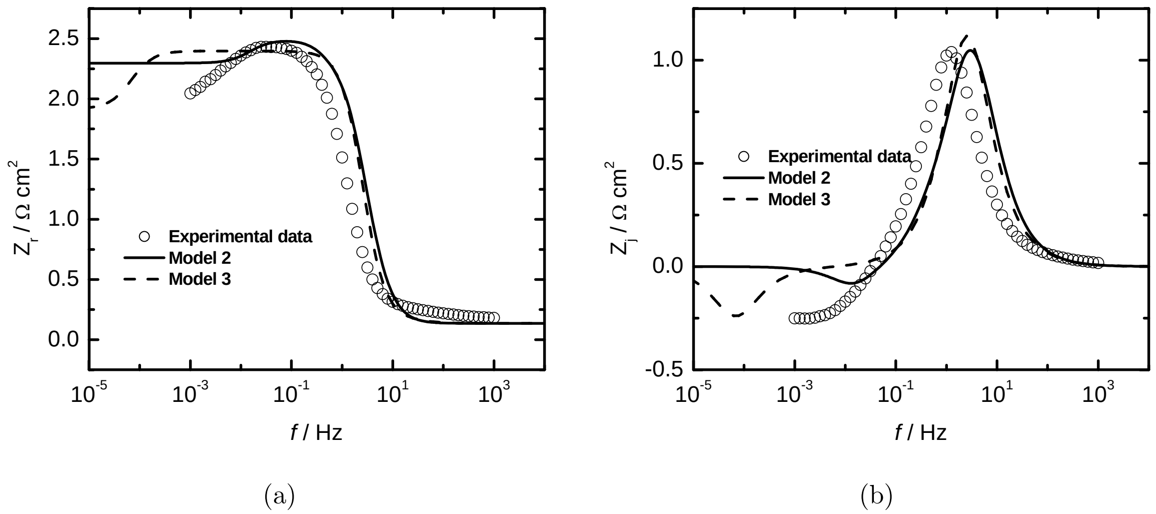

Figure 5-14: Impedance response for 0.3 A/cm^2 generated by Models 2 and 3 for 40 °C using parameters reported in Table 5-1: a) real part of the impedance of the model response compared with the experimental data presented in Figure 5-3(b); and b) imaginary part of the impedance of the model response compared with the experimental data presented in Figure 5-3(b).

and 3 were found to be capable of yielding low-frequency inductive loops at all portions of the polarization curve.

5.6 Discussion

The inductive loops seen in low-frequency impedance measurements for the fuel cell have gained recent attention in the literature. Several explanations have been proposed. Models for impedance response are not unique, and many models can lead to specific features such as the low-frequency inductive loops described in the present work. The influence of carbon monoxide poisoning on the anode kinetics has been invoked by several authors.[106, 119, 187, 122] The cathode kinetics were limiting in the configuration employed in the present experiments, which used a symmetric platinum loading. In addition, the anode and cathode gases used were rated ultra-pure, so the influence of carbon monoxide could be excluded for the present experiments. Wiezell *et al.*[145, 217] have proposed that non-uniform water transport in the anode could lead to low-frequency inductive loops due to the influence of water on the anode kinetics. Such an explanation does not apply for the present experiments as they were dominated by cathode kinetics.

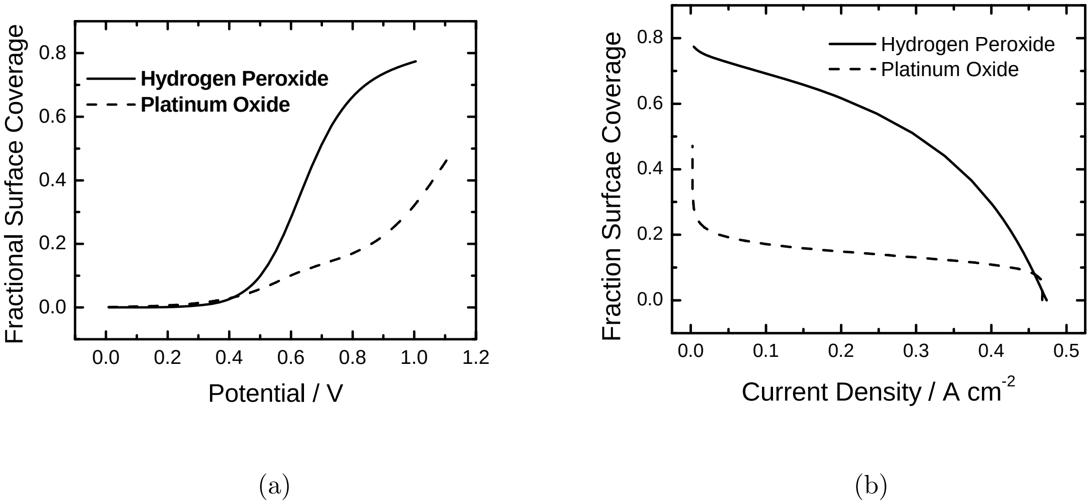

Figure 5-15: Fractional surface-coverage of the intermediates plotted a) as a function of cell potential; and b) as a function of current density.

Several authors have proposed that the low-frequency inductive loops could be attributed to relaxation of adsorbed intermediates species associated with cathodic reactions.[208, 144, 209] The present work shows that cathodic reactions involving formation of peroxide intermediates and reactions involving formation of PtO and subsequent dissolution of platinum can result in low-frequency inductive loops. An interesting aspect of Model 3 is that the inductive loop is controlled by formation of PtO. The corresponding low-frequency inductive loops can be seen even at very low rates of Pt dissolution. These interpretations are supported by a growing number of articles in the recent literature describing evidence of peroxide formation and platinum dissolution under normal PEM operating conditions.[87, 96–98, 93, 90, 99]

Models based on proposed reaction hypothesis can be used to gain insight into the reaction mechanism. For example, Models 2 and 3, respectively, invoked surface coverage by peroxide and PtO. The surface coverage predicted by these models is presented in Figures 5-15(a) and 5-15(b) as function of potential and current density, respectively. As shown in Figure 5-15(a), the fractional coverage of the intermediates in both the models increased with the increase in the cell potential. The presentation in Figure 5-15(b) as a function of current density shows that the fractional coverage of the intermediates decreases with increasing current.

The models presented in the present work, while based on plausible reaction mechanisms, are ambiguous. Both the reactions involving adsorbed peroxide and formation of PtO were capable of predicting the low-frequency inductive loops observed in the impedance response of the fuel cell. This work demonstrates the need to couple the impedance measurements with supporting experiments to identify the reactions taking place within the system.[218] Experimental results can be found in the literature that support both reaction mechanisms.

CHAPTER 6
RESULTS OF EX-SITU ANALYSIS

The evidence of the intermediates proposed for the model development in Chapter 5 is presented in this chapter.

6.1 Introduction

PEM fuel cells are electrochemical reactors that convert chemical energy into electrical energy. These are promising energy converters in the 21^{th} century because of their pollution free characteristic and high power density; however, several issues unresolved which have limited commercialization of this technology on a large scale. Durability and low performance is one of the issues which could arise from several factors such as side reactions and intermediates invloving peroxide formation,[7–9] catalyst deactivation evoked by platinum oxidation and dissolution,[10] catalyst support loss due to carbon corrosion,[11] water management issues including flooding, and drying[12] etc.

In Chapter 5, analytic impedance models were derived from consideration of specific reaction sequences proposed to take place in the fuel cell.[219] Two class of models, one with side-reaction and intermediate involving hydrogen peroxide formation, and other related to catalyst deactivation evoked by platinum oxide formation, were considered in the work. Both the models were capable of predicting the low-frequency inductive loops observed in the impedance response of the fuel cell. The models presented in the work, while based on plausible reaction mechanisms, are ambiguous. The work demonstrated the need to couple the impedance measurements with supporting experiments to identify the reactions taking place within the system.

The object of this work was to perform experiments which may provide an evidence of the proposed reaction mechanisms. The surface characteristic and morphological details of catalyst particles of the MEA was studied with the scanning electron microscope (SEM).[101,31] The TEM was used for atomic-scale micro-structural and chemical characterization of the MEA.[100,94,33] XPS (X- ray Photoelectron Spectroscopy) was utilized to study oxidation state of metals (platinum in catalyst layer). The XPS was used to inspect possible elements and compounds at the surface (5-15 atomic layers) of the MEA. The performance of the fuel cell was also investigated with time in form of polarization curves and impedance responses. ICP-MS (Inductively Coupled Plasma-Mass Spectroscopy) was applied to estimate platinum concentration[94] in effluent water of the fuel cell.

6.2 Experimental

The experimental system and the impedance instrumentation used are presented in this section.

6.2.1 Materials and Chemicals

The membrane electrode assembly (MEA) (purchased from Ion Power, Inc., New Castle, DE) employed 0.0508 mm (2 mils) thick Nafion N112 with catalyst layers of about 0.025 mm on both sides of the membrane. The active surface area was 5 cm^2. The catalyst layers were platinum supported on carbon with a Pt catalyst loading of 0.4 mg/cm^2 on both the anode and the cathode sides. The gas diffusion layer (GDL) used has an an effective thickness of 0.284 mm, and was made of carbon cloth with uniform macro-pores. The flow channel used was serpentine in configuration. The material of the flow channel was graphite with the outlet lower than the inlet to facilitate removal of condensed water. A torque of 45 inch-pounds was applied to the fuel cell assembly. Hydrogen gas was used as fuel and a 79% N_2 and 21% O_2 mixture was used as oxidant. Compressed N_2 was used to purge the fuel cell before and after experiments. A Barnstead E-Pure Water System with an ion resistivity of 14.9 MΩcm was used as a source of deionized water delivered to the anode and the cathode humidifiers.

An 850C fuel-cell test station (supplied by Scribner Associates, Southern Pines, NC) was used to control reactant flow rates and temperatures. The test station was connected to a computer by an interface for data acquisition. The gas flows were humidified to 100 percent relative humidity at the respective temperatures. The hydrogen flow rate was 0.1 liters/min, and the air flow rate was 0.5 liters/min. The maximum stoichiometry for hydrogen and air was 1.5 and 2.5, respectively, and the cell was operated at the fully-humidified condition.

6.2.2 Electrochemical Impedance Measurements

Impedance measurements were performed with the 850C fuel-cell test station, which contains an electronic load and impedance measurement capability. All electrochemical measurements were performed with a two-electrode cell. The anode was used as a pseudo-reference electrode. The impedance measurements were conducted in galvanostatic mode for a frequency range of 10 kHz to 5 mHz with a 10 mA peak-to-peak sinusoidal perturbation. The corresponding potential perturbation ranged from 0.04 mV to 0.4 mV. The perturbation amplitude selected was the largest amplitude that did not cause visible distortions in low-frequency Lissajous plots. The frequencies were spaced in logarithmic progression with 10 points per frequency decade. Impedance scans were conducted in auto-integration mode with a minimum of 2 cycles per frequency measured.

6.2.3 Aging Protocol for the Samples

The fresh sample was analyzed as received from the vendor. The aged sample was used in the fuel cell for a period of 3 months operating at various steady current loads for 9 hours/day of a total period of 600 hours.

6.2.4 Surface Analysis

Several microstructural characterizations techniques were employed to study the morphology, sintering, and oxidation state of elements in the cathode catalyst layer of the MEA.

6.2.4.1 Scanning electron microscope

For sample preparation, a small portion from the center of the both fresh and used MEA was cut with sharp razor and the SEM images were taken with the JOEL JSM 6400 available at MAIC in the University of Florida.

6.2.4.2 Transmission electron microscope

The TEM study was performed with a JOEL JSM-2010F Field Emission Electron Microscope available at MAIC in the University of Florida, which is equipped with an energy dispersive spectrometer (EDS) for compositional analysis. The TEM micrographs were taken at 200 kV accelerating voltage for several magnifications in bright field mode (transmitted electrons). Samples were prepared following procedure reported in literature.[193] A small portion from the center of the both fresh and used MEA was cut with sharp razor and was embedded on epoxy resin (Araldite 5002) for 48 hours at 60°C. Thin (90 nm) sections from the membrane-electrodes interfaces were cut with a diamond knife on Reichert OMU3 ultramicrotome at room temperature. The samples were mounted on Cu grid (mesh size 200) prior to TEM study.

6.2.4.3 X-ray photoelectron spectroscopy

The XPS was used to inspect possible elements and compounds at the surface (5-15 atomic layers) of the MEA. For sample preparation, a small portion from the center of the both fresh and used MEA was cut with sharp razor and the XPS scans were taken with the PHI 5100 ESCA system by Perkin-Elmer available at MAIC in the University of Florida. X-ray source was Mg anode with a work function 4.8 eV. The emitted electrons were collected at 45 ^{0} with respect to the sample. The sample was scanned at 300 watts power in energy range of 1000-0 eV (binding energy) with a step of 0.5 eV and 30 mSec/step. The survey (full scan) was generated at pass energy 89.45 eV whereas narrow scans (high resolution) for several peaks were performed at pass energy of 22.36 eV. The atoms were assigned according to binding energy of visible peaks and atomic composition of elements were evaluated by relatives intensities of the peaks.

6.3 Results

The results obtained from the surface analysis of the cathode surface, and supporting observation obtained from electrochemical response, and effluent analysis are presented in this section.

6.3.1 Microstructural Characterization

The full-scan XPS spectra is presented in Figure 6-1. It was discerned that the peak intensities of F, C was reduced in the used sample whereas the intensities of Pt and O were enhanced. The amount of carbon could decrease due to corrosion and enhanced amount of oxygen can be ascribed to surface oxidation of Pt in electrodes. An increase in the elemental composition of Pt and O was noticed in the used MEA, which could support the formation of PtO in the used MEA. A peak of PtO was detected in the spectra of used sample was recorded in during XPS investigation as shown in Figure 6-2. The analysis of spectra presented in Figure 6-2 were performed by 11 point, 2nd order, Savitsky-Golay smoothing followed by a Shirley background subtraction. This set the ends of the spectrum to a zero baseline and then the spectra were normalized. The two spectra were imported obtained from clean Pt(100) and 3 ML (monolayer) of atomic oxygen on Pt(100) from data presented by Shumbera *et al.*[220] XPS data does indicate oxide formation in the 1 to 3 ML range.

It is worth noting that the Pt 4f shoulder from the 3 ML oxide is small because the electron kinetic energy for that peak is large (1300 eV) when using a laboratory X-ray source which may be due to reduced surface sensitivity at lower binding energy.

TEM was applied to study agglomeration of catalyst particles; high-resolution TEM monograms presented in Figure 6-3 have showed bigger Pt particle size in case of used MEA as compared to fresh one. In the TEM images of cross-section of MEAs migration of Pt particles from cathode-membrane interface to membrane was observed. The TEM image of cross-section of fresh and used MEAs are presented in Figure 6-4. Changes in interface of the catalyst-membrane were evident.

The decrease in the surface area could be due to combined effect[101] of (i) metal catalyst cluster agglomeration or (ii) loss of support particles and metal cluster from the catalyst layer. Due to weak bonding of platinum particles with the carbon support, the formation of agglomerates of the catalyst particles are possible. The decreased

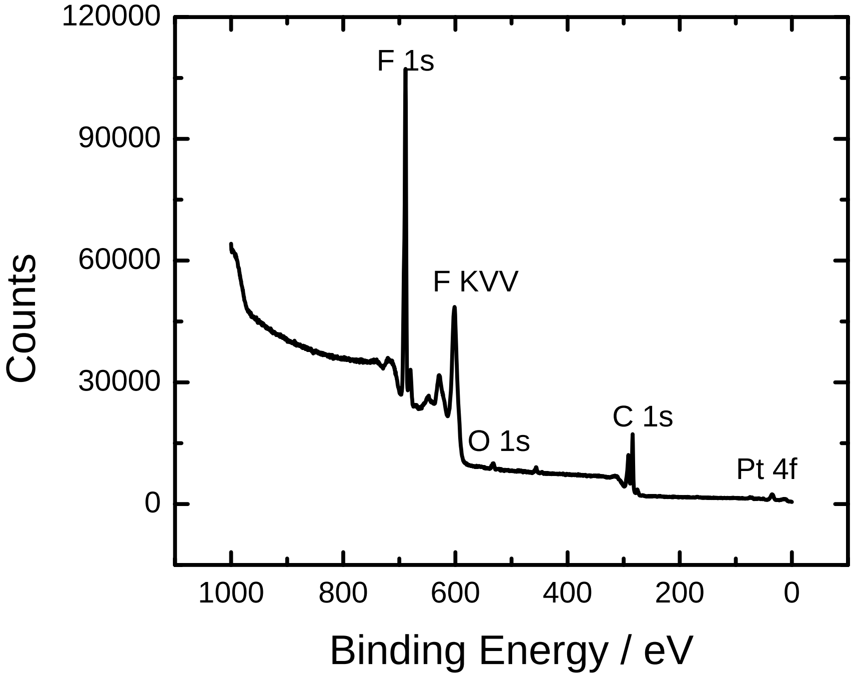

Figure 6-1: Full-scan XPS spectrum of the used sample generated at pass energy 89.45 eV. XPS scans were taken with the PHI 5100 ESCA system by Perkin-Elmer available at MAIC in the University of Florida. X-ray source was Mg anode with a work function 4.8 eV. The sample was scanned at 300 watts power in energy range of 1000-0 eV (binding energy) with a step of 0.5 eV and 30 mSec/step.

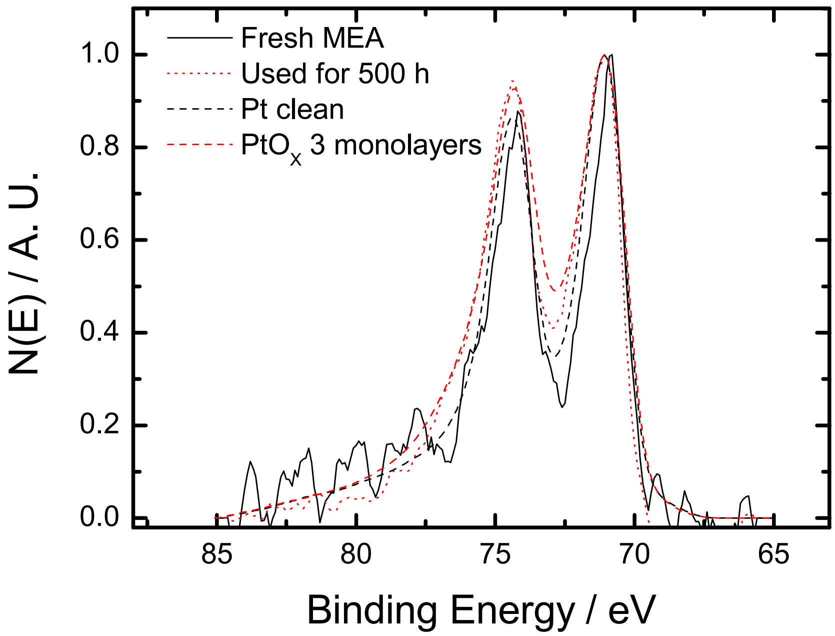

Figure 6-2: High resolution performed at pass energy of 22.36 eV of the XPS spectra on Pt peaks. XPS scans were taken with the PHI 5100 ESCA system by Perkin-Elmer available at MAIC in the University of Florida. X-ray source was Mg anode with a work function 4.8 eV. The sample was scanned at 300 watts power in energy range of 1000-0 eV (binding energy) with a step of 0.5 eV and 30 mSec/step.

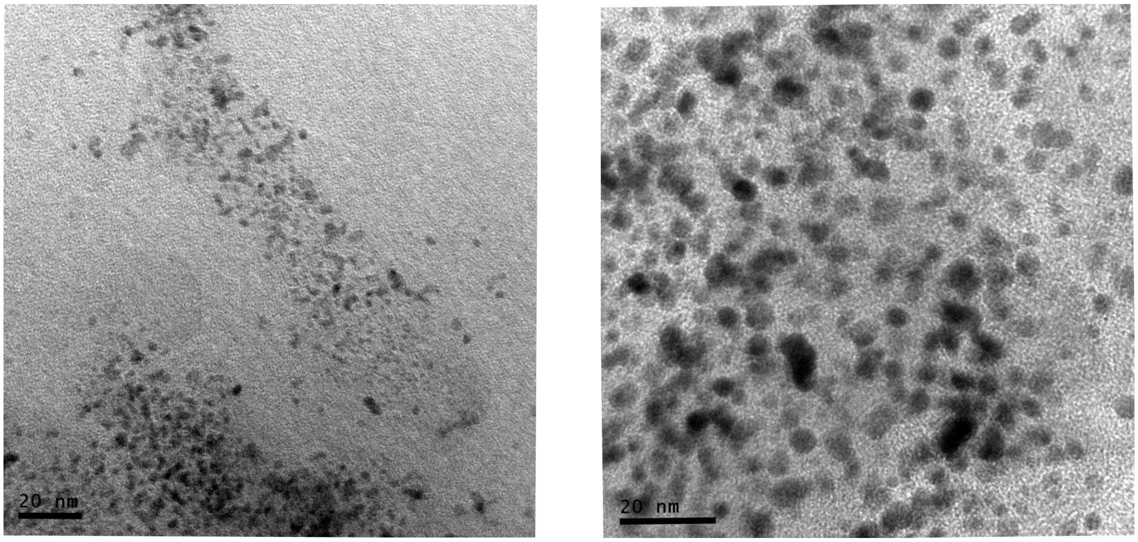

(a) (b)

Figure 6-3: TEM images of cathode surfaces. TEM study was performed with a JOEL JSM-2010F Field Emission Electron Microscope available at MAIC in the University of Florida. The TEM micrographs of cathode surfaces were taken at 200 kV accelerating voltage in bright field mode; a) fresh sample; and b) used sample.

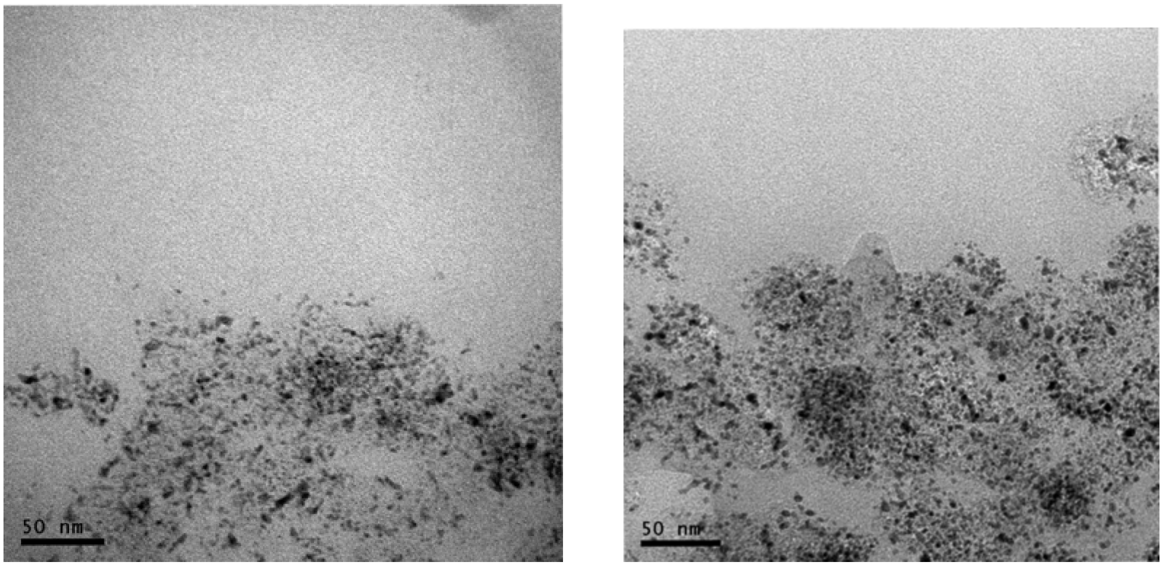

(a) (b)

Figure 6-4: TEM images of cross-section. TEM study was performed with a JOEL JSM-2010F Field Emission Electron Microscope available at MAIC in the University of Florida. The TEM micrographs were taken at 200 kV accelerating voltage in bright field mode;; a) fresh sample; and b) used sample.

surface area has also been attributed to the platinum dissolution and redepositing at the catalyst/ectrolyte interface.[100] The migration of the platinum particles to the membrane interface has also been reported.[94] Once the catalyst particle has migrated into the membrane, it would lose the electrical contact from the catalyst layer, which could also cause the loss of the electrochemical active surface area.

The SEM images of MEA cross sections are presented in Figure 6-5, in which the morphology changes in the interface of electrode-membrane can be clearly seen. Change in surface features was observed in the SEM images of surface the fresh (Figure 6-5(a)) and the used (Figure 6-5(b)) catalyst layer. These type of changes have been described as mud-cracking and surface erosion and have been explained as a result of catalyst particle or recast Nafion ionomer loss from the catalyst surface due to particle dissolution.[101]

6.3.2 Effluent Analysis

ICP-MS was used to analyze the effluent from the cathode of the fuel cell under operation at different points along the polarization curve. A trace amount of Pt was

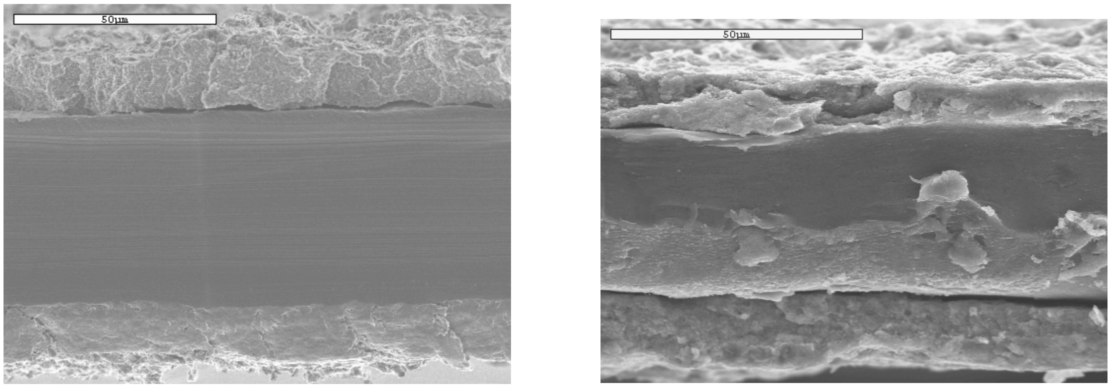

(a) (b)

Figure 6-5: SEM micrographs of cathode cross-section were taken at 15 kV accelerating voltage. The cross-section of the both fresh and used MEA was cut with sharp razor and the samples were coated with Au-Pd; a) fresh sample; and b) used sample.

estimated at a level of 15 ppb for the used sample against 6 ppb for blank sample. This result is in consistent with the literature. Xie *et al.* have also observed Pt in the cathode effluent by ICP-MS, and have attributed this result to Pt dissolution.[101,100] The dissolution is consistent with reaction scheme proposed by Darling *et al.*[10] which supports the formation of the platinum oxide as an intermediate.

6.3.3 Electrochemical Response

The performance of the fuel cell was also investigated with time in form of polarization curves and impedance responses. As presented in Figure 6-6, the a sharp decrease in the current density was observed with time especially apparent in the ohmic and mass transport regimes of the polarization.

The impedance response obtained at 0.2 A/cm^2 is presented in Figure 6-7. An overall increase in the impedance was recorded and also the different features in the impedance spectra were observed. The effect of the microstructural changes due to deactivation of the catalyst layer can be related to the observed performance loss in the polarization curve and higher impedance seen for the used sample. Furthermore, interfacial capacitance was estimated for the impedance data presented in Figure 6-7 following the procedure described in Chapter 8. The interfacial capacitance for the fresh sample was found as

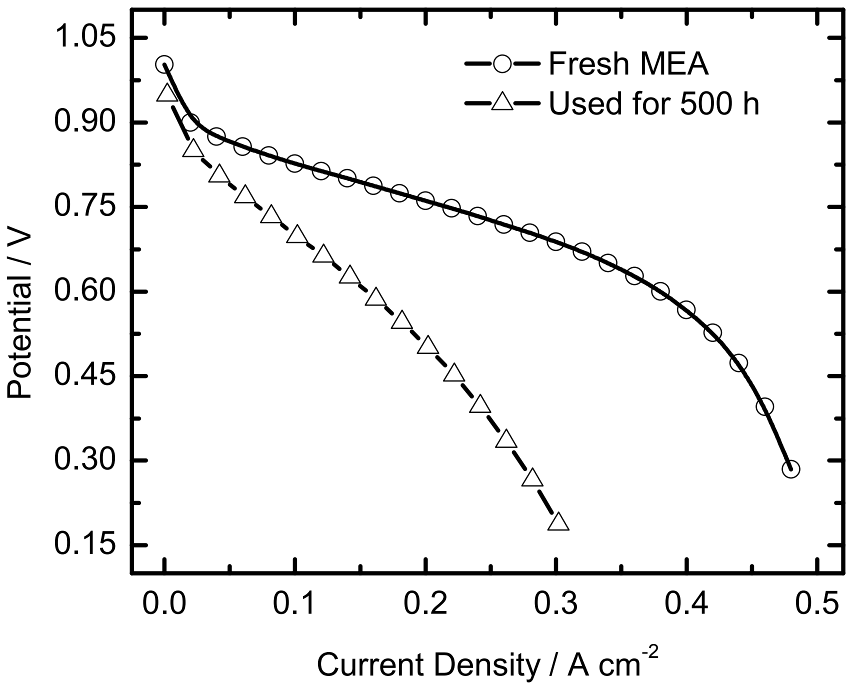

Figure 6-6: Polarization curve generated from the steady-state measurement for different time with 850C for H_2 as reactant at the anode and air as oxidant at cathode. The anode reactant stream and cell temperatures were set at 40 ^{0}C and the cathode reactant stream temperature at 35 ^{0}C. The fuel cell was assembled with a serpentine flow channel, and a uniform porous GDL.

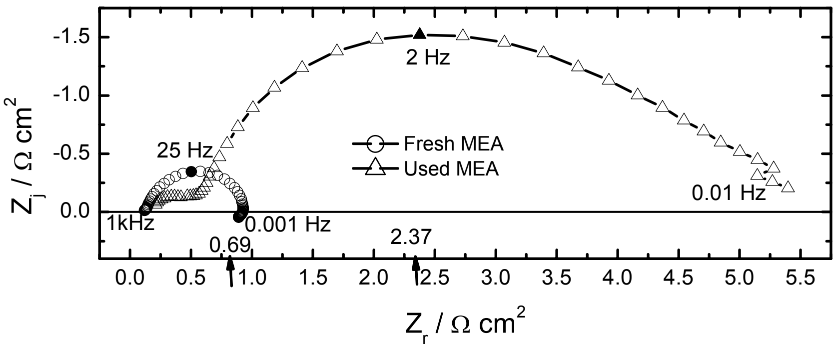

Figure 6-7: Impedance responses collected at at 0.2 A/cm^2 as a function of times a function of time with 850C for a function of time for H_2 as reactant at the anode and air as oxidant at cathode. The anode and the cell temperatures were set at 40 °C and the cathode temperature at 35 °C. The fuel cell was assembled with a serpentine flow channel, and a uniform porous GDL.

0.078 against 0.045 F/cm^2 for the used sample. The observed decrease in the interfacial capacitance can attributed to decrease in electrochemical area due to processes such as PtO oxide formation.

CHAPTER 7
DETECTION OF ONSET OF FLOODING

Impedance spectroscopy in conjunction with the measurement model analysis was used to gain an insight into the problem of flooding which adversely affects the performance of the fuel cell. The approach demonstrates how the stochastic character of flooding may be exploited to detect onset of flooding without the need to regress impedance spectra. The research presented has potential to give guidelines for efficient fuel-cell operation.

7.1 Introduction

Flooding increases the resistance associated with the gas diffusion layer and may even block flow channels, reducing the availability of oxygen.[149] Condensed water may be removed by gas flow. Thus, changes in reactant flow channel design have been proposed to reduce the flooding.

The object of the present work was to explore how the stochastic character of flooding can be exploited to improve sensitive of impedance spectroscopy to detect onset of flooding. Impedance measurements were performed as a function of different parameters such as current density, temperature, and time. A comprehensive model for base-level noise in impedance measurements for normal conditions (non-flooded) was developed by a measurement model analysis,[124,125,221,222,194] and stochastic errors were also assessed by transient fixed-frequency measurements. A comparison of the actual noise to the base-level noise was used to detect onset of flooding.

7.2 Results

The influence of flooding on the operation of the fuel cell was investigated using impedance spectroscopy. The results of frequency scan and single-frequency time-dependent measurements are presented in following sections.

7.2.1 Impedance Response

A typical impedance response is presented in Figure 7-1 with current density as a parameter. The size of the intermediate-frequency and the low-frequency arcs increased

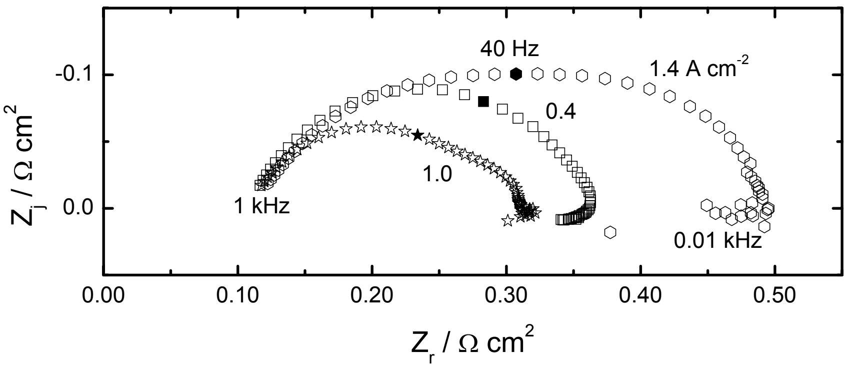

Figure 7-1: Impedance data recorded with the 850C with applied current density as a parameter. The anode, cathode, and cell temperatures were set to 50 °C.

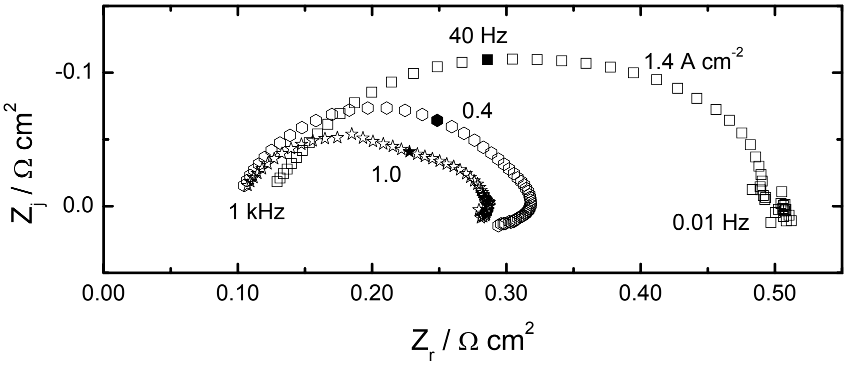

Figure 7-2: Impedance data recorded with the 850C with applied current density as a parameter. The anode, cathode, and cell temperatures were set to 70 °C.

with increasing current density, an effect which was suggested in the literature[12,157] to be due partially to flooding. The impedance spectra were relatively smooth for low current densities; however, the spectra have significant scatter at higher current densities where flooding was probable. The scatter was particularly evident at low frequency, where the spectra show jumps in value which may be associated with removal of condensed water. Similar results were observed at other temperatures. The impedance measured at 70 °C is presented in Figure 7-2 with current density as a parameter. Here also the impedance data have greater degree of scatter at higher current densities, and this scatter is particularly evident at lower frequencies.

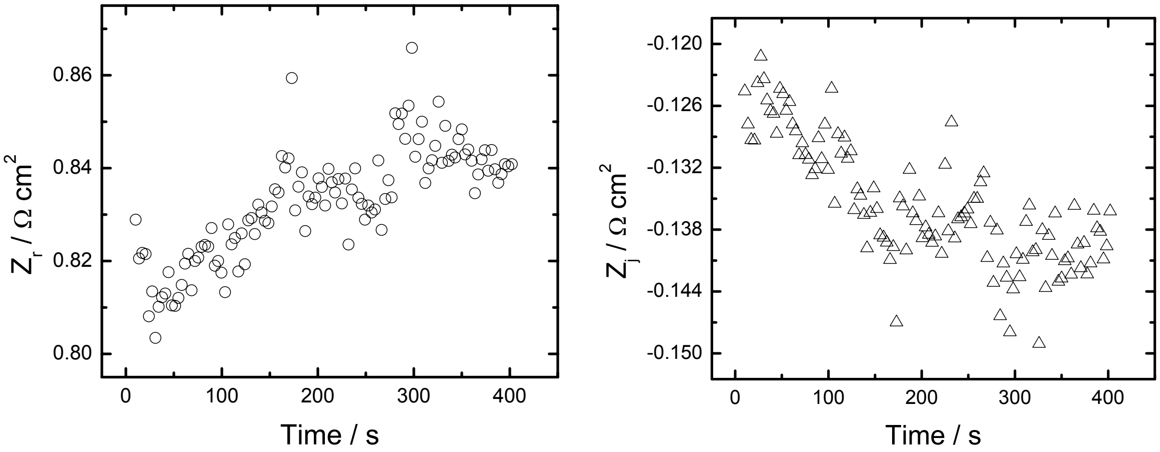

(a)

(b)

Figure 7-3: Single-frequency Impedance measurements recorded at 0.1 Hz, 70 °C, and 1.4 A/cm^2 as functions of time: a) real part; and b) imaginary part.

7.2.2 Stochastic Error in Impedance Response

The standard deviations of the stochastic errors were estimated from both impedance spectra and single-frequency transients for dry, flooded, and non-flooded conditions.

7.2.2.1 Sensitivity to flooding

The impedance was recorded as a function of time for different current densities and fixed-frequencies. For example, the real and imaginary parts of impedance at 0.1Hz and 1.4 A/cm^2 are presented as functions of time in Figures 7-3(a) and 7-3(b), respectively. The standard deviations in the impedance data were calculated using a moving average method to account for the systematic changes shown in Figure 7-3. The standard deviations for the real and imaginary parts of the impedance response are presented in Figure 7-4(a) for a measured frequency of 100 Hz and in Figure 7-4(b) for a frequency of 1 Hz. At low frequencies, Figure 7-4(b), the standard deviation of the real part of the impedance is clearly larger than that of the imaginary part. The solid line given in Figure 7-4 represents the model value for the standard deviation, developed in a subsequent section for non-flooded conditions.

The standard deviations for the real part of the impedance are presented as a function of current density in Figure 7-5 for frequencies of 0.1, 10, and 100 Hz. The

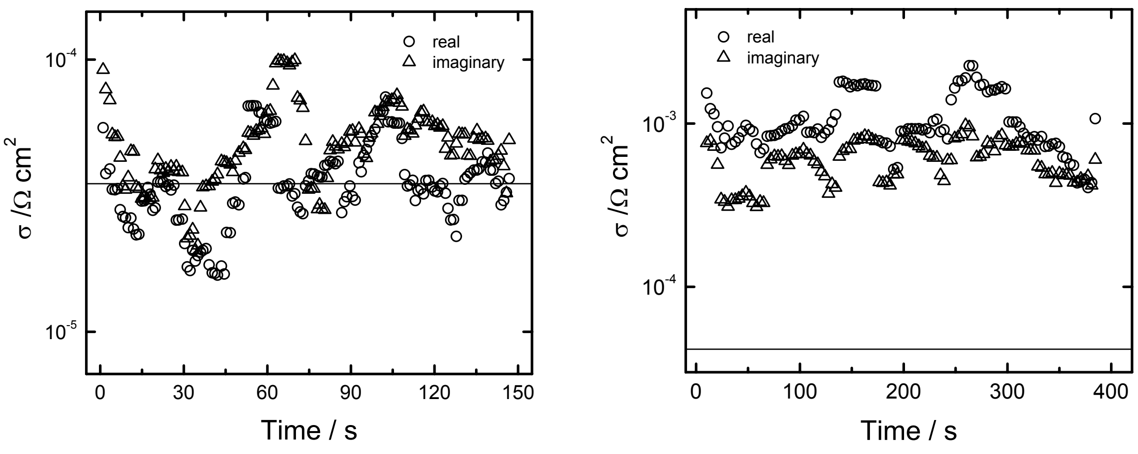

(a) (b)

Figure 7-4: The standard deviation of the single-frequency Impedance measurements recorded at 1.4 A/cm^2 and 70 °C as functions of time: a) at a frequency of 100 Hz; and b) at a frequency of 1 Hz (as presented in Figure 7-3). The solid line represents the empirical model developed for the error structure given by equation (7–1).

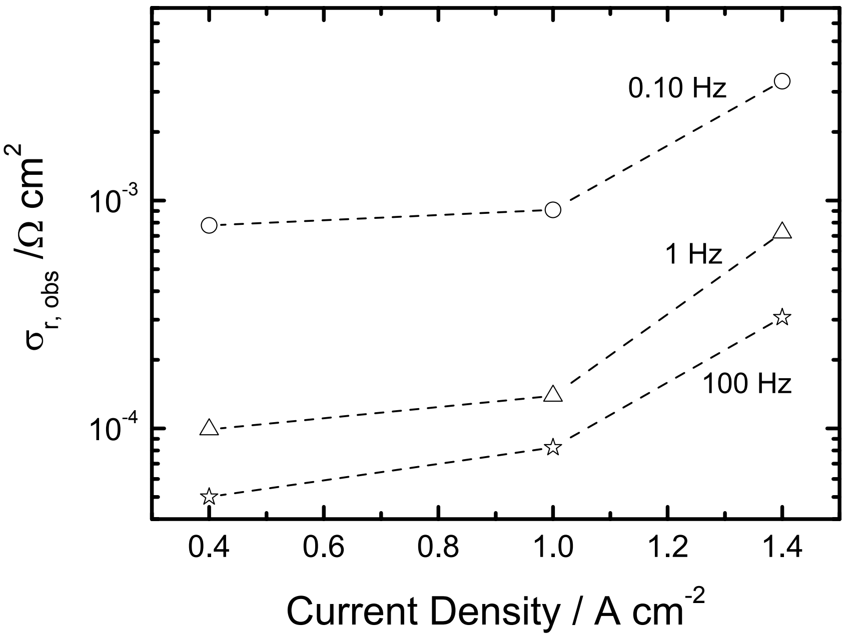

Figure 7-5: The standard deviations for the real part of the impedance as a function of current density with frequency as a parameter for cell operation at 70 °C.

stochastic errors in the impedance increased with increasing current density, in particular for the lower frequencies of 0.1 and 10 Hz. The standard deviation at lower frequencies are higher than that at higher frequencies for any given current density.

The statistical nature of the error structure may be used to explain the larger standard deviation observed at larger current densities. As shown in Figure 7-4(b), the standard deviation of the real part of the impedance at 1 Hz was much higher as compared to imaginary part. The results presented in Figure 7-4(a) indicate that at 100 Hz, the standard deviation of real and imaginary parts of the impedance were also unequal, but the imaginary part of the impedance seems to have the larger standard deviation. For causal systems which satisfy the Kramers-Kronig relations, the standard deviation in the real and imaginary parts should be equal.[223] The literature indicates that, at low frequencies, the real part of the impedance is more sensitive to flooding;[12,116] therefore, the higher standard deviation of the real part of the impedance observed at low frequencies may be attributed to onset of flooding.

7.2.2.2 Baseline error structure

To establish a baseline error-structure model for the standard deviation of impedance measurements in the absence of flooding, a measurement model analysis[124,125,221,194] was applied to a large set of replicated impedance data. The measurement model was used to filter small systematic changes from one measurement to the other. The standard deviations for impedance response recorded at 0.4 A/cm^2, presented in Figure 7-6, were smaller than those observed at both larger and at smaller current densities. The real and imaginary parts of the impedance were statistically indistinguishable at all frequencies, in agreement with expectations for data that are consistent with the Kramers-Kronig relations.

The model for error structure developed in previous work for a broad variety of electrochemical and electronic systems[135,210] did not provide a good representation of the error structure presented in Figure 7-6. The failure of the general model to apply

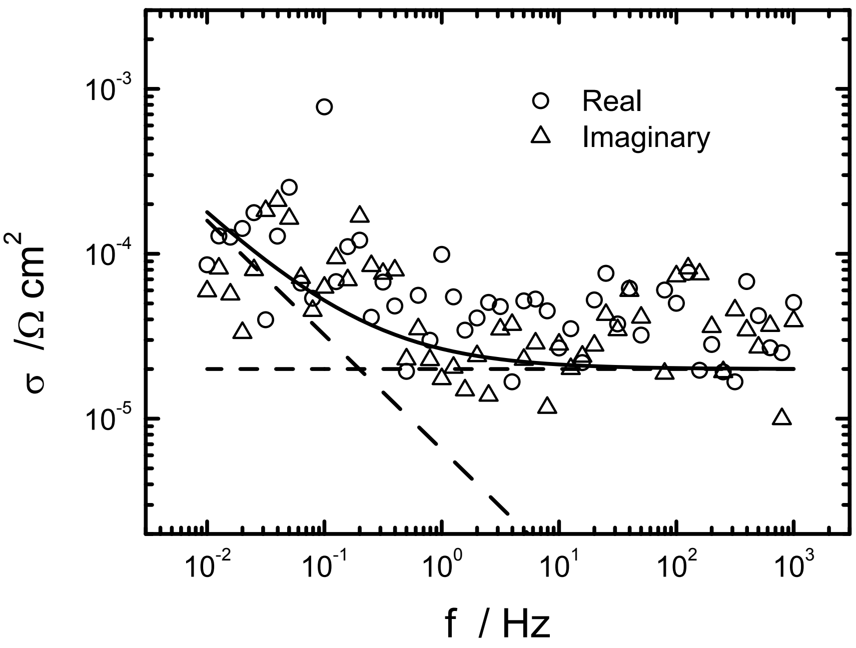

Figure 7-6: Standard deviations for the impedance data obtained at a current density of 0.4 A/cm^2. The solid line represents the empirical model developed for the error structure given by equation (7–1). The dashed lines represent the asymptotic behavior of the model at high and low frequencies.

to the present data was attributed to differences in the parameters used to make the measurement. An empirical model was found to follow the form

$$\sigma_r = \sigma_j = c + |Z_{r,\max}|(af^{-b}) \tag{7–1}$$

where $a = 9 \times 10^{-5}$, $b = 0.695$, and $c = 3.5 \times 10^{-5}$. The model can be rationalized by examination of the standard formula for propagation of stochastic errors, which can be written for impedance as

$$\sigma_Z^2 \cong \sigma_I^2[\frac{\partial Z}{\partial \Delta I}]^2 + \sigma_V^2[\frac{\partial Z}{\partial \Delta V}]^2 \tag{7–2}$$

where ΔI, and ΔV are perturbations in current, and potential respectively, and Z is the impedance given as

$$Z = \frac{\Delta V}{\Delta I} \tag{7–3}$$

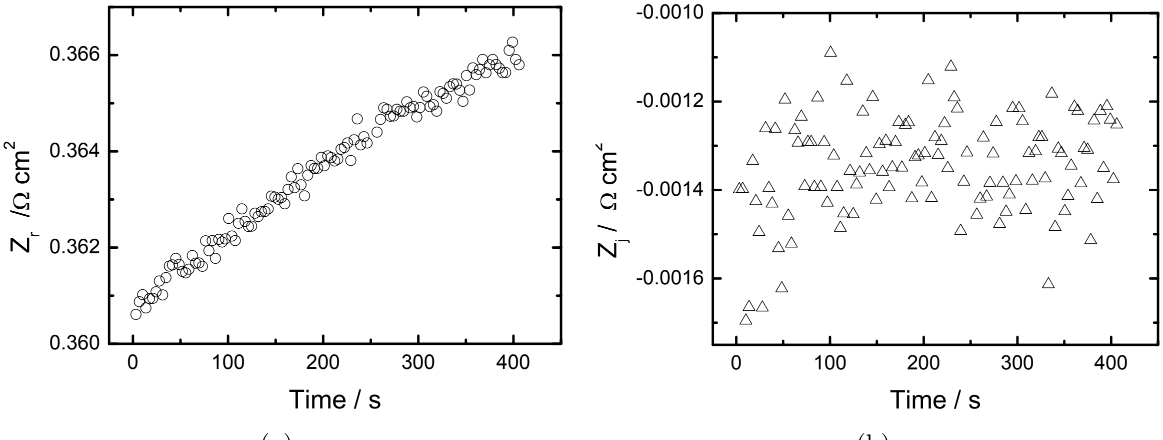

(a) (b)

Figure 7-7: Impedance measurement recorded at 0.4 A/cm^2 and 1 Hz as functions of time at 70 °C: a) real part; and b) imaginary part.

Equation (7–2) can be written as

$$\sigma_Z^2 \cong \sigma_I^2[\frac{\Delta V}{\Delta I^2}]^2 + \sigma_V^2[\frac{1}{\Delta I}]^2 \tag{7–4}$$

or

$$\sigma_Z^2 \cong \frac{\sigma_I^2}{\Delta I^2}Z^2 + \sigma_V^2[\frac{1}{\Delta I}]^2 \tag{7–5}$$

For galvanostatic modulation at fixed amplitude, equation (7–5) takes the form

$$\sigma_Z \cong B|Z| + C \tag{7–6}$$

where C, and B are constants.

The error structure identified for impedance spectra can be compared to that obtained for single-frequency transient measurements such as presented in Figure 7-7 for impedance data collected at 0.4 A/cm^2 and 1 Hz. The standard deviations for the real and imaginary parts of the impedance response are presented in Figure 7-8(a) for a measured frequency of 100 Hz and in Figure 7-8(b) for a frequency of 1 Hz. The error structure model represented by equation (7–1) is in good agreement with the standard deviations obtained by transient single-frequency measurements. At 100 Hz, Figure 7-8(a), the standard deviation of the real and imaginary parts of the impedance are equal;

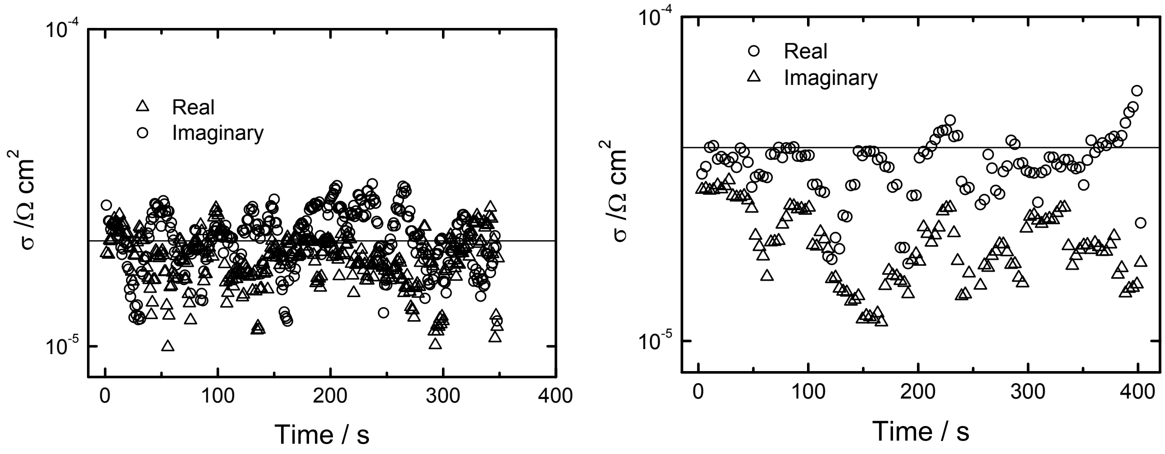

(a) (b)

Figure 7-8: The standard deviation of the single-frequency Impedance measurements recorded at 0.4 A/cm^2 and 70 °C as functions of time: a) at a frequency of 100 Hz; and b) at a frequency of 1 Hz (as presented in Figure 7-7). The solid line represents the empirical model developed for the error structure given by equation (7–1).

however, as shown in Figure 7-8(b), the standard devaitions for real and imaginary parts are not equal at a frequency of 1 Hz. This result suggests that, even at a current density of 0.4 A/cm^2, where the error structure was the smallest, some flooding may be taking place.

Equation (7–1) provided a good representation of the impedance error structure obtained at a current density of 0.4 A/cm^2 under a broad variety of conditions. The error structure for the impedance response collected at different temperatures is presented in Figure 7-9(a) and the influence of anode/cathode back-pressure is explored in Figure 7-9(b). The model provided a good representation of the error structure for all cases considered in Figure 7-9. Accordingly, equation (7–1) was used to represent the base-level standard deviation for measurements unaffected by drying or flooding conditions.

7.2.2.3 Detection of flooded conditions

Impedance spectra were obtained at different current densities. The standard deviations obtained at larger current densities are compared in Figure 7-10 to the values obtained at 0.4 A/cm^2. The standard deviations obtained for current densities of 1.0 and

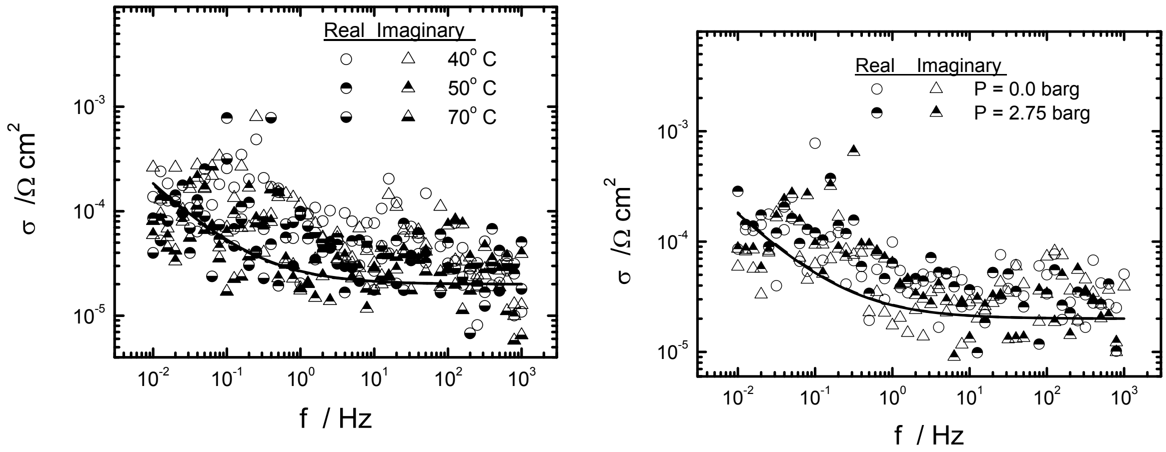

(a) (b)

Figure 7-9: Standard deviations for the impedance data obtained at a current density of 0.4 A/cm^2: a) with system temperature as a parameter; and b) at 70 °C with anode/cathode back-pressure as a parameter. The solid line represents the empirical model for the error structure given by equation (7–1).

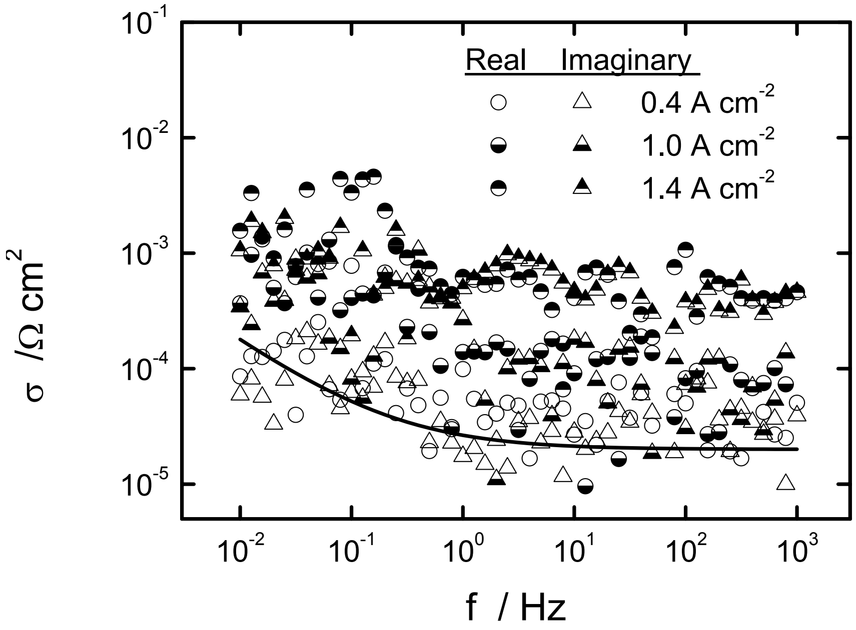

Figure 7-10: Standard deviations for the impedance data obtained at a current densities of 0.4, 1.0, and 1.4 A/cm^2. The solid line represents the empirical model for the error structure given by equation (7–1).

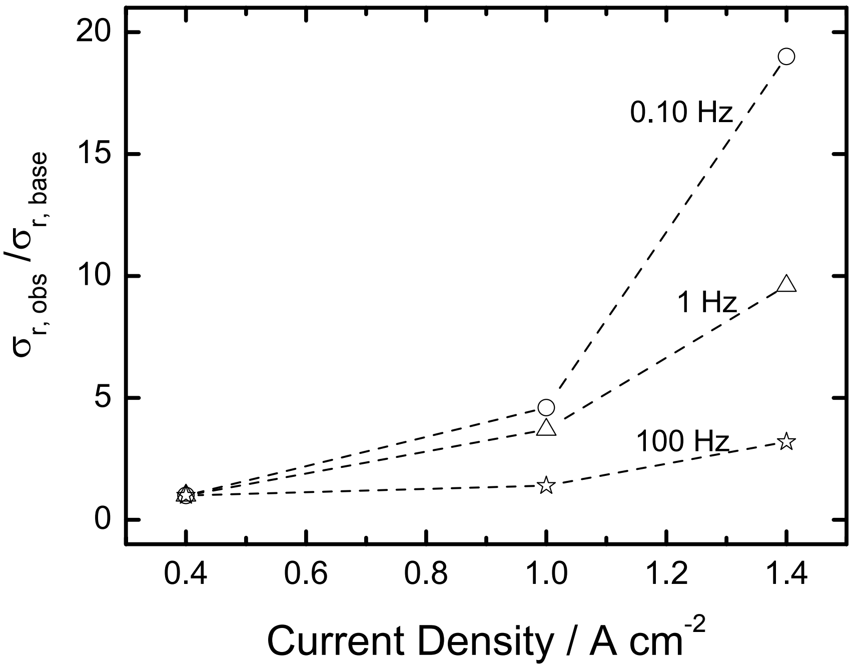

Figure 7-11: Normalized standard deviations for the real part of the impedance calculated from the data shown in Figure 7-3 as a function of current density with frequency as a parameter.

1.4 A/cm^2 are clearly larger than that predicted by equation (7–1). The discrepancy may be attributed to stochastic processes within the cell such as associated with flooding.

The standard deviations presented in Figure 7-5 were normalized by the base-stochastic errors level calculated using the error structure presented by equation (7–1). The result for the real part of the impedance is presented in Figure 7-11. As shown in Figure 7-11, the standard deviation of the impedance data increased with an increase in the operating current. The increased noise levels are seen at a frequency of 100 Hz as well as at lower frequencies. At large current densities and at low frequencies, the standard deviation calculated for the real part of the impedance was more than 20 times that obtained in the absence of flooding. The standard deviation of the imaginary part of the impedance had no clear dependency on flooding. The standard deviation of the real part particularly at low frequency, however, can be used to detect onset of flooding.

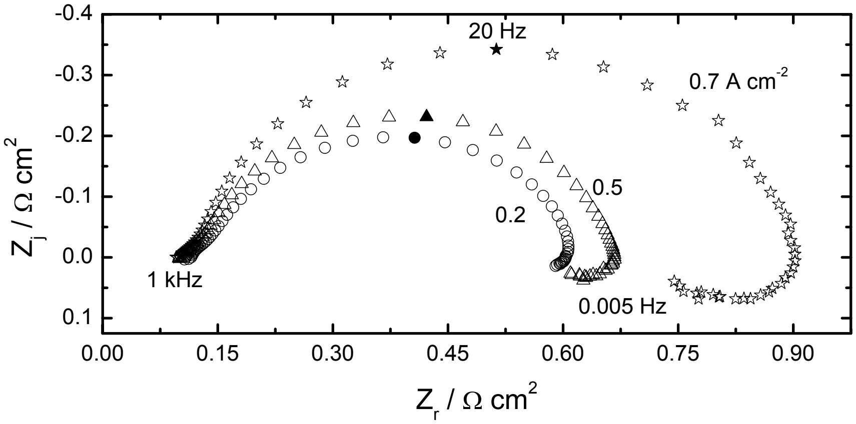

Figure 7-12: The impedance data recorded using the MEA with a uniform GDL. The anode, the cathode, and cell temperatures were set at 50 °C.

Similar experiments and analysis were performed on the MEA with a uniform GDL. The impedance response is presented in Figure 7-12 with current density as a parameter. The scattering at higher current densities was more evident than observed for experiments using the non-uniform GDL. Transient single-frequency impedance measurements were used to obtain the standard deviations for real and imaginary parts of the impedance. The standard deviation for the real part of the impedance is presented in Figure 7-13 as a function of current density for frequencies of 0.1, 10, and 100 Hz. The base-line error structure model used to normalize the data was calculated at a current density of 0.2 A/cm^2.

7.2.2.4 Detection of dry conditions

The stochastic errors for small current densities are shown in Figure 7-14 for the MEA with a non-uniform pore distribution. The empirical model given by equation (7–1) provided a good description for the behavior at a current density of 0.4 A/cm^2, but the observed errors are much larger for lower current densities where dry conditions are anticipated. This result is consistent with the experimental observations of Schneider *et al.*[155] who report impedance scans with large scatter at low frequencies for dry conditions. The standard deviation of the real part particularly at low frequency, however, can be used as well to detect the presence of dry conditions.

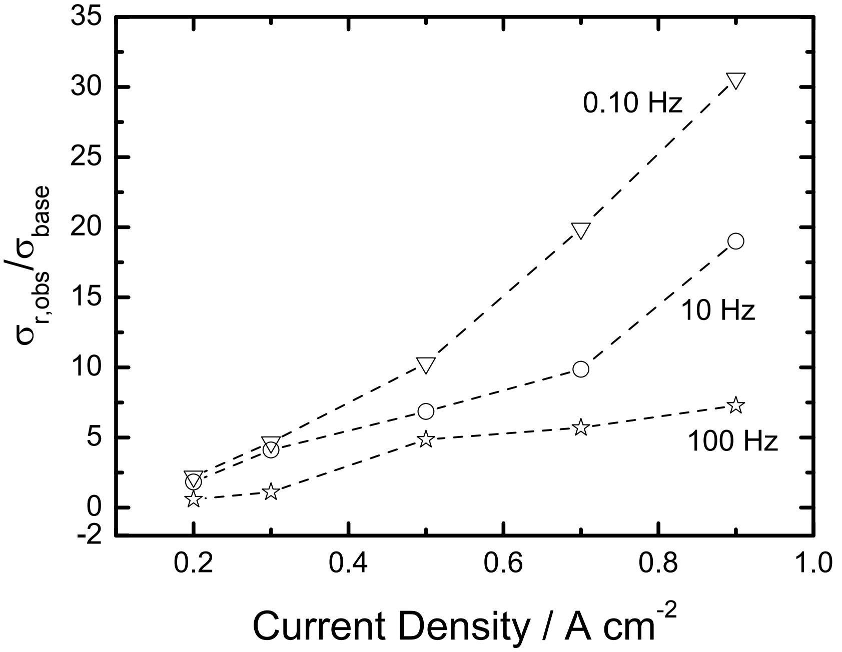

Figure 7-13: Normalized standard deviations for the real part of the impedance as a function of current density with frequency as a parameter for the MEA with a uniform pore distribution. The anode, the cathode, and cell temperatures were set at 50 °C.

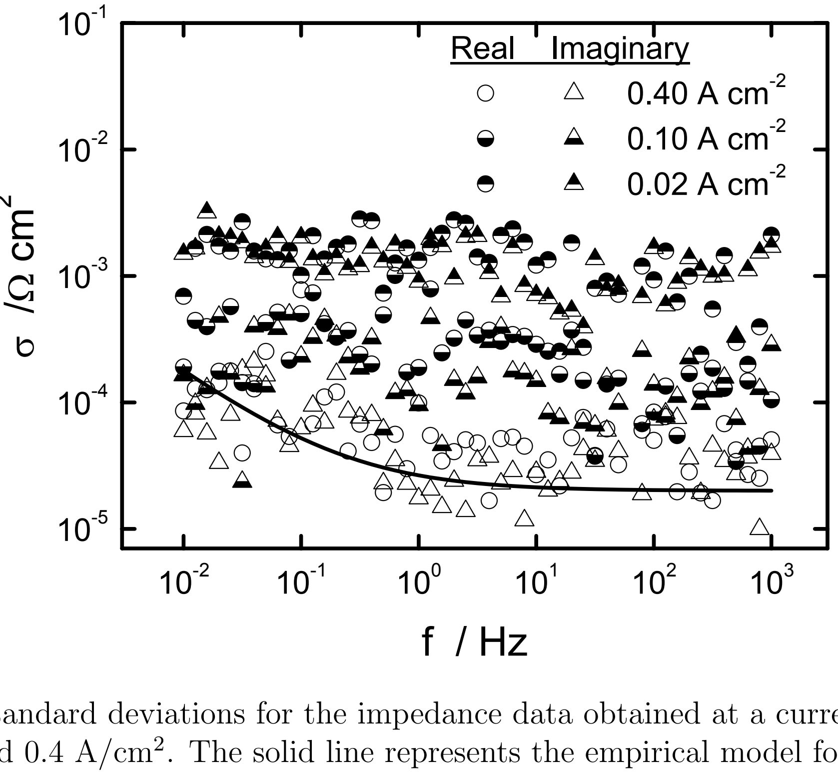

Figure 7-14: Standard deviations for the impedance data obtained at a current densities of 0.02, 0.1, and 0.4 A/cm^2. The solid line represents the empirical model for the error structure given by equation (7–1). The anode, the cathode, and cell temperatures were set at 70 °C.

7.3 Discussion

Due to its influence on mass transfer and kinetics, the onset of flooding in the fuel cell can be identified by a decrease in cell potential at fixed current or a decrease in current at fixed potential. Similarly, the onset of flooding can be identified by an increase in the cell impedance. In the present work, the increase in the low-frequency cell impedance associated with flooding was on the order of 10 percent. The increase of 10 percent in the cell impedance was accompanied by an increase in the standard deviation of the real part of the impedance by 2000 or 3000 percent.

The increase in stochastic errors in the impedance measurement can be attributed to the random character of the flooding process in which droplets of water are formed and then removed by gas flow. In fact, the increase in stochastic errors provides verification that the increased cell impedance was at least partially due to flooding. Impedance spectroscopy has been shown to provide a more sensitive assessment of cell condition than steady-state measurements of cell potential and current. The difficulty with using impedance directly to detect flooding is that a baseline value for the impedance must be established in the absence of flooding. This baseline must, however, change with time due to systematic changes to catalyst and membrane properties that are not associated with flooding. Thus, a baseline established when a cell is first commissioned will not be valid throughout the lifetime of the cell.

In contrast, the model given by equation (7–1) for the standard deviation of the impedance should be affected largely by instrumental settings, and, so long as the impedance is measured in the same way, a baseline established for the standard deviation of impedance measurements in the flooded condition should be valid throughout the lifetime of the cell. In addition, the change in the standard deviation of the measurement caused by flooding is 100 times larger than the corresponding change in the value of the impedance. Thus, assessment of the standard deviation of impedance measurements will provide a more sensitive indicator for the onset of flooding in a PEM fuel cell.

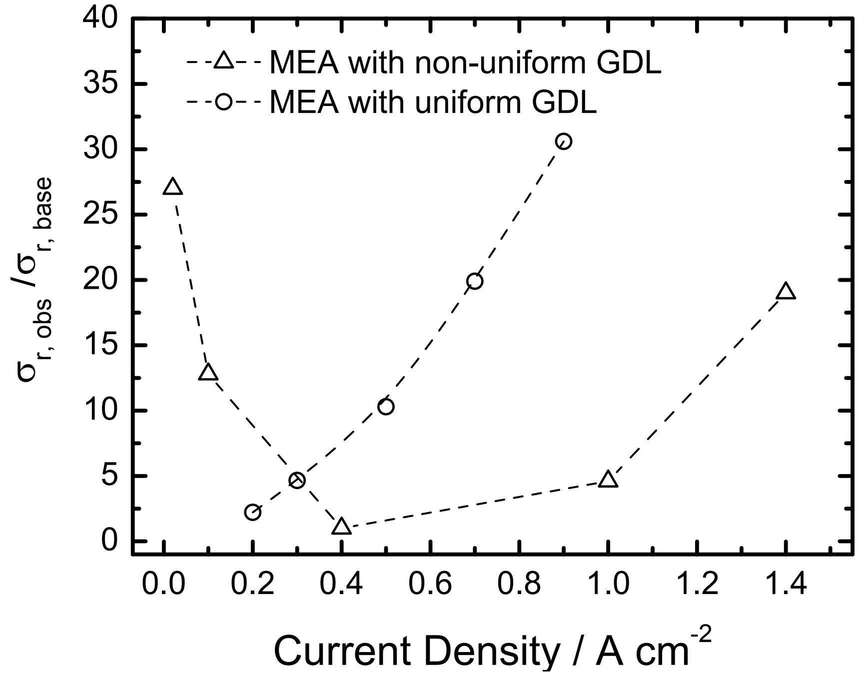

Figure 7-15: Normalized standard deviations for the real part of the impedance measured at 0.1 Hz for fuel cells containing two different MEAs as a function of current density. The experiments for the uniform MEA were performed at 50 °C, and the experiments for the nonuniform MEA were performed at 70 °C.

The standard deviation of the impedance measurements were sensitive to the properties of the MEA used in the experiment. A comparison of the normalized standard deviations for the real part of the impedance is presented in Figure 7-15 with GDL properties as a parameter. The experiments for the uniform MEA were performed at 50 °C, and the experiments for the nonuniform MEA were performed at 70 °C. The normalized standard deviation increased at lower current densities for the GDL with a uniform pore distribution. The value was closer to unity over a broader range for the GDL with a nonuniform pore distribution. The results are consistent with the observation that a larger maximum current density could be obtained with the nonuniform GDL. Micro-macro porous GDLs are reported to provide better water management.[64–66] The increase in normalized standard deviation at low current densities observed for the non-uniform GDL is likely due to drying of the membrane.[152,12] Similar experiments were not performed for the uniform GDL.

CHAPTER 8
EVALUATION OF INTERFACIAL CAPACITANCE

Graphical methods were used to extract values of CPE parameters and interfacial capacitance from impedance data collected on a PEM fuel cell. The impedance data were recorded as a function of current density, time, temperature, backpressure, and flow channel and gas diffusion layer design. The value of the interfacial capacitance was reduced when the cell was operated under dry or flooded conditions. The interfacial capacitance decreased with time over a timescale consistent with the approach to a steady state. In addition to providing an insight into physical processes, the parameters obtained from graphical methods can be used for model reduction when regressing impedance data. The methodology presented can be applied to any electrochemical system on which impedance measurements can be conducted.

8.1 Introduction

Use of CPE parameters is frequent, though parameters estimated by fitting circuit models to impedance data are not unique. The object of this work was to use the graphical methods described by Orazem *et al.*[224] to evaluate the influence of operation and design parameters on the interfacial capacitance of a PEM fuel cell. The transient behavior of CPE parameters was also investigated. The parameters obtained by the graphical methods were used to explore processes such as flooding, drying, and catalyst deactivation in the fuel cell.

8.2 Results

Typical impedance results are presented in Figure 8-1 with current density as a parameter. The measurement model developed by Agarwal *et al.*[124,125,221,222] was used to analyze the error structure of the impedance data.[194,225] As shown by Roy and Orazem,[194] data collected above a frequency of 1 kHz were inconsistent with the Kramers-Kronig relations. This inconsistency was attributed to instrumental artifacts. Once a steady operation had been achieved, the data collected at frequencies as low as 1 mHz were found to be consistent with the Kramers-Kronig relations. Data found to be inconsistent with

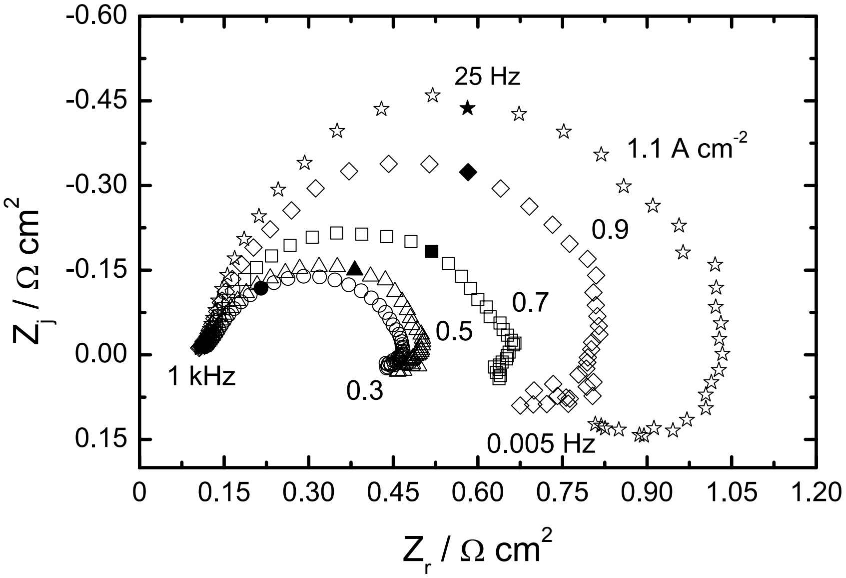

Figure 8-1: Impedance response recorded at 70 °C with current density as a parameter. The fuel cell was assembled with a non-uniform GDL and an interdigitated flow channel.

the Kramers-Kronig relations were removed from the data set used for further analysis. For the transient measurements obtained at 0.02 A/cm^2 (see Figure 8-11), the data at frequencies above 500 Hz were inconsistent with the Kramers-Kronig relations. For all other measurements, the data were consistent with the Kramers-Kronig relations at frequencies below 1 kHz.

8.2.1 Application of Asymptotic Graphical Analysis

CPE parameters were estimated for data found to be consistent with the Kramers-Kronig relations using the graphical methods illustrated by Orazem *et al.*[224] The CPE exponent α was calculated from the slope at high frequency of a logarithmic plot of the absolute value of the imaginary part of the impedance as a function of frequency, shown in Figure 8-2(a)). The resulting value of α is presented in Figure 8-2(b) as a function of current density. An increase in α was observed with an increase in current density.

Given the value of α presented in Figure 8-2(b), the CPE coefficient Q_{eff} could be calculated from

$$Q_{\text{eff}} = \sin(\frac{\alpha\pi}{2})\frac{-1}{Z_j(2\pi f)^\alpha} \tag{8–1}$$

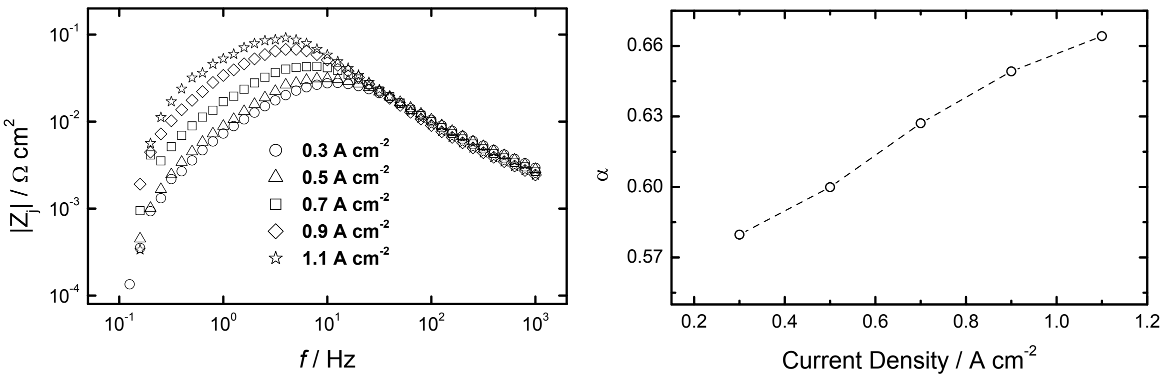

(a) (b)

Figure 8-2: Representation of the graphical analysis of the data presented in Figure 8-1 to obtain the CPE exponent α: a) the magnitude of the imaginary part of the impedance as a function of frequency with current density as a parameter; and b) CPE exponent obtained from the slope of part (a) at high frequencies.

as proposed by Orazem *et al.*,[224] where Z_j is the imaginary part of the impedance, and f is the frequency in units of Hz. The value of Q_{eff} is presented in Figure 8-3(a) as a function of frequency with current density as a parameter. The frequency dependence of the apparent CPE coefficient, evident at frequencies below 50 Hz, is caused by Faradaic and transport processes. Faradaic and transport processes have negligible influence at higher frequencies. The value of Q_{eff} was obtained by estimating the high-frequency asymptote of Figure 8-3(a) by calculating the average of the 10 values at the highest frequencies.

The interfacial capacitance C_{eff} was calculated by

$$C_{\text{eff}} = [Q_{\text{eff}} R_e^{1-\alpha}]^{\frac{1}{\alpha}} \tag{8–2}$$

as derived by Brug *et al.*,[158] where R_e is the electrolyte resistance calculated from the high-frequency part of the impedance data presented in Figure 8-1. In a comparison of expressions developed by Hsu and Mansfeld[226] and Brug *et al.*,[158] Huang *et al.*[171] found that equation (8–2) provided an excellent assessment of interfacial capacitance for systems for which the CPE behavior originated from nonuniform current and potential distributions along the electrode surface. Values of interfacial capacitance C_{eff} obtained

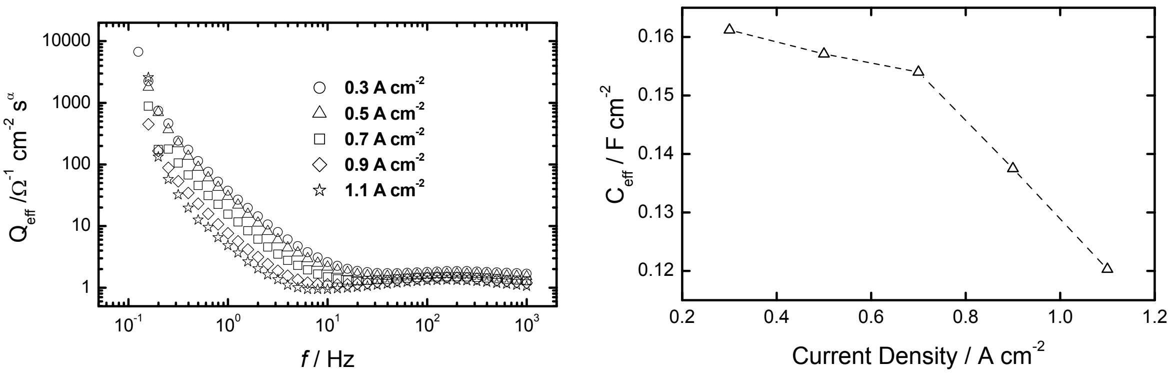

(a) (b)

Figure 8-3: Representation of the graphical analysis of the data presented in Figure 8-1 to obtain the CPE coefficient Q_{eff} and the interfacial capacitance C_{eff}: a) CPE coefficient obtained from equation (8–1); and b) the interfacial capacitance obtained from equation (8–2).

from equation (8–2) are presented in Figure 8-3(b) as functions of current density. A decrease in C_{eff} was observed with increasing current density.

To investigate the influence of the state-of-health (drying and flooding) of the fuel cell, similar analyses were performed over a broader range of current densities and as a function of time. The corresponding values obtained for Q_{eff} are presented in Figure 8-4 with time as a parameter. The CPE coefficient Q_{eff} was significantly lower at small current densities, where localized drying of the MEA could be expected due to reduced production of water at the cathode coupled with redistribution by electro-osmosis. The CPE coefficient was also reduced at large current densities which are associated with flooding. The largest value of Q_{eff} was found at intermediate current densities. At all current densities for which the effect of time on Q_{eff} was explored, the value of Q_{eff} decreased with time.

The corresponding values for interfacial capacitance C_{eff}, obtained from equation (8–2), are presented in Figure 8-5 as a function of current density with time as a parameter. The behavior of the interfacial capacitance was consistent with that found for the CPE coefficient. It should be noted, however, that the numerical value for interfacial capacitance reported in Figure 8-5 is significantly different from the numerical value of the

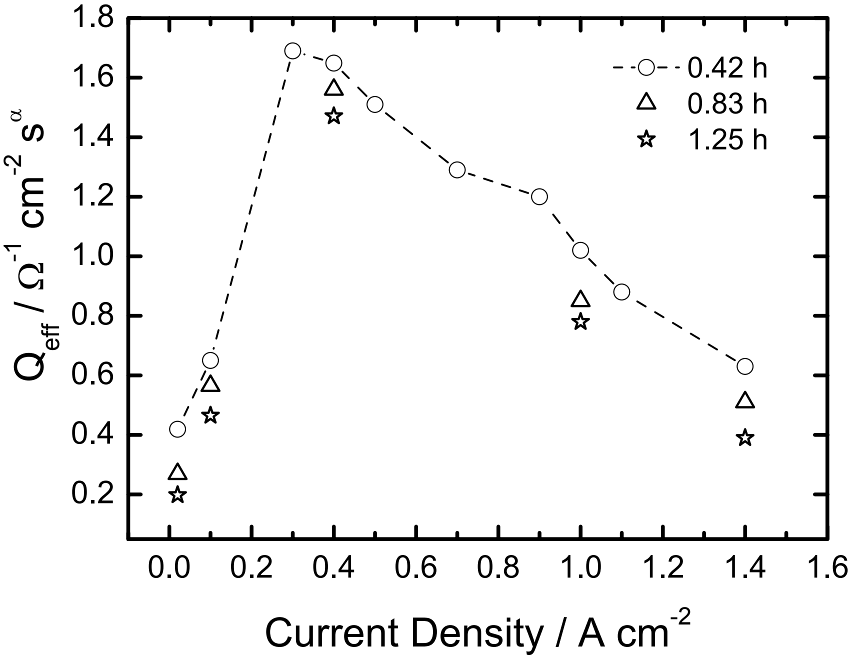

Figure 8-4: CPE coefficient Q_{eff} as a function of current density with time as a parameter. The impedance data were obtained under the conditions described for Figure 8-1.

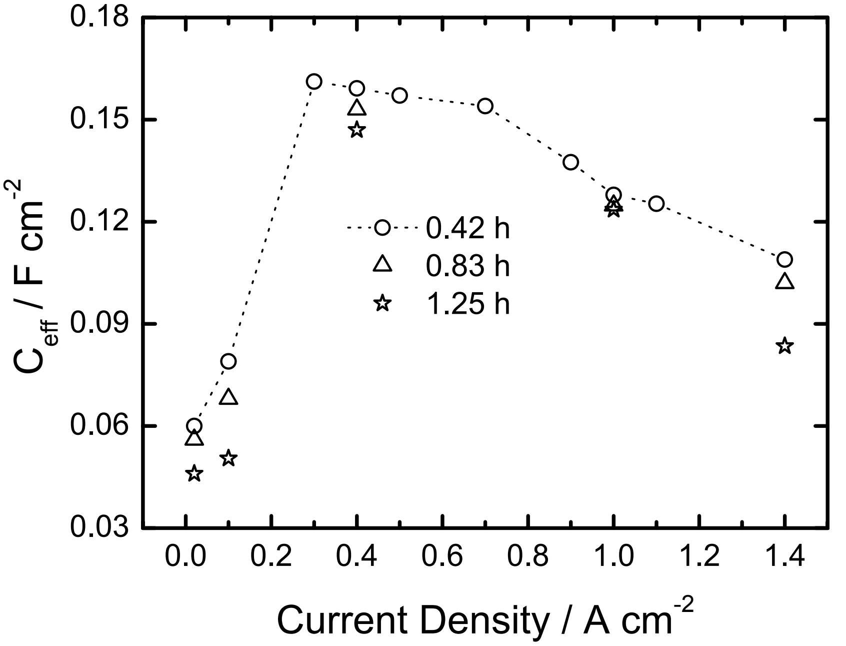

Figure 8-5: The interfacial capacitance C_{eff}, obtained from equation (8–2), as a function of current density with time as a parameter. The impedance data were obtained under the conditions described for Figure 8-1.

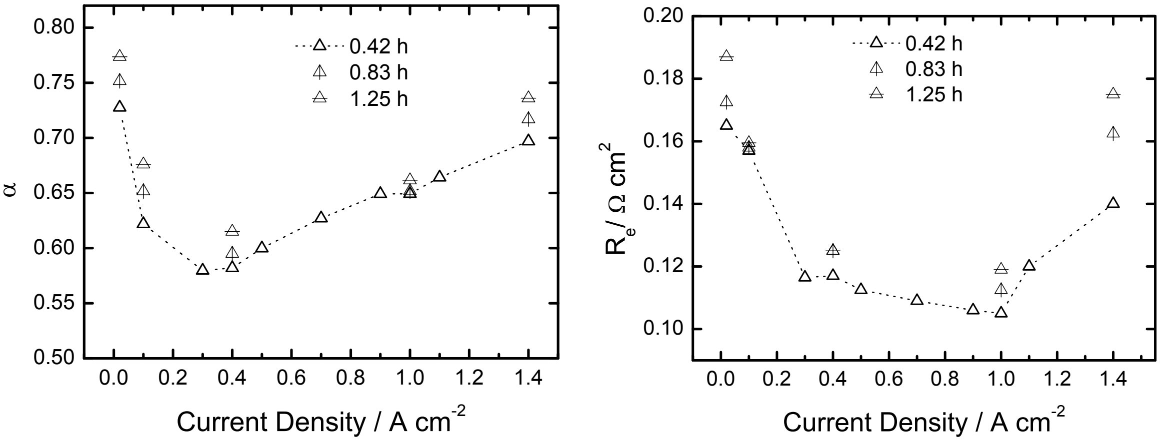

(a) (b)

Figure 8-6: Electrochemical parameters obtained for the data presented in Figures 8-4 and 8-5 as a function of current density with time as a parameter: a) CPE exponent α; and b) Ohmic resistance R_e.

CPE coefficient presented in Figure 8-4. The values of Q_{eff} are 4 to 10 times larger than the values of C_{eff}.

The difference between the values of Q_{eff} and C_{eff} is closely related to the values obtained for the CPE exponent α presented in Figure 8-6(a). At high and low current densities, α approaches values close to 0.8. In these regions, Q_{eff} is about 4 times larger than C_{eff}. At intermediate current densities, α has values near 0.6, and Q_{eff} is about 10 times larger than C_{eff}. The Ohmic resistance, shown in Figure 8-6(b), also plays a role in calculation of capacitance from equation (8–2). A significant increase R_e was observed at drying and flooding conditions. The observed increase in R_e at drying and flooding conditions are consistent with observations reported by Barbir *et al.*[152]

8.2.2 Effect of Operating Parameters

The influence of temperature on the impedance measurements is presented in Figure 8-7 for data obtained at a current density of 0.5 A/cm^2. The impedance was smaller at elevated temperatures, suggesting improved cell performance. The procedure described in the previous section was used to obtain the interfacial capacitance presented in Figure 8-8 as a function of system temperature. An increase in interfacial capacitance was observed

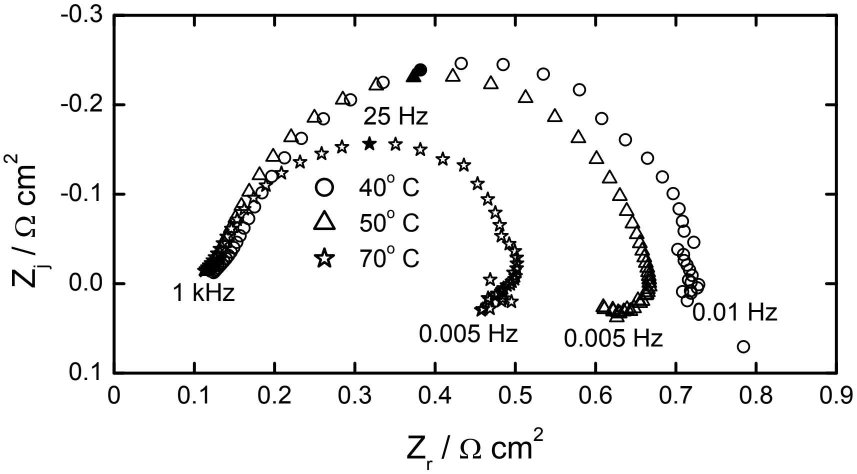

Figure 8-7: Impedance response recorded at a current density of 0.5 A/cm^2 with system temperature as a parameter. The experimental system was the same as described in Figure 8-1.

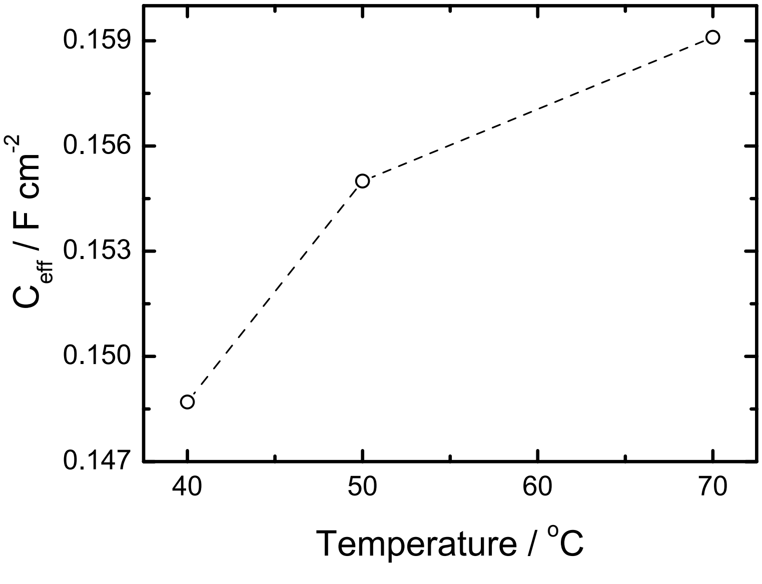

Figure 8-8: The interfacial capacitance C_{eff}, obtained from equation (8–2), as a function of system temperature for the data presented in Figure 8-7.

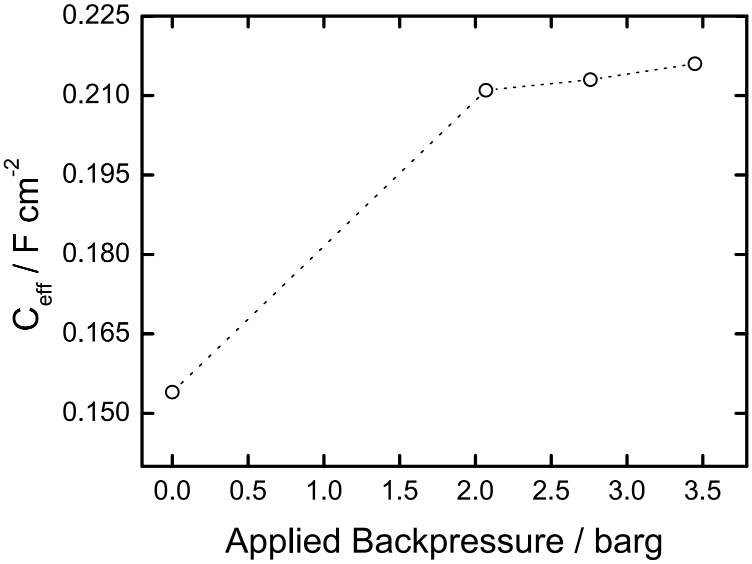

Figure 8-9: The interfacial capacitance C_{eff}, obtained from equation (8–2), as a function of backpressure applied for both the cathode and the anode. The impedance data were recorded at 0.7 A/cm^2 at 70 °C. The experimental system was the same as described in Figure 8-1.

at elevated temperatures, which may account partially for the better performance at higher temperatures.

A similar investigation of the influence of backpressure was performed. The resulting interfacial capacitance, obtained from equation (8–2), is presented in Figure 8-9 as a function of backpressure applied for both the cathode and the anode. The impedance data were recorded at 0.7 A/cm^2 at 70 °C. A significant increase in interfacial capacitance was observed with an increase in the backpressure from 0 to 2 barg. Subsequent increases in backpressure resulted in only small increases in interfacial capacitance.

8.2.3 Effect of Design Parameters

Impedance data recorded with different combinations of flow channels and gas-diffusion layers were also analyzed to estimate the interfacial capacitance as presented in Figure 8-10. The interfacial capacitance for MEAs assembled using a gas diffusion layer with a nonuniform pore distribution was significantly larger than that obtained for MEAs assembled using a gas diffusion layer with a uniform pore distribution. This difference may be attributed to the improved water management properties of the gas diffusion

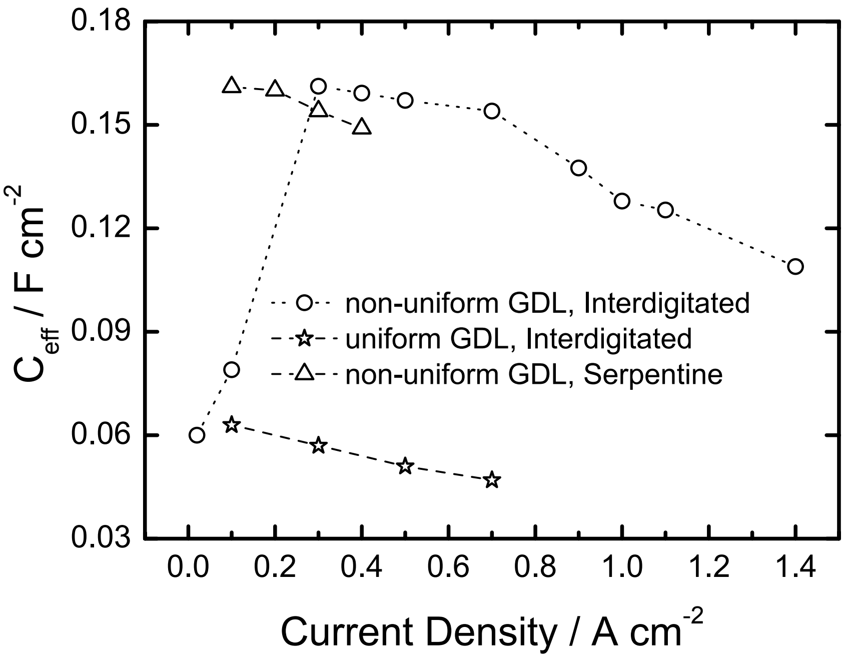

Figure 8-10: Interfacial capacitance as a function of current density for different combinations of flow channels and gas-diffusion layers. The impedance data were recorded at 70 °C.

layer with a nonuniform pore distribution. The influence of flow channel design was much less significant. For MEAs assembled using a gas diffusion layer with a nonuniform pore distribution, the interfacial capacitance was larger for the interdigitated flow channel as compared to the serpentine flow channel. The observation that the value of C_{eff} was found to be larger when using a gas diffusion layer with a nonuniform pore distribution is consistent with the observation that these systems yielded a larger limiting current density.

8.2.4 Transient Behavior

To explore the influence of time, sequential impedance spectra were recorded for a variety of operating conditions. The resulting interfacial capacitance is reported in Figure 8-11 as a function of time with operating and system condition as a parameter.

The interfacial capacitance decreased with time for all impedance data, but the dependence on time was smaller than was observed with current density. The decrease in the interfacial capacitance can be attributed to the slow approach to steady state

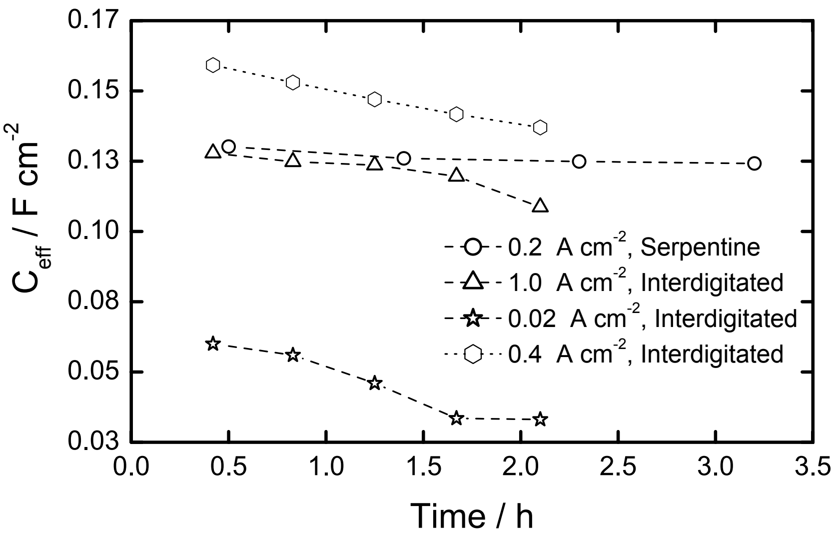

Figure 8-11: Interfacial capacitance as a function of time with operating and system condition as a parameter. The impedance data were recorded at 70 °C using an MEA with a non-uniform GDL.

operation, as reported by Roy and Orazem.[194] The rate of decrease was smallest for current densities least affected by flooding (0.2 A/cm^2 for the serpentine flow channel and 0.4 A/cm^2 for the interdigitated flow channel). The interfacial capacitance was smallest for the system affected by localized drying (0.02 A/cm^2 for the interdigitated flow channel). The interfacial capacitance was somewhat smaller for the system affected by flooding (1.0 A/cm^2 for the interdigitated flow channel).

The corresponding values of CPE exponent α are presented in Figure 8-12. The CPE exponent increased with time for all impedance data and had values that ranged between 0.57 and 0.8. The value of α was largest for the systems most likely to be affected by flooding or drying.

8.3 Discussion

System parameters are typically obtained from impedance data by regression of models. Accordingly, the value of the parameters obtained depend on the suitability of the model and on the quality of the regression. The graphical methods employed in the present work provide information that is limited to the high-frequency portion of the spectrum, where the Faradaic and transport processes do not influence the impedance

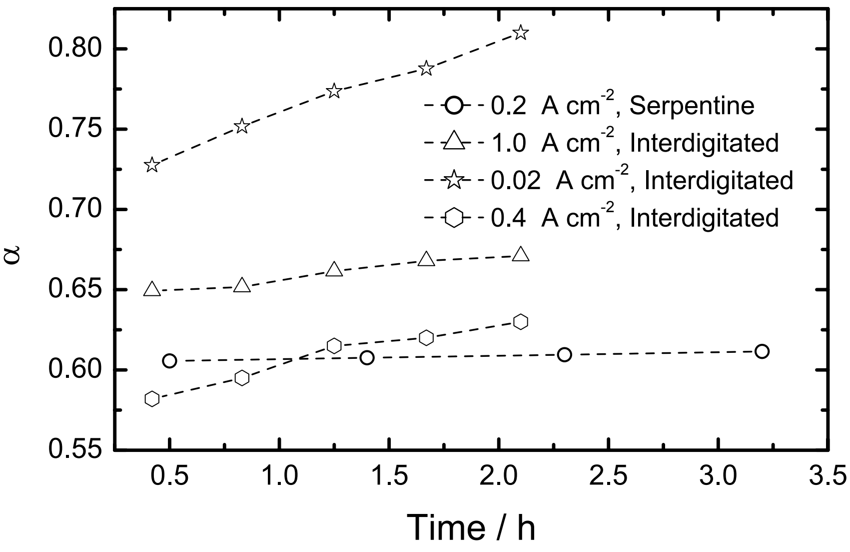

Figure 8-12: CPE exponent α Interfacial-capacitance as a function of time corresponding to the results presented in Figure 8-11.

response. The advantage of the graphical methods employed here is that the parameter values do not depend on the suitability of the model and on the quality of the regression. The values of the CPE parameters Q and α can be obtained unequivocally; however, the relationship between these parameters and the interfacial capacitance requires a model. The formulas developed by Brug *et al.*[227] were found to give good accounting for 2-D distributions.[171] A similar verification has not been provided for 3-D distributions, though the Brug formula has been invoked to describe the relationship between CPE parameters and 3-D distributions in oxides.[228]

The values of α was found in the present work to range between 0.57-0.8, which is consistent with the value of 0.8027 reported by Fouquet *et al.*[157] The value of α can be expected to result from a combined lateral distribution, associated with the distribution of current and potential along the flow channels and between land and channel areas, and an axial distribution associated with the porous character of the MEA. The decreased value of α at low and high current densities may be attributed to increased heterogeneity created by drying or flooding, respectively. Correspondingly, a decrease in the value of C_{eff} was found under conditions associated with drying and flooding. The calculated interfacial capacitance is usually scaled to electrochemical active surface area of catalyst.[229] A decrease in effective surface area of roughly 60 percent was found under drying conditions, and a decrease of roughly was found under flooding conditions.

The higher value estimated for the interfacial capacitance could contribute to the improved performances of the fuel cell at elevated temperature[4] and elevated operating pressure.[196] The sensitivity of interfacial capacitance to poor water management accounts for the small values of capacitance when using a uniform GDL. The capacitance was larger when using a micro-macro porous GDL, which is reported to provide better water management.[64–66] The sharp decrease in C_{eff} at low current densities observed for the non-uniform GDL is likely due to drying of the membrane.[152,12] Similar experiments were not performed for the uniform GDL. The observation of a higher value of the interfacial capacitance for the interdigitated flow channel is consistent with observation of higher current densities and better fuel cell performance as compared to the serpentine flow channel.[4,200,206,207] A moderate decrease in the value of C_{eff} with time was observed. The observed decrease in the interfacial capacitance can be converted into an equivalent decrease in the electrochemical active surface area with time, which could be due to the slow approach to steady-state operation.[194]

CHAPTER 9
CONCLUSIONS

An integral approach comprised of error analysis, model interpretations and validations based on impedance response of the fuel cell was employed to investigate factors influencing performance and lifetime. Use of impedance techniques was also explored to gain an insight into the problem of flooding, drying in the fuel cell. The conclusions are presented in the following sections.

9.1 Error Analysis of Impedance Response

The impedance data for the fuel cell were analyzed using a Voigt measurement model. The inductive loops found at low frequency were found to be consistent with the Kramer-Kronig relation once the fuel cell achieved steady-state operation. The formalism of the measurement model error analysis provides a means for determining whether a steady state has been achieved.

This part of the work confirmed that the low-frequency inductive loops could be attributed to processes occurring in the fuel cell. Kramers-Kronig consistent inductive loops were observed in the entire range (current density) of operation of the fuel cell. The results were independent of the impedance instrumentation used.

9.2 Interpretation of Impedance Response

Low-frequency inductive loops were observed in impedance measurements of the fuel cell. These loops were found to be consistent with the Kramers-Kronig relations and were observed for all parts of the polarization curve. Three analytic impedance models were derived from consideration of specific reaction sequences proposed to take place in the fuel cell. The model that accounted only for hydrogen oxidation and oxygen reduction could not account for the low-frequency inductive loops observed in experimental data. Models that accounted for additional reactions, *i.e.,* formation of hydrogen peroxide and formation of PtO with subsequent dissolution of Pt, could predict low-frequency inductive loops. These models were supported by complementary experiments, and the results show that either of these reaction mechanisms could account for the experimentally observed low-frequency inductive loops. These models can also be used to predict such variables as the fractional surface-coverage of the proposed intermediates.

9.3 Ex-Situ Analysis

The formation of intermediates in the proposed reaction mechanisms were confirmed by experimental investigations including XPS, TEM, SEM, and ICP-MS analysis. The XPS studies indicate that after 600 hours of use, a layer of PtO was formed equivalent to 3 monolayer. The substantial hydrogen crossover through the membrane estimated by the CV experiments supports peroxide formation. Thus, both reaction sequences proposed in Models 2 and 3 are likely in the fuel cell under study, and both the reaction sequences were found to yield low-frequency inductive loops in the impedance response. This work suggests that quantitative analysis of low-frequency inductive loops may provide a useful characterization of reactions which reduce the efficiency and operating life-time of the fuel cell.

9.4 Detecting Onset of Flooding

The flooding of gas diffusion layer pores in the fuel cell has been associated with increases in the internal cell resistance and in the impedance response of the fuel cell. The formation and removal of water droplets is an inherently stochastic process which increases the stochastic errors observed in impedance measurements. A measurement technique oriented towards assessment of the stochastic errors can therefore be used to identify the onset of flooding. In the present work, impedance spectroscopy was coupled with a measurement-model-based error analysis to detect onset of flooding. This method is particularly attractive because it is extremely sensitive and a well-defined baseline stochastic error can be established for the non-flooding condition.

The onset of flooding was examined for a 5 cm^2 PEM fuel cell with an interdigitated flow channel. At low current densities, the ratio of the observed standard deviation to the expected non-flooded standard deviation was close to unity. At larger current densities, the ratio for the real part of the impedance became quite large, with onset of flooding evident at current densities above 1 A/cm^2 for the MEA with a non-uniform GDL and at current densities above 0.3 A/cm^2 for the MEA with a uniform GDL. Drying was evident at current densities below 0.3 A/cm^2 for the MEA with a non-uniform GDL.

The work presented here demonstrates that the stochastic error structure of impedance measurements may be used to detect operating conditions of the fuel cell which induce flooding or drying. In this case, the flooding or drying phenomena contribute stochastic errors which are superposed on those associated with the electronic instrumentation.

9.5 Evaluation of Interfacial Capacitance

Graphical methods were used to interpret impedance spectra in terms of CPE parameters, and the formulas presented by Brug *et al.*[227] were used to convert these into effective interfacial capacitance. The effective interfacial capacitance was smallest at small and large current densities and showed a maximum value at the intermediate current densities. The decreases in interfacial capacitance with higher current density can be attributed to an excess production of water resulting in flooding; whereas, at low current density, the effect could be attributed to drying. The interfacial capacitance was dependent on flow channel configuration, GDL properties, temperature, and backpressure. The improved performance and larger interfacial capacitance observed for the interdigitated flow channel and the non-uniform GDL could be attributed to the improved water management capabilities of these system designs. A smaller influence of time was observed which could be associated with the long time required to achieve steady-state operation.[194]

The use of graphical methods to extract physical properties is under-utilized in the fuel cell literature. The method provides unequivocal values for the CPE exponent α, the CPE coefficient Q, and the Ohmic resistance R_e. The interpretation of the resulting parameters in terms of interfacial capacitance is, however, less clear. More work is needed to confirm the suitability of the Brug formula for combined 2-D/3-D distributions present in the PEM fuel cell.

CHAPTER 10
FUTURE DIRECTIONS

Recommendations for the future research of this work are presented in this chapter. To gain better understanding into the proposed mechanisms, the following research plan can be employed as a future direction of this project.

10.1 Parameter Evaluation

The experimental data can be regressed to the impedance models developed to extract meaningful parameters such as rate constants for reaction kinetics, and transport properties like diffusivity of species. Moreover, other information such as exchange current density, and limiting current density can also be evaluated.

10.2 Effluent, and Microstructure Analysis

More work needed to provide evidence to support or disprove proposed reaction mechanisms. ICP-MS can be applied to estimate platinum concentration[94] in the effluent water of the fuel cell. IC (Ion Chromatography) can be used to estimate fluoride emission rate in the effluent. The Chemtrics Test Kit can be used to measure hydrogen peroxide concentration,[9] and the Orion Test Kit can be used to measure fluoride ion concentration in the effluent water. The information found from the microstructural analysis and the effluent analysis can be used to validate the proposition of the reaction mechanisms for the model development, *e.g.,* the platinum dissolution and the peroxide formation. The fluoride ion concentration in the fuel cell effluent will give the information about lifetime of the membrane.

10.3 One-Dimensional Flow Channel

The pseudo 1-Dimensional flow channel investigated should be analyzed comprehensively to improve the design further. Improved flow channel can be used to compare model and experiment results in the search of kinetics and transport parameters important to describe the fuel cell.

APPENDIX A: COMPUTATIONAL ALGORITHM FOR MODEL 1

```
$r1 = 0.135$; [Electrolyte resistance]
$c = 0.212$; [Double-layer capacitance]
$\alpha_o = 0.5$ [symmetry coefficient for ORR]
$\alpha_h = (1 - \alpha_o)$; [symmetry coefficient for HOR]
$V = 0.68$; [operating voltage]
$F = 96500$; [Faradays constant]
$R = 8.314$; [Universal gas constant]
$T = 298$; [Temperature]
$dh2 = 9 * 10^{-})$; [diffusivity for oxygen]
$do2 = 3.69 * 10^{-}12$; [diffusivity for hydrogen]
$delta = 10^{-}6$; [film thickness]
$ko = 2.63 * 10^{-}2$; [Rate constant for ORR]
$kh = 3.6 * 10^{-}4$; [Rate constant for HOR]
$iexp = []$; [export experimental data]
$eexp = []$; [export experimental data]
$Cmbulkh2$ [define bulk concentration for hydrogen]
$Cmbulko2$ [define bulk concentration for oxygen]
$O = ko * exp(-(\alpha_o FV)/(RT))$; [Kinetic expression for ORR]
$H = kh * exp(-(\alpha_h FV)/(RT))$; [Kinetic expression for HOR]
$ilimh2 = (2. * F. * Dh2. * Cmbulkh2)./(delta)$; [limiting current of hydrogen]
$ilimo2 = (4. * F. * Do2. * Cmbulko2)./(delta)$; [limiting current of oxygen]
$A = 2. * Kh2. * F. * Dh2. * Cmbulkh2. * exp(bh2. * vh2)$; [lumped parameter for HOR]
$B = 4. * Ko2. * F. * Do2. * Cmbulko2. * exp(-bo2. * vo2)$; [lumped parameter for ORR]
$ih2 = (A. * ilimh2)./(A + ilimh2)$; [current from HOR]
$io2 = (B. * ilimo2)./(B + ilimo2)$; [current from ORR]
$plot(io2, V,' *')$; [current from ORR]
```

$iT = io2$; [current at cathode]

$ih2 = iT$; [current at anode]

$na = (log((iT)./(Kh2. * Cmbulkh2). * (1 - (iT./ilimh2))))./bh2$; [equating current at cathode and anode]

$VT = V - (iT. * Reff) + na$; [cathode overpotential]

$plot(iT, VT, ' -')$;

$plot(iexp, eexp, ' o')$;

$Rto = [(2(\alpha_o)F^2(1 - \gamma)O)/(RT)]$; [Charge-transfer resistance for ORR]

$Rth = [(2(\alpha_h)F^2(\gamma)H)/(RT)]$; [Charge-transfer resistance for HOR]

$p0 = (2Fkoexp(-\alpha_o FV/(RT)))$; [Mass-transfer impedance for ORR]

$q0 = (2Fkhexp(-\alpha_h FV/(RT)))$; [Mass-transfer impedance for HOR]

$w = -6 : .05 : 6$; [Frequency range]

$w = 10.^w$;

$p1 = Rto$;

$Kh2 = (w * delta^2)/dh2$; [tangent hyperbolic for Hydrogen]

$th2 = tanh(sqrt(i * Kh2))./(sqrt(i * Kh2))$;

$Ko2 = (w. * delta^2)/do2$;

$to2 = tanh(sqrt(i * Ko2))./(sqrt(i * Ko2))$;

$A1 = 1./(RtO2 + ZDO2 * to2)$;[lumped parameters for HOR]

$C1 = 1./(RtH2 + ZDH2 * th2)$; [lumped parameters for HOR]

$p2 = p0$;

$q1 = Rth$;

$q2 = q0$;

$z1 = (p1 - q1). * (p2 - q2)$;

$z2 = z1./((jwF2) - p2 - q2)$;

$z3 = z2 + (p1 + q1) + (jwc)$;

$z4 = 1./z3$;

```
z = r1 + z4; [overall impedance]

zr = real(z);

zi = imag(z);

plot(exzr, -exzj,' o')

daspect([111])

y = [zr; zi];

fid = fopen('M1EIS90.txt',' w');

fclose(fid);
```

APPENDIX B: COMPUTATIONAL ALGORITHM FOR MODEL 2

$r1 = 0.135;$ [Electrolyte resistance]

$c = 0.212;$ [Double-layer capacitance]

$\alpha_o = 0.5$ [symmetry coefficient for ORR]

$\alpha_h = (1 - \alpha_o);$ [symmetry coefficient for HOR]

$V = 0.68;$ [operating voltage]

$F = 96500;$ [Faraday constant]

$R = 8.314;$ [Universal gas constant]

$T = 298;$ [Temperature]

$dh2 = 9 * 10^{-});$ [diffusivity for oxygen]

$do2 = 3.69 * 10^{-}12;$ [diffusivity for hydrogen]

$dh2o2 = 4e - 15;$ [diffusivity for peroxide]

$delta = 10^{-}6;$ [film thickness]

$ko = 2.63 * 10^{-}2;$ [Rate constant for ORR1]

$kh = 3.6 * 10^{-}4;$ [Rate constant for HOR]

$kh2o2 = 3.6 * 10^{-}4;$ [Rate constant for ORR2]

$iexp = [];$ [export experimental data]

$eexp = [];$ [export experimental data]

$Cmbulkh2$ [define bulk concentration for hydrogen]

$Cmbulko2$ [define bulk concentration for oxygen]

$ko = 2.63 * 10^{-}2;$ [Rate constant for ORR]

$kh = 3.6 * 10^{-}4;$ [Rate constant for HOR]

$O = ko * exp(-(\alpha_o FV)/(RT));$ [Kinetic expression for ORR]

$H = kh * exp(-(\alpha_h FV)/(RT));$ [Kinetic expression for HOR]

$\gamma = [O/(O + H)];$ [Surface coverage of hydrogen peroxide]

$a = (1./ilimh2o2) - (1./ilimo2);$

$b = (1./ilimh2o2) - (1./B) - (1./C) - (1./ilimo2);$

$c = 1./C;$

$theta1 = (b + sqrt(b.^2 + 4. * c. * a))./(2 * a);$

$ih2 = (A. * ilimh2)./(A + ilimh2); figure(2)plot(ih2, V,' +');$

$io2 = (B. * ilimo2. * (1 - theta2))./((B. * (1 - theta2)) + ilimo2);$

$ih2o2 = (C. * ilimh2o2. * theta2)./((C. * theta2) + ilimh2o2);$

$iT = ih2 + io2 + ih2o2;$ [Total current]

$w = -6 : .05 : 6;$ [Frequency range]

$w = 10.^w;$

$Kh2 = (w * delta^2)/dh2; bh2 = tanh(sqrt(i * Kh2))./(sqrt(i * Kh2));$

$Ko2 = (w. * delta^2)/do2; bo2 = tanh(sqrt(i * Ko2))./(sqrt(i * Ko2));$

$Kh2o2 = (w. * delta^2)/dh2o2;$

$b2o2 = tanh(sqrt(i * Kh2o2))./(sqrt(i * Kh2o2));$

$C1 = 1./(RtH2 + ZDH2 * bh2);$

$D1 = 1./(RtO2 + ZDO2 * bo2);$

$D2 = 1./((RtO2 + ZDO2 * bo2). * (1 - gamma));$

$E1 = 1./(RtH2O2 + ZDH2O2 * b2o2);$

$E2 = 1./((RtH2O2 + ZDH2O2 * b2o2). * gamma);$

$H = (D2 - E2). * (D1 - E1)./(2 * 96500 * i * 2 * 3.14 * w - D2 + E2);$

$z = re + (1./((C1 + D1 + E1) + H + (i * 2 * 3.14 * w * c))) + (1./((C1) + (i * 2 * 3.14 * w * c)));$

$zr = real(z);$

$zi = imag(z);$

APPENDIX C: COMPUTATIONAL ALGORITHM FOR MODEL 3

$r1 = 0.135$; [Electrolyte resistance]

$c = 0.212$; [Double-layer capacitance]

$\alpha_o = 0.5$ [symmetry coefficient for ORR]

$\alpha_h = (1 - \alpha_o)$; [symmetry coefficient for HOR]

$V = 0.68$; [operating voltage]

$F = 96500$; [Faradays constant]

$R = 8.314$; [Universal gas constant]

$T = 298$; [Temperature]

$ko = 2.63 * 10^{-}2$; [Rate constant for ORR]

$kh = 3.6 * 10^{-}4$; [Rate constant for HOR]

$O = ko * exp(-(\alpha_o FV)/(RT))$; [Kinetic expression for ORR]

$H = kh * exp(-(\alpha_h FV)/(RT))$; [Kinetic expression for HOR]

$\gamma = [O/(O + H)]$; [Surface coverage of hydrogen peroxide]

$A = 2. * Kh2. * F. * Dh2. * Cmbulkh2. * exp(bh2. * vh2);$

$k1 = 4. * F. * Do2. * Cmbulko2. * exp(-bo2. * vo2);$

$C1 = Kptf. * exp(bpt. * vpt);$

$C2 = -Kptb. * exp(-bpt. * vpt); k2 = C1 - C2 + k3;$

$a = (Kpt. * k1. * (ilimo2 + C1)) + (C1. * ilimo2);$

$b = -((Kpt. * k1. * (ilimo2 + k2)) + ((k2 - (Kpto. * k1)). * ilimo2));$

$c = (k2. * k1). * (Kpt - Kpto);$

$theta1 = (b + sqrt((b.^2) - (4. * c. * a)))./(2 * a);$

$theta2 = C1./(k2); figure(1) plot(V, theta2);$

$ih2 = (A. * ilimh2)./(A + ilimh2);$

$Ke = Kpt + ((Kpto - Kpt). * theta2);$

$B = Ke. * k1; io2 = (B. * ilimo2)./(B + ilimo2);$

$ipt = (C1. * (1 - theta2)) - (C2. * theta2);$

$iT = io2 + ipt;$

$na = (log((iT)./(Kh2. * Cmbulkh2). * (1 - (iT./ilimh2))))./bh2;$

$VT = V - (iT. * Reff) - na;$

$y = [VT; iT; theta2];$

$w = -6 : .05 : 6;$ [Frequency range]

$w = 10.^{w};$

$Ko2 = (w. * delta^2)/do2;$

$bo2 = tanh(sqrt(i * Ko2))./(sqrt(i * Ko2));$

$C1 = 1./(RtH2 + ZDH2 * bh2);$

$A1 = 1./(RtO2 + ZDO2 * bo2);$

$A2 = 1. * g2./(RtO2 + ZDO2 * bo2);$

$B1 = 1. * (1./RtPtf) + (1./RtPtb);$

$B2 = 1. * (f3 + f4);$

$T = ((A2 + B2). * (A1 - B1))./(2 * 96500 * i * 2 * 3.14 * w - B2 + A2 + f5);$

$z = re + (1./((A1 + B1 + C1) + T + (i * 2 * 3.14 * w * c))) + (1./((A1) + (i * 2 * 3.14 * w * c)));$

$zr = real(z);$

$zi = imag(z);$

REFERENCES

[1] G. Hoogers, *Fuel Cell Technology Handbook*, 2nd edition (CRC Press LLC, 2003).

[2] J. Lin, H. R. Kunz, J. M. Fenton, and S. S. Fenton, "The Fuel Cell: An Ideal ChE Undergraduate Experiment," *Chemical Engineering Education*, **Winter** (2004) 38–47.

[3] A. Z. Weber and J. Newman, "Transport in Polymer-Electrolyte Membranes 1. Physical Model," *Journal of the Electrochemical Society*, **150** (2003) A1008–A1015.

[4] L. Wang and H. Liu, "Performance Studies of PEM Fuel Cells with Interdigitated Flow Fields," *Journal of Power Sources*, **134** (2004) 185–196.

[5] F. L. Darkrim, P. Malbrunot, and G. Tartaglia, "Review of Hydrogen Storage by Adsorption in Carbon Nanotubes," *Int. J. Hydrogen Energy*, **27** (2002) 193–202.

[6] V. C. Y. Kong, F. R. Foulkes, D. W. Kirk, and J. T. Hinatsu, "Development of Hydrogen Storage for Fuel Cell Generators I: Hydrogen Generation using Hydrolysis Hydrides," *Int. J. Hydrogen Energ.*, **24** (1999) 665–675.

[7] C. F. Zinola, J. Rodriguez, and G. Obal, "Kinetic of Molecular Oxygen Electroreduction on Platinum Modified by Tin Underpotential Deposition," *J. Appl. Electrochem.*, **31** (2001) 1293–1300.

[8] A. Damjanovic and V. Brusic, "Electrode Kinetic of Oxygen Reduction on Oxide Free Pt Electrode," *Electochimica Acta*, **12** (1967) 615–628.

[9] V. O. Mittal, H. R. Kunz, and J. M. Fenton, "Is H2O2 Involved in the Membrane Degradation Mechanism in PEMFC," *Electrochemical and Solid-State Letters*, **9** (2006) A229–A302.

[10] R. M. Darling and J. P. Meyers, "Kinetic Model of Platinum Dissolution in PEMFCs," *Journal of the Electrochemical Society*, **150** (2003) A1523–A1527.

[11] L. M. Roen, C. H. Paik, and T. D. Jarvi, "Electrocatalytic Corrosion of Carbon Support in PEMFC Cathodes," *Electrochemical and Solid-State Letters*, **7** (2004) A19–A22.

[12] J.-M. L. Canut, R. M. Abouatallah, and D. A. Harrington, "Detection of Membrane Drying, Fuel Cell Flooding, and Anode Catalyst Poisoning on PEMFC Stacks by Electrochemical Impedance Spectroscopy," *Journal of the Electrochemical Society*, **153** (2006) A857–A864.

[13] M. Winter and R. Brodd, "What are Batteries, Fuel Cells, and Supercapacitors," *Chem. Rev.*, **104** (2004) 4245–4270.

[14] L. F. Brown, "A comparative study of fuels for on-Board hydrogen production for fuel cell powered automobiles," *Inst. J. Hydrogen Energy*, **26** (2001) 381.

[15] D. Davies, P. Adcock, M. Turpin, and S. Rowen, "Stainless Steel as Bipolar Plate Material for Solid Polymer Fuel Cells," *Journal of Power Sources*, **86** (2000) 237–242.

[16] H. van Bussel, F. Koene, and R. Mallant, "Dynamic model of solid polymer fuel cell water management," *Journal of Power Sources*, **71** (1998) 218–222.

[17] G. Maggion, V. Recupero, and L. Pino, "Modeling PEM fuel cell: an innovative approach," *Journal of Power Sources*, **101** (2001) 275–286.

[18] R. Roshandel, B. Farhanieha, and E. Saievar-Iranizad, "The Effects of Porosity Distribution Variation on PEM Fuel Cell Performance," *Renewable Energy*, **30** (2005) 1557–1572.

[19] M. Eikerling and A. A. Kornyshev, "Electrochemical Impedance of the Cathode Catalyst Layer in Polymer Electrolyte Fuel Cells," *Journal of Electroanalytical Chemistry*, **475** (1999) 107–123.

[20] K. T. Adjemian, S. J. Lee, S. Srinivasan, J. Benziger, and . A. B. Bocarslya, "Silicon Oxide Nafion Composite Membranes for Proton-Exchange Membrane Fuel Cell Operation at 80-140C," *Journal of the Electrochemical Society*, **149** (2002) A256–A261.

[21] C. Huang, K. Tan, J. Lin, and K. Tan, "XRD and XPS analysis of the degradation of the polymer electrolyte in H2-O2 fuel cell,," *Chem. Phys. Lett*, **371** (2003) 80–85.

[22] F. Liu, B. Yi, D. Xing, J. Yu, Z. Hou, and Y. Fu, "Development of novel self-humidifying composite membranes for fuel cells," *Journal of Power Sources*, **124** (2003) 81–89.

[23] M. Li, Z.-G. Shao, H. Zhang, Y. Zhang, X. Zhu, and B. Yi, "Self-Humidifying Cs2.5H0.5PW12O40/Nafion/PTFE Composite Membrane for Proton Exchange Membrane Fuel Cells," *Electrochemical and Solid-State Letters*, **9** (2006) A92–A95.

[24] M.-K. Song, Y.-T. Kim, J. M. Fenton, H. R. Kunz, and H.-W. Rhee, "Chemically-modified Nafion1/poly(vinylidene fluoride) blend ionomers for proton exchange membrane fuel cells," *Journal of Power Sources*, **117** (2003) 14–21.

[25] C. Heitner-Wirguin, "Recent Advances in Perfluorinated Ionomer Membranes: Structure, Properties and," *J. Membr. Sci.*, **120** (1996) 1–33.

[26] Y.-H. Liu, B. Yi, Z.-G.Shao, D. Xing, and H. Zhanga, "Carbon Nanotubes Reinforced Nafion Composite Membrane for Fuel Cell Applications," *Electrochemical and Solid-State Letters*, **9** (2006) A356–A359.

[27] M. Doyle, S. Choi, and G. Proulx, "High-Temperature Proton Conducting Membranes Based on Perfluorinated Ionomer Membrane-Ionic Liquid Composites," *Journal of the Electrochemical Society*, **147** (2000) 34–37.

[28] J.-D. Kim, T. Mori, and I. Honma, "Organic-Inorganic Hybrid Membranes for a PEMFC Operation at Intermediate Temperatures," *Journal of the Electrochemical Society*, **153** (2006) A508–A514.

[29] M. Nagao, A. Takeuchi, . Heo, and T. Hibino, "A Proton-Conducting In3+-Doped SnP2O7 Electrolyte for Intermediate-Temperature Fuel Cells," *Electrochemical and Solid-State Letters*, **9** (2006) A105–A109.

[30] V. Ramani, H. R. Kunz, and J. M. Fenton, "Stabilized Composite Membranes and Membrane Electrode Assemblies for Elevated Temperature/Low Relative Humidity PEFC Operation," *Journal of Power Sources*, **152** (2005) 182–188.

[31] V. Ramani, H. R. Kunz, and J. M. Fenton, "Investigation of Nafion/HPA Composite Membranes for High Temperature/Low Relative Humidity PEMFC Operation," *Journal of Membrane Science*, **232** (2004) 31–44.

[32] V. Ramani, H. R. Kunz, and J. M. Fenton, "Stabilized Heteropolyacid/Nafion Composite Membranes for Elevated Temperature/Low Relative Humidity PEFC Operation," *Electrochimica Acta*, **50** (2005) 1181–1187.

[33] V. Ramani, H. Kunz, and J. Fenton, "Effect of Particle Size Reduction on the Conductivity of Nafion/Phosphotungstic Acid Composite Membranes," *Journal of Membrane Science*, **266** (2005) 110–114.

[34] D. A. Boysen, C. R. I. Chisholm, S. M. Haile, and S. R. Narayanan, "Polymer Solid Acid Composite Membranes for Fuel-Cell Applications," *Journal of the Electrochemical Society*, **147** (2000) 3610–3613.

[35] R. Jiang, H. R. Kunz, and J. M. Fenton, "Composite Silica/Nafion Membranes Prepared by Tetraethylorthosilicate Sol-Gel Reaction and Solution Casting for Direct Methanol Fuel Cells," *Journal of Membrane Science*, **272** (2006) 116–124.

[36] M. A. Sweikart, A. M. Herring, J. A. Turner, D. L. Williamson, B. D. McCloskey, S. R. Boonrueng, and M. Sanchez, "12-Tungstophosphoric Acid Composites with Sulfonated or Unsulfonated Epoxies for High-Temperature PEMFCs," *Journal of the Electrochemical Society*, **151** (2005) A98–A103.

[37] A. P. Saab, F. H. Garzon, and T. A. Zawodzinski, "Determination of Ionic and Electronic Resistivities in Carbon/Polyelectrolyte Fuel-Cell Composite Electrodes," *Journal of the Electrochemical Society*, **149** (2002) A1541–A1546.

[38] A. Rusanov, "Novel Bis(Naphthalic Anhydrides) and Their Polyheteroarylenes with Improved," *Adv. Polym. Sci.*, **111** (1994) 115–175.

[39] C. Feger, J. McGrath, and M. Khojasteh, *Polyimides: Materials, Chemistry and Characterization* (Elsevier: New York, 1988).

[40] X. Wang and I.-M. Hsing, "Surfactant Stabilized Pt and Pt Alloy Electrocatalyst for Polymer Electrolyte Fuel Cells," *Electochimica Acta*, **47** (2002) 2981–2987.

[41] Y. Song, Y. Wei, H. Xu, M. Williams, Y. Liu, L. J. Bonville, H. R. Kunz, and J. M. Fentona, "Improvement in high temperature proton exchange membrane fuel cells cathode performance with ammonium carbonate," *Journal of Power Sources*, **141** (2005) 250–257.

[42] T. Ioroi and K. Yasuda, "Platinum-Iridium Alloys as Oxygen Reduction Electrocatalyss for Polymer Electrolyte Fuel Cells," *Journal of the Electrochemical Society*, **152** (2005) A1917–A1924.

[43] J. R. C. Salgado, E. Antolini, and E. R. Gonzalez, "Pt-CoC Electrocatalys for Oxygen Reduction in H2/O2 [PEMFCs," *Journal of the Electrochemical Society*, (2004) A2143–A2149.

[44] P. J. Bouwman, W. Dmowski, J. Stanley, G. B. Cotton, and K. E. Swider-Lyons, "Platiunm-Iron Phosphate Electrocatalysts for Oxygen Reduction in PEMFCs," *Journal of the Electrochemical Society*, **151** (2004) A1989–A1998.

[45] H. R. Colon-Mercado, H. Kim, and B. N. Popov, "Durability Study of Pt3Ni Catalyst as Cathode in PEM Fuel Cells," *Electrochemistry Communications*, **6** (2004) 795–799.

[46] H. R. Colon-Mercado and B. N. Popov, "Stability of Pt Based Alloy Cathode Catalysts in PEM Fuel Cells," *Journal of Power Sources*, **155** (2006) 253–263.

[47] T. Toda, H. Igarashi, H. Uchida, and M. Watanabe, "Enhancement of the electroreduction of oxygen on Pt alloys witn Fe Ni Co," *Journal of the Electrochemical Society*, **146** (1999) 3750–3756.

[48] Y. Liu, A. Ishihara, S. Mitsushima, N. Kamiya, and K. Ota, "Zirconia Oxide for PEFC Cathode," *Electrochemical Solid-State Letters*, **8** (2005) A400–A402.

[49] A. Ishihara, K. Lee, S. Doi, S. Mitsushima, N. M. Hara, K. Domen, K. Fukuda, and K. Ota, "Tantalum Oxynitride for Novel Cathode for PEFC," *Electrochemical Solid-State Letters*, **8** (2005) A201–A203.

[50] A. H. C. Sirk, S. A. Campbell, and V. I. Birss, "Oxygen Reduction by Sol Derived [Co, N, C,O]-Based Catalysts for use in Proton Exchange Membrane Fuel Cells," *Electrochemical Solid-State Letters*, **8** (2005) A104–A107.

[51] K. Lee, A. Ishihara, S. Mitsushima, N. Kamiya, and K. Ota, "Stability and Electrocatalytic Activity for Oxygen Reduction in WC + Ta Catalyst," *Electochimica Acta*, **49** (2004) 3479–3485.

[52] G. Girishkumar, M. Rettker, R. Underhile, D. Binz, K. Vinodgopal, P. McGinn, and P. Kamat, "Single-Wall Carbon Nanotube-Based Proton Exchange Membrane Assembly for Hydrogen Fuel Cells," *Langmuir*, **21** (2005) 8487–8494.

[53] K. Kinoshita, *Carbon: Electrochemical and Physicochemical Properties* (Wiley: New York, 1988).

[54] A. Smirnova, X. Dong, H. Hara, and N. Sammes, “Aerogel-based PEMFC Catalyst Operating at Room Temperature,” *Journal of Fuel Cell Science and Technology*, **3** (2006) 477–481.

[55] W. Li, X. Wang, Z. Chen, M. Waje, and Y. Yan, “Carbon Nanotube Film by Filtration as Cathode Catalyst Support for Proton-Exchange Membrane Fuel Cell,” *Langmuir*, **21** (2005) 9386 – 9389.

[56] Y. Shao, G. Yin, Y. Gao, and P. Shi, “Durability Study of Pt/C and Pt/CNTs Catalysts under Simulated PEM Fuel Cell Conditions,” *Journal of the Electrochemical Society*, **153** (2006) A1093–A1097.

[57] R. Zeis, A. Mathur, G. Fritz, J. Lee, and J. Erlebacher, “Platinum-plated Nanoporous Gold: An Efficient, Low Pt Loading Electrocatalyst for PEM Fuel Cells,” *Journal of Power Sources*, **165** (2007) 65–72.

[58] M. C. Lefebvre, Z. Qi, and P. G. Pickup, “Electronically Conducting Proton Exchange Polymers as Catalyst Supports for Proton Exchange Membrane Fuel Cells Electrocatalysis of Oxygen Reduction, Hydrogen Oxidation, and Methanol Oxidation,” *Journal of the Electrochemical Society*, **146** (1999) 2054–2058.

[59] H. . Chhina, S. Campbell, and O. Kesler, “Ex-Situ Evaluation of Tungsten Oxide as a Catalyst Support for PEMFC,” *Journal of the Electrochemical Society*, **154** (2007) B533–B539.

[60] S. J. Lee, S. Mukerjee, J. McBreen, Y. W. Rho, Y. T. Kho, and T. H. Lee, “Effects of Nafion Impregnation on Performances of PEMFC Electrode,” *Electochimica Acta*, **43** (1998) 3693–3701.

[61] J. M. Song, S. Y. Cha, and W. M. Lee, “Optimal Composition of Polymer Electrolyte Fuel Cell Electrodes Determined by AC Impedance Method,” *Journal of Power Sources*, **94** (2001) 78–84.

[62] G. Li and P. G. Pickup, “Ionic Conductivity of PEMFC Electrodes Effect of Nafion Loading,” *Journal of the Electrochemical Society*, **150** (2003) C745–C752.

[63] C. S. Kong, D. Y. Kim, H. K. Lee, Y. G. Shul, and T. H. Lee, “Influence of Pore-Size Distribution of Diffusion Layer on Mass-Transport Problmes of Proton Exchange Membrane Fuel Cells,” *Journal of Power Sources*, **108** (2002) 185–191.

[64] T. E. Springer, T. A. Zawodzinski, M. S. Wilson, and S. Gottesfeld, “Characterization of Polymer Electrolyte Fuel Cells using AC Impedance Spectroscopy,” *Journal of the Electrochemical Society*, **143** (1996) 587–599.

[65] V. A. Paganin, C. L. F. Oliveira, E. A. Ticianelli, T. E. Springer, and E. R. Gonzalez, “Modelistic Interpretations of Impedance Response of Polymer Electrolyte Fuel Cell,” *Electochimica Acta*, **43** (1998) 3761–3766.

[66] W. K. Lee, C.-H. Ho, J. W. V. Zee, and M. Murthy, "The effect of compression and gas diffusion layers on the performance of a PEM fuel cell," *Journal of Power Sources*, **84** (1999) 45–51.

[67] S. Shimplee, U. Beuscher, and J. W. V. Zee, "Analysis of GDL Flooding on PEMFC performance," *Electochimica Acta*, **52** (2007) 6748–6754.

[68] T. Hottinen, M. M. aand T. Mennoal, and P. Lund, "Titanium Sinter as gas diffusion backing in PEMFC," *Electochimica Acta*, **118** (2003) 183–188.

[69] A. Pozio, R. Silva, M. D. Francesco, and L. Giorgi, "Nafion Degradation in PEFCs from End Plate Iron Contamination," *Electrochemica Acta*, **48** (2003) 1543.

[70] H. Wang and J. A. Turner, "Ferrite Stainless Steel as Bipolar Plate Material for Polymer Electrolyte Membrane Fuel Cells," *J. Power Sources*, **128** (2004) 193–200.

[71] E. Middleman, W. Kout, B. Vogelaar, J. Lenssen, and E. de Waal, "Bipolar Plates for PEM Fuel Cells," *J. Power Sources*, **118** (2003) 44–46.

[72] M. Oh, Y.S.Yoon, and S.G.Park, "The Electrical and Physical Properties of Alternative Material for Bipolar Plate for PEM Fuel Cell System," *Electochimica Acta*, **50** (2004) 777–780.

[73] D. L. WoodIII, J. S. Yi, and T. V. Nguyen, "Effect of Direct Liquid Water Injection and Interdigitated Flow Field on The Performance of Proton Exchange Membrane Fuel Cells," *Electochimica Acta*, **43** (1998) 3795–3809.

[74] J. S. Yi and T. V. Nguyen, "Multicomponent Transport in Porous Electrodes of Proton Exchange Membrane Fuel Cells Using the Interdigitated Gas Distributors," *Journal of the Electrochemical Society*, **146** (1999) 38–45.

[75] S. J. C. Cleghorn, D. K. Mayfield, D. A. Moore, J. C. Moore, G. Rusch, T. W. Sherman, N. T. Sisofo, and U. Beuscher, "A Polymer Electrolyte Fuel Cell Life Test: 3 Years of Continuous Operation," *Journal of Power Sources*, **158** (2006) 446–454.

[76] O. Antoine and R. Durand, "RRDE Study of Oxygen Reduction on Pt Nanoparticles Inside Nafion: H202 Production in PEMFC Cathode Conditions," *Journal of Applied Electrochemistry*, **30** (2000) 839–844.

[77] M. Inaba, H. Yamada, J. Tokunaga, and A. Tasaka, "Effect of Agglomeration of Pt/C Catalyst on Hydrogen Peroxide Formation," *Electrochemical and Solid-State Letters*, **7** (2004) A474–476.

[78] W. Liu and D. Zuckerbrod, "In Situ Detection of Hydrogen Peroxide in PEM Fuel Cells," *Journal of the Electrochemical Society*, **152** (2006) A1165–A1170.

[79] J. Jiang and A. Kucernak, "Investigations of fuel cell reactions at the composite microelectrode solid polymer electrolyte interface I. hydrogen oxidation at the nanostructure Pt-Nafion membrane interface," *Journal of Electroanalytic Chemistry*, **567** (2004) 123–137.

[80] V. Stemeankovic, B.N.Gurgur, P.N.Ross, and M.N.Markovic, "Oxygen Reduction Reaction on Pt and Pt-Bimetallic Electrodes Covered with CO, mechanism of air bleed effect of reformate," *Journal of the Electrochemical Society*, **152** (2005) A277–A282.

[81] V. A. Sethuraman, J. W. Weidner, A. T. Haug, S.Motupally, and L. V. Protsailo, "Hydrogen Peroxide Formation Rates in a PEMFC Anode and Cathode Effect of Humidity and Temperature," *Journal of the Electrochemical Society*, **155** (2008) B50–B57.

[82] A. Ohma, S. Suga, S. Yamamoto, and K.Shinohara, "Membrane Degradation Behavior during Open-Circuit Voltage Hold Test," (2007).

[83] A. B. Laconti, M. Mamdan, and R. C. MacDonald, *Handbook of Fuel Cells*, volume 3, 2nd edition (New York: John Wiley and Sons, 2003).

[84] E. Endoh, S. Terazono, B.Widjaja, and Y. Takimoto, "Degradation Study of MEA for PEMFCs under Low Humidity Conditions," *Electrochemical and Solid-State Letters*, **7** (2004) A209–A211.

[85] M. Inaba, "Degradation Mechanism of Polymer Electrolyte Fuel Cells," in *14th International Conference on Properties of Water and Steam in Kyoto.* (2004) 395–402.

[86] X. Huang, R. Solasi, Y. Zou, M. Feshler, K. Reifsnider, D. Condit, S. Burlastsky, and T. Madden, "Mechanical Endurance of Polymer Electrolyte Membrane and PEM Fuel Cell Durability," *Journal of Polymer Science: Part B: Polymer Physics*, **44** (2006) 2346–2357.

[87] J. Qiao, M. Saito, K. Hayamizu, and T. Okada, "Degradation of Perfluorinated Ionomer Membranes for PEMFuel Cells during Processing with H2O2," *Journal of the Electrochemical Society*, **153** (2006) A967–A974.

[88] T. Patterson, "Fuel Cell Technology Topical Conference Proceedings," in *Fuel Cell Technology Topical Conference Proceedings*, AIChE Spring National Meeting (2002) 235.

[89] M. Cai, M. S. Ruthkosky, B. Merzougui, S. Swathirajan, M. P. Balogh, and S. H. Oha, "Investigation of thermal and electrochemical degradation of fuel cell catalysts," *Journal of Power Sources*, **160** (2006) 977–986.

[90] H. Xu, R. Kunz, and J. M. Fenton, "Investigation of Platinum Oxidation in PEM Fuel Cells at Various Relative Humidities," *Electrochemical and Solid-State Letters*, **10** (2007) B1–B5.

[91] V. A. T. Dam and F. A. deBruijn, "The Stability of PEMFC Electrodes," *Journal of the Electrochemical Society*, **154** (2007) B494–B499.

[92] K. Ota, Y. Koizumi, S. Mitsushima, and N. Kamiya, "Dissolution of Platinum in Acidic Medium," *ECS Transaction*, **3** (2006) 619–624.

[93] W. Bi, G. E. Gray, and T. F. Fuller, "PEM Fuel Cell Pt/C Dissolution and Deposition in Nafion Electrolyte," *Electrochemical and Solid-State Letters*, **10** (2007) B101–B104.

[94] P. J. Ferreira, G. J. la O', Y. Shao-Horn, D. Morgan, R. Makharia, S. Kocha, and H. A. Gasteiger, "Instability of Pt/C Electrocatalysts in Proton Exchange Membrane Fuel Cells A Mechanistic Investigation," *Journal of the Electrochemical Society*, **152** (2005) A2256–A2271.

[95] R. M. Darling and J. P. Meyers, "Mathematical Model of Platinum Movement in PEM Fuel Cells," *Journal of the Electrochemical Society*, **152** (2005) A242–A247.

[96] K. Yasuda, A. Taniguchi, T. Akita, T. Ioroi, and Z. Siroma, "Characteristics of a Platinum Black Catalyst Layer with Regard to Platinum Dissolution Phenomena in a Membrane Electrode Assembly," *Journal of the Electrochemical Society*, **158** (2006) A1599–A1603.

[97] X. Wang, R. Kumar, and D. J. Myers, "Effect of Voltage on Platinum Dissolution Relevance to Polymer Electrolyte Fuel Cells," *Electrochemical and Solid-State Letters*, **9** (2006) A225–A227.

[98] E. Guilminot, A. Corcella, F. Charlot, F. Maillard, and M. Chateneta, "Detection of Ptz+ Ions and Pt Nanoparticles Inside theMembrane of a Used PEMFC," *Journal of the Electrochemical Society*, **154** (2007) B96–B105.

[99] A. V. Virkar and Y. Zhou, "Mechanism of Catalyst Degradation in Proton Exchange Membrane Fuel Cells," *Journal of the Electrochemical Society*, **154** (2007) B540–B547.

[100] J. Xie, D. L. W. III, K. L. More, P. Atanassov, and R. L. Borup, "Microstructural Changes of Membrane Electrode Assemblies during PEFC Durability Testing at High Humidity Conditions," *Journal of the Electrochemical Society*, **152** (2005) A1011–A1020.

[101] J. Xie, D. L. WoodIII, D. M. Wayne, T. A. Zawodzinski, P. Atanassov, and R. L. Borup, "Durability of PEMFC at High Humidity Conditions," *Journal of the Electrochemical Society*, **152** (2005) A104–A113.

[102] K. H. Kangasniemi, D. A. Condit, and T. D. Jarvi, "Characterization of Vulcan Electrochemically Oxidized under Simulated PEM Fuel Cell Conditions," *Journal of the Electrochemical Society*, **151** (2004) E125–E132.

[103] V. A. Sethuraman, J. W. Weidner, and L. V. Protsailob, “Effect of Diphenyl Siloxane on the Catalytic Activity of Pt on Carbon,” *Electrochemical and Solid-State Letters*, **10** (2007) B207–B209.

[104] R. Mohtadi, W. K. Lee, and J. W. V. Zee, “Assessing Durability of Cathode Exposed to Common Air Impurities,” *Journal of Power Sources*, **138** (2004) 216–225.

[105] E. Barsoukov and J. R. Macdonald, *Impedance Spectroscopy : Theory, Experiment, and Applications*, 2nd edition (Wiley Interscience, 2005).

[106] M. Ciureanu and H. Wang, “Electrochemical Impedance Study of Electrode-Membrane Assemblies in PEM Fuel Cells: I. Electro-oxidation of H2 and H2/CO Mixtures on Pt-Based Gas-Diffusion Electrodes,” *Journal of the Electrochemical Society*, **146** (1999) 4031–4040.

[107] M. Ciureanu, S. D. Mikhailenko, and S. Kaliaguine, “PEM Fuel Cells as Membrane Reactors: Kinetic Analysis by Impedance Spectroscopy,” *Catalyst Today*, **82** (2003) 195–206.

[108] N. Wagner, W. Schnurnberger, B. Muller, and M. Lang, “Electrochemical Impedance Spectra of Solid Oxide Fuel Cells and Polymer Membrane Fuel Cells,” *Electochimica Acta*, **43** (1998) 3785–3793.

[109] J. Fleig, P. Pham, P. Sztulzaft, and J. Maier, “Inhomogeneous Current Distributions at Grain Boundaries and Electrodes and Their Impact on the Impedance,” *Solid State Ionics*, **113-115** (1998) 739–747.

[110] K. Sasaki, Y. Hori, R. Kikuchi, K. Eguchi, A. Ueno, H. Takeuchi, M. Aizawa, K. Tsujimoto, H. Tajiri, H. Nishikawa, and Y. Uchida, “Current-Voltage Characteristics and Impedance Analysis of Solid Oxide Fuel Cells for Mixed H2 and CO Gases,” *Journal of the Electrochemical Society*, **149** (2002) A227–A233.

[111] A. Barbucci, R. Bozzo, G. Cerisola, and P. Costamagn, “Characterisation of Composite SOFC Cathodes using Electrochemical Impedance Spectroscopy. Analysis of Pt/YSZ and LSM/YSZ Electrodes,” *Electochimica Acta*, **47** (2002) 2183–2188.

[112] M. J. Jurgensen, S. Primdahl, and M. Mogensen, “Characterisation of Composite SOFC Cathodes Using Electrochemical Impedance Spectroscopy,” *Electochimica Acta*, **44** (1999) 4195–4201.

[113] S. McIntosh, S. B. Adler, J. M. Vohs, and R. J. Gorte, “Effect of Polarization on and Implications for Characterization of LSM-YSZ Composite Cathodes,” *Electrochemical and Solid-State Letters*, **7** (2004) A111–A114.

[114] J. T. Mueller and P. M. Urban, “Characterization of Direct Methanol Fuel Cells by AC Impedance Spectroscopy,” *Journal of Power Sources*, **75** (1998) 139–143.

[115] G. Li and P. G. Pickup, "Measurement of Single Electrode Potentials and Impedances in Hydrogen and Direct Methanol PEM Fuel Cells," *Electochimica Acta*, **49** (2004) 4119–4126.

[116] W. Merida, D. A. Harrington, J.-M. L. Canut, and G. McLean, "Characterization of Proton Exchange Membrane Fuel Cell (PEMFC) Failures via Electrochemical Impedance Spectroscopy," *Journal of Power Sources*, **161** (2006) 264–274.

[117] S. W. Cha, S. J. Lee, Y. I. Park, and F. B. Prinz, "Investigation of Transport Phenomena in Micro Flow Channels for Miniature Fuel Cells," in *Proc. of 1st Int. Conference on Fuel Cell Science Engineering and Technology*, American Society of Mechanical Engineers, Rochester, NY (2003) 143–148.

[118] E. Cho, J. Ko, H. Y. Ha, S. Hong, K. Lee, T. Lim, and I. Oh, "Characteristics of the PEMFC Repetitively Brought to Temperatures below 0C," *Journal of the Electrochemical Society*, **150** (2003) A1667–A1670.

[119] R. Jiang, H. R. Kunz, and J. M. Fenton, "Electrochemical Oxidation of H2 and H2/CO Mixtures in Higher Temperature (Tcell ¿100C) Proton Exchange Membrane Fuel Cells: Electrochemical Impedance Spectroscopy," *Journal of the Electrochemical Society*, **152** (2005) A1329–A1340.

[120] J. Kim, Y. Park, K. Kobayashi, M. Nagai, and M. Kunimatsu, "Characterization of CO Tolerance of PEMFC by AC Impedance Spectroscopy," *Solid State Ionics*, **140** (2001) 313–325.

[121] M. Yang and C. Hsueh, "Impedance Analysis of Working PEMFCs in the Presence of Carbon Monoxide," *Journal of the Electrochemical Society*, **153** (2006) A1043–A1048.

[122] X. Wang and I. Hsing, "Kinetics Investigation of H2/CO Electro-Oxidation on Carbon Supported Pt and its Alloys using Impedance Based Models," *Journal of Electroanalytical Chemistry*, **556** (2003) 117–126.

[123] M. Mazurek, N. Benker, C. Roth, T. Buhrmester, and H. Fuess, "Electrochemical Impedance and X-Ray Absorption Spectroscopy (EXAFS) as In-Situ Methods to Study the PEMFC Anode," *Fuel Cells 06*, **1** (2006) 16–20.

[124] P. Agarwal, M. E. Orazem, and L. H. García-Rubio, "Measurement Models for Electrochemical Impedance Spectroscopy: I. Demonstration of Applicability," *Journal of the Electrochemical Society*, **139** (1992) 1917–1927.

[125] P. Agarwal, O. D. Crisalle, M. E. Orazem, and L. H. García-Rubio, "Measurement Models for Electrochemical Impedance Spectroscopy: 2. Determination of the Stochastic Contribution to the Error Structure," *Journal of the Electrochemical Society*, **142** (1995) 4149–4158.

[126] P. Agarwal, M. E. Orazem, and L. H. García-Rubio, "Measurement Models for Electrochemical Impedance Spectroscopy: 3. Evaluation of Consistency with the

Kramers-Kronig Relations," *Journal of the Electrochemical Society*, **142** (1995) 4159–4168.

[127] M. E. Orazem, "A Systematic Approach toward Error Structure Identification for Impedance Spectroscopy," *Journal of Electroanalytical Chemistry*, **572** (2004) 317–327.

[128] R. de L. Kronig, "On the Theory of Dispersion of X-Rays," *Journal of the Optical Society of America and Review of Scientific Instruments*, **12** (1926) 547–557.

[129] R. de L. Kronig, "Dispersionstheorie im Röntgengebeit," *Physik Zeitschrift*, **30** (1929) 521–522.

[130] H. A. Kramers, "Die Dispersion und Absorption von Röntgenstrahlen," *Physik Zeitschrift*, **30** (1929) 522–523.

[131] P. Agarwal, M. E. Orazem, and L. H. García-Rubio, "Application of the Kramers Kronig Relations to Electrochemical Impedance Spectroscopy," in *Electrochemical Impedance: Analysis and Interpretation*, J. Scully, D. Silverman, and M. Kendig, editors, volume ASTM STP 1188 (Philadelphia, PA: American Society for Testing and Materials, 1993) 115–139.

[132] B. A. Boukamp and J. R. Macdonald, "Alternatives to Kronig-Kramers Transformation and Testing, and Estimation of Distribtuions," *Solid State Ionics*, **74** (1994) 85–101.

[133] B. A. Boukamp, "A Linear Kronig-Kramers Transform Test for Immittance Data Validation," *Journal of the Electrochemical Society*, **142** (1995) 1885–1894.

[134] P. K. Shukla, M. E. Orazem, and O. D. Crisalle, "Validation of the Measurement Model Concept for Error Structure Identification," *Electrochimica Acta*, **49** (2004) 2881–2889.

[135] M. E. Orazem, P. Agarwal, C. Deslouis, and B. Tribollet, "Application of Measurement Models to Electro-Hydrodynamic Impedance Spectroscopy," *Journal of the Electrochemical Society*, **143** (1996) 948–960.

[136] M. E. Orazem, M. Durbha, C. Deslouis, H. Takenouti, and B. Tribollet, "Influence of Surface Phenomena on the Impedance Response of a Rotating Disk Electrode," *Electrochimica Acta*, **44** (1999) 4403–4412.

[137] I. Frateur, C. Deslouis, M. E. Orazem, and B. Tribollet, "Modeling of the Cast Iron/Drinking Water System by Electrochemical Impedance Spectroscopy," *Electrochimica Acta*, **44** (1999) 4345–4356.

[138] C. Deslouis, T. E. Moustafid, M. M. Musiani, M. E. Orazem, V. Provost, and B. Tribollet, "Effect of Cations on The Diffusivity of The Charge Carriers in Polyaniline Membranes," *Electrochimica Acta*, **44** (1999) 2087–2093.

[139] P. M. Gomadam and J. W. Weidner, "Analysis of Electrochemical Impedance Spectroscopy in Proton Exchange Membrane Fuel Cells," *International Journal of Energy Research*, **29** (2005) 1133–1151.

[140] T. E. Springer and I. D. Raistrick, "Electrical Impedance of Pore Wall for the Flooded - Agglomerate Model of Porous Gas Diffusion Electrodes," *Journal of the Electrochemical Society*, **136** (1989) 1594–1603.

[141] F. Jaouen and G. Lindberg, "Transient Techniques for Investigating Mass Transport Limitations in Gas Diffusion Electrodes 1. Modeling of the PEFC Cathode," *Journal of the Electrochemical Society*, **150** (2003) A1699–A1710.

[142] Q. Guo, M. Gayetano, Y. Tsou, E. S. D. Castro, and R. E. White, "Study of Ionic Conductivity Profiles of The Air Cathode of A PEMFC by AC Impedance Spectroscopy," *Journal of the Electrochemical Society*, **151** (2003) A1440–A1449.

[143] H. F. Oetjen, V. M. Schmidt, U. Stimming, and F. Trila, "Performance Data of a Proton Exchange Membrane Fuel Cell Using H2/CO as Fuel Gas," *Journal of the Electrochemical Society*, **143** (1996) 3838–3842.

[144] O. Antoine, Y. Bultel, and R. Durand, "Oxygen Reduction Reaction Kinetics and Mechanism on Platinum Nanoparticles Inside Nafion," *Journal of Electroanalytical Chemistry*, **499** (2001) 85–94.

[145] K. Wiezell, P. Gode, and G. Lindbergh, "Steady State and EIS Investigations of Hydrogen Electrodes and Membranes in Polymer Electrolyte Fuel Cells - I. Modeling," *Journal of the Electrochemical Society*, **153** (2006) A749–A758.

[146] X. Cheng, L. Chen, C. Peng, Z. Chen, Y. Zhang, and Q. Fan, "Catalyst Microstructure Examination of PEMFC Membrane," *Journal of the Electrochemical Society*, **151** (2004) A48–A52.

[147] A. A. Kulikovsky, "Quasi-3D Modeling of water transport in Polymer Electrolyte Fuel Cells," *Journal of the Electrochemical Society*, **150** (2003) A1432–A1439.

[148] P. Berg, K. Promislow, J. S. Pierre, J. Stumper, and B. Wetton, "Water Management in PEM Fuel Cells," *Journal of the Electrochemical Society*, **151** (2004) A341–A353.

[149] A. Su, F. Weng, C. Hsu, and Y. Chen, "Studies on Flooding in PEM Fuel Cell Cathode Channels," *International Journal of Hydrogen Energy*, **31** (2006) 1031 – 1039.

[150] W. He, J. S. Yi, and T. V. Nguyen, "Two-Phase Flow Model of the Cathode of PEM Fuel Cells using Interdigitated Flow Fields," *AICHE*, **46** (2000) 2053–2064.

[151] S. W. Cha, R. Hayre, Y. Park, and F. B. Prinz, "Electrochemical impedance investigation of flodding in micro-flow channels for proton exchange membrane fuel cells," *Journal of Power Sources*, **161** (2006) 138–142.

[152] F. Barbir, H. Gorgun, and X. Wang, “Relationship Between Pressure Drop and Cell Resistance as a Diagnostic Tool for PEM Fuel Cells,” *Journal of Power Sources*, **141** (2005) 96–101.

[153] S. Ge and C.-Y. Wang, “Liquid Water Formation and Trasnport in PEFC Anode,” *Journal of the Electrochemical Society*, **154** (2007) B998–B1005.

[154] I. A. Schneider, H. Kuhn, A. Wokaun, and G. G. Scherer, “Fast locally resolved electrochemical impedance spectroscopy in polymer electrolyte fuel cells,” *Journal of the Electrochemical Society*, **152** (2005) A2092–A2103.

[155] I. A. Schneider, H. Kuhn, A. Wokaun, and G. G. Scherer, “Spatially resolved characterization of PEFCs using simultaneously neutron radiography and locally resolved impedance spectroscopy,” *Electrochemistry Communications*, **7** (2005) 1393–1397.

[156] I. A. Schneider, H. Kuhn, A. Wokaun, and G. G. Scherer, “Study of Water Balance in a Polymer Electrolyte Fuel Cell by Locally Resolved Impedance Spectroscopy,” *Journal of the Electrochemical Society*, **152** (2005) A2383–A2389.

[157] N. Fouquet, C. Doulet, C. Nouillant, G. Dauphin-Tanguy, and B. Ould-Bouamama, “Model based PEM fuel cell state-of-health monitoring via ac impedance measurements,” *Journal of Power Sources*, **159** (2006) 905–913.

[158] G. J. Brug, A. L. G. van den Eeden, M. Sluyters-Rehbach, and J. H. Sluyters, “The Analysis of Electrode Impedances Complicated by the Presence of a Constant Phase Element,” *Journal of Electroanalytic Chemistry*, **176** (1984) 275–295.

[159] J. R. Macdonald, editor, *Impedance Spectroscopy: Emphasizing Solid Materials and Systems* (New York: John Wiley & Sons, 1987).

[160] A. Lasia, “Electrochemical Impedance Spectroscopy and its Applications,” in *Modern Aspects of Electrochemistry*, R. E. White, B. E. Conway, and J. O. Bockris, editors, volume 32 (New York, New York: Plenum Press, 1999) 143–248.

[161] Z. Lukacs, “The Numerical Evaluation of the Distortion of EIS Data due to the Distribution of Parameters,” *Journal of Electroanalytical Chemistry*, **432** (1997) 79–83.

[162] Z. Lukacs, “Evaluation of Model and Dispersion Parameters and Their Effects on the Formation of Constant-Phase Elements in Equivalent Circuits,” *Journal of Electroanalytical Chemistry*, **464** (1999) 68–75.

[163] J. R. Macdonald, “Generalizations of Universal Dielectric Response and a General Distribution-of-Activation-Energies Model for Dielectric and Conducting Systems,” *Journal of Applied Physics*, **58** (1985) 1971–1978.

[164] J. R. Macdonald, “Frequency Response of Unified Dielectric and Conductive Systems Involving an Exponential Distribution of Activation Energies,” *Journal of Applied Physics*, **58** (1985) 1955–1970.

[165] R. L. Hurt and J. R. Macdonald, “Distributed Circuit Elements in Impedance Spectroscopy: A Unified Treatment of Conductive and Dielectric Systems,” *Solid State Ionics*, **20** (1986) 111–124.

[166] J. R. Macdonald, “Linear Relaxation: Distributions, Thermal Activation, Structure, and Ambiguity,” *Journal of Applied Physics*, **62** (1987) R51–R62.

[167] J. R. Macdonald, “Power-Law Exponents and Hidden Bulk Relaxation in the Impedance Spectroscopy of Solids,” *Journal of Electroanalytical Chemistry*, **378** (1994) 17–29.

[168] Z. Kerner and T. Pajkossy, “impedance of rough capacitive electrode: role of surface disorder,” *Journal of Electroanalytical Chemistry*, **448** (1998) 139–142.

[169] C. Hitz and A. Lasia, “Experimental study and modeling on impedance of HER on porous Ni electrode,” *Journal of Electroanalytical Chemistry*, **500** (2001) 213–222.

[170] J.-B. Jorcin, M. E. Orazem, N. Pébère, and B. Tribollet, “CPE Analysis by Local Electrochemical Impedance Spectroscopy,” *Electrochimica Acta*, **51** (2006) 1473–1479.

[171] V. M.-W. Huang, V. Vivier, M. E. Orazem, N. Pébère, and B. Tribollet, “The Apparent CPE Behavior of a Disk Electrode with Faradaic Reactions,” *Journal of the Electrochemical Society*, **154** (2007) C99–C107.

[172] M. Mazurek, N. Benker, C. Roth, T. Buhrmester, and H. Fuess, “Electrochemical Impedance and X-Ray Absorption Spectroscopy (EXAFS) as In-Situ Methods to study the PEMFC Anode,” *Fuel Cells*, **1** (2006) 16–20.

[173] A.-K. Meland, S. Kjelstrup, and D. Bedeaux, “Rate Limiting Proton Hydration in the Anode of the PEM Fuel Cell,” *Journal of Membrane Science*, **282** (2006) 96–108.

[174] J. Labato, M. A. Rodrigo, J. Linares, and K. Scott, “Effect of the Catalytic Ink Preparation Method on the Performance of High Temperature PEM Fuel Cells,” *Journal of Power Sources*, **157** (2006) 284–292.

[175] K.-T. Jeng, C.-C. Chien, N.-Y. Hsu, W.-M. Huang, S.-D. Chiou, and S.-H. Lin, “Fabrication and inpedance studies of DMFC anode incorporated with CNT-supported high metal content electrocatalyst,” *Journal of Power Sources*, **2007** (2007) 33–41.

[176] A. Bieberle and L. J. Gauckler, “Reaction Mmechanism of Ni pattern anodes for SOFC,” *Solid State Ionics*, **135** (2000) 337–345.

[177] N.-Y. Hsu, S.-C. Yen, K.-T. Jeng, and C.-C. Chien, "Impedance Studies and Modeling of Direct Methanol Fuel Cell Anode with Interface and Porous Structure Perspectives," *Journal of Power Sources*, **161** (2006) 232–239.

[178] S.-S. Hsieh, S.-H. Yang, and C.-L. Feng, "Characterization of the operational parameters of a H2-air micro PEMFC with different flow fields by impedance spectroscopy," *Journal of Power Sources*, **162** (2006) 262–270.

[179] S. K. Roy and M. E. Orazem, "Graphical Estimation of Interfacial Capacitance of PEM Fuel Cells from Impedance Measurements," *Journal of the Electrochemical Society*, **xxx** (2008) submitted.

[180] B. Andreaus, A. J. McEvoy, and G. G. Scherer, "Analysis of Performance Losses in Polymer Electrolyte Fuel Cells at High Current Densities by Impedance Spectroscopy," *Electochimica Acta*, **47** (2002) 2223–2229.

[181] M. Ciureanu, "Effects of Nafion dehydration in PEM fuel cells," *Journal of Applied Electrochemistry*, **34** (2004) 705–714.

[182] A. G. Hombrados, L. Gonzalez, M. A. Rubio, W. Agila, E. Villanueva, D. Guinea, E. Chinarro, B. Moreno, and J. R. Jurado, "Symmetrical Electrode Mode for PEMFC Characterization using Impedance Spectroscopy," *Journal of Power Sources*, **151** (2005) 25–31.

[183] T. Abe, H. Shima, K. Watanabe, and Y. Ito, "Study of PEFCs by AC Impedance, Current Interrupt, and Dew Point Measurements I. Effect of Humidity in Oxygen Gas," *Journal of the Electrochemical Society*, **151** (2004) A101–A105.

[184] S. v. Kraemer, M. Puchner, P. Jannasch, A. Lundblad, and G. Lindbergh, "Gas Diffusion Electrodes and Membrane Electrode Assemblies Based on a Sulfonated Polysulfone for High-Temperature PEMFC," *Journal of the Electrochemical Society*, **153** (2006) A2077–A2084.

[185] M. Ciureanu and R. Roberge, "Electrochemical Impedance Study of PEM Fuel Cells. Experimental Diagnostic and Modeling of Air Cathode," *Journal of Physical Chemistry B*, **105** (2001) 3531–3539.

[186] T. Romero-Castana, L. G. Arriaga, and U. Cano-Castillo, "Impedance Spectroscopy as a Tool in the Evaluation of MEA," *Journal of Power Sources*, **118** (2003) 179–182.

[187] N. Wagner and M. Schulze, "Change of Electrochemical Impedance Spectra during CO Poisoning of the Pt and Pt-Ru Anodes in a Membrane Fuel Cell (PEFC)," *Electochimica Acta*, **48** (2003) 3899–3907.

[188] N. Wagner and E. Glzow, "Change of electrochemical impedance spectra (EIS) with time during CO-poisoning of the Pt-anode in a membrane fuel cell," *Journal of Power Sources*, **127** (2004) 341–347.

[189] M. N. Tsampas, A. Pikos, S. Brosda, A. Katsaounis, and C. G. Vayenas, "The Effect of Membrane Thickness on the Conductivity of Nafion," *Electochimica Acta*, **51** (2006) 2743–2755.

[190] E. H. Sanders, K. A. McGradya, G. E. Wneka, C. A. Edmondsonb, J. M. Mueller, J. J. Fontanella, S. Suarez, and S. G. Greenbaum, "Characterization of Electrosprayed Nafion Films," *Journal of Power Sources*, **129** (2004) 55–61.

[191] F. Liu, B. Yi, D. Xing, J. Yu, Z. Hou, and Y. Fu, "Development of Novel Self-Humidifying Composite Membranes for Fuel Cells," *Journal of Power Sources*, **124** (2003) 81–89.

[192] V. Ramani, J. M. Fenton, H. R. Kunz, and K. R. Cooper, *Experimental Methods and Data Analyses for Polymer Electrolyte Fuel Cells* (Southern Pines, NC: Scribner Associates, Inc., 2005).

[193] D. A. Blom, J. R. Dunlap, T. A. Nolan, and L. F. Allarda, "Preparation of Cross-Sectional Samples of Proton Exchange Membrane Fuel Cells by Ultramicrotomy for TEM," *Journal of the Electrochemical Society*, **150** (2003) A414–A418.

[194] S. K. Roy and M. E. Orazem, "Error Analysis of the Impedance Response of PEM Fuel Cells," *Journal of the Electrochemical Society*, **154** (2007) B883–B891.

[195] A. Z. Weber and J. Newman, "Transport in Polymer-Electrolyte Membranes 2. Mathematical Models," *Journal of the Electrochemical Society*, **151** (2004) A311–A325.

[196] F. Y. Zhang, X. G. Yang, and C. Y. Wang, "Liquid water removal from a PEM fuel cell," *Journal of the Electrochemical Society*, **153** (2006) A225–A232.

[197] X. Cheng, J. Zhang, Y. Tang, C. Song, J. Shen, D. Song, and J. Zhang, "Hydrogen crossover in high-temperature PEM fuel cell," *Journal of Power Sources*, **167** (2007) 25–31.

[198] M. C. Leverett, "Capillary Behavior in porous solid," in *Pet. Trans. AIME*, volume 142 (1941) 152.

[199] X. Li and I. Sabir, "Review of Bipolar Plates in PEM Fuel Cells: Flow-Field Designs," *International Journal of Hydrogen Energy*, **30** (2005) 359 – 371.

[200] S. Hsieh, S. Yang, J. Kuo, C. Huang, and H. Tsai, "Study of Operational Parameters on the Performance of Micro PEMFCs with Different Flow Fields," *Energy Conversion and Management*, **47** (2006) 1868–1878.

[201] A. de Souza and E. R. Gonzalez, "Influence of the operational parameters on the performance of polymer electrolyte membrane fuel cells with different flow fields," *J Solid State Electrochem*, **7** (2003) 651–657.

[202] A. Su, Y. C. Chiu, and F. B. Weng, "The Impact of Flow Field Pattern on Concentration and Performance in PEMFC," *International Journal of Energy Research*, **29** (2005) 409–425.

[203] Y. Yoon, W. Lee, G. Park, T. Yang, and C. Kim, "Effects of Channel Configurations of Flow Field Plates on the Performance of a PEMFC," *Electochimica Acta*, **50** (2004) 709–712.

[204] S. Dutta, S. Shimpalee, and J. W. V. Zee, "Three-Dimensional Numerical Simulation of Straight Channel PEM Fuel Cell," *Journal of Applied Electrochemistry*, **30** (2000) 135–146.

[205] W. k. Lee, S. Shimpalee, and J. W. V. Zee, "Verifying Predictions of Water and Current Distributions in a Serpentine Flow Field Polymer Electrolyte Membrane," *Journal of The Electrochemical Society*, **150** (2005) A341–A348.

[206] A. Kazim, H. T. Liu, and P. Forges, "Modeling of Performance of PEM Fuel Cells with Conventional and Interdigitated Flow Fields," *Journal of Applied Electrochemistry*, **29** (1999) 1409–1416.

[207] T. V. Nguyen, "A Gas Distributor Design for Proton-Exchange-Membrane Fuel Cells," *Journal of the Electrochemical Society*, **143** (1996) L103.

[208] R. Makharia, M. F. Mathias, and D. R. Baker, "Measurement of Catalyst Layer Electrolyte Resistance in PEFCs using Electrochemical Impedance Spectroscopy," *Journal of the Electrochemical Society*, **152** (2005) A970–A977.

[209] Y. Bultel, L. Genies, O. Antoine, P. Ozil, and R. Durand, "Modeling Impedance Diagrams of Active Layers in Gas Diffusion Electrodes: Diffusion, Ohmic Drop Effects and Multistep Reactions," *Journal of Electroanalytical Chemistry*, **527** (2002) 143–155.

[210] M. E. Orazem, T. E. Moustafid, C. Deslouis, and B. Tribollet, "The Error Structure of Impedance Spectroscopy Measurements for Systems with a Large Ohmic Resistance with Respect to the Polarization Impedance," *Journal of the Electrochemical Society*, **143** (1996) 3880–3890.

[211] S. K. Roy and M. E. Orazem, "Use of Deterministic Impedance Models for Interpretation of Low-Frequency Inductive Loops in PEM Fuel Cells," *ECST-Proton Exchange Membrane Fuel Cells 6*, **3** (2006) 1031–1040.

[212] I. Epelboin, M. Keddam, and J. C. Lestrade, "Faradaic impedance and intermediates in electrochemical reactions," *Faraday Discussions*, **56** (1975) 264–275.

[213] R. D. Armastron, R. E. Firman, and H. R. Thirsk, "AC Impedance of complex eelctrochemical reactions," *Faraday Discussions*, **56** (1975) 244–263.

[214] R. D. Armstrong and K. Edmondson, "The impedance of metals in the passive and transpassive regions," *Electochimica Acta*, **18** (1973) 937–943.

[215] H. Xu, R. Kunz, and J. M. Fenton, "Investigation of Platinum Oxidation in PEM Fuel Cells at Various RH," *Electrochemical and Solid-State Letters*, **10** (2007) B1–B5.

[216] Y. Bultel, K. Wiezell, F. Jaouen, P. Ozil, and G. Lindberg, "Investigation of mass transport in gas diffusion layer at the air cathode of a PEMFC," *Electochimica Acta*, **51** (2005) 474–488.

[217] K. Wiezell, P. Gode, and G. Lindbergh, "Steady-state and EIS Investigations of hydrogen electrodes and membranes in the Polymer Electrolyte Fuel Cells," *Journal of the Electrochemical Society*, **153** (2006) A759–A764.

[218] M. E. Orazem and B. Tribollet, "An Integrated Approach to Electrochemical Impedance Spectroscopy," *Electrochimica Acta*, (2008) submitted.

[219] S. K. Roy, M. E. Orazem, and B. Tribollet, "Interpretation of Low-Frequency Inductive Loops in PEM Fuel Cells," *Journal of the Electrochemical Society*, **154** (2007) B1378–B1388.

[220] R. B. Shumbera, H. H. Kan, and J. F. Weaver, "Oxidation of Pt(100)-hex-R0.7 by gas-phase oxygen atoms," *Surface Science*, **601** (2007) 235–246.

[221] P. Agarwal, M. E. Orazem, and L. H. García-Rubio, "Measurement Models For Electrochemical Impedance Spectroscopy: 3. Evaluation of Consistency with the Kramers- Kronig Relations," *Journal of the Electrochemical Society*, **142** (1995) 4159–4156.

[222] M. E. Orazem, "A systematic Approach Toward Error Structure Identification for Impedance Spsectroscopy," *Journal of Electroanalytic Chemistry*, **572** (2004) 317–327.

[223] M. Durbha, M. E. Orazem, and L. H. García-Rubio, "Spectroscopy Applications of the Kramers-Kronig Relations: Implications for Error Structure Identification," *Journal of the Electrochemical Society*, **144** (1997) 48–55.

[224] M. E. Orazem, N. Pébère, and B. Tribollet, "A New Look at Graphical Representation of Impedance Data," *Journal of the Electrochemical Society*, **153** (2006) B129–B136.

[225] S. K. Roy and M. E. Orazem, "Analysis of Flooding as a Stochastic Process in PEM Fuel Cells by Impedance Techniques," *Journal of Power Sources*, (2008) in press.

[226] C. H. Hsu and F. Mansfeld, "Technical Note: Concerning the Conversion of the Constant Phase Element Parameter Y_0 into a Capacitance," *Corrosion*, **57** (2001) 747–748.

[227] G. J. Brug, A. L. G. van den Eeden, M. Sluyters-Rehbach, and J. H. Sluyters, "The Analysis of Electrode Impedance Complicated by the Presence of a Constant Phase Elementt," *J. Electroanal. Chem.*, **176** (1984) 275–295.

[228] S. P. Harrington and T. M. Devine, “Analysis of Electrodes Displaying Frequency Dispersion in Mott-Schottky Tests,” *Journal of the Electrochemical Society*, **155** (2008) C381–C386.

[229] P. Zoltowski, “On the Electrical Capacitance of Interfaces Exhibiting Constant Phase Element Behavior,” *Journal of Electroanalytical Chemistry*, **443** (1998) 149–154.

BIOGRAPHICAL SKETCH

Sunil was born and raised in Bihar, a state in central-eastern India, famous for its agricultural production, educational heritage and as the birthplace of several religions including Buddhism.

He received a BS degree in chemical engineering from the National Institute of Technology, Surat, India, in May 2002, and completed an MS degree in chemical engineering in July 2004 from the prestigious Indian Institute of Technology, Kharagpur. In his MS research, he designed a spray dryer for cost effective drying Aloe vera gel, characterized the gel, and dried powder to constitute skin care products, sponsored by Emami Inc., India. Sunil then joined the Ph.D. program in the Department of Chemical Engineering at the University of Florida (UF) in fall 2004. His doctoral research, sponsored by NASA, investigated several factors related to side reactions and intermediates, and flooding and drying of the fuel cell responsible for degradation in the performance and lifetime, which are the major hurdles in the commercialization of the fuel cell. His research interests include applied electrochemistry such as fuel cell, battery, semiconductor, and nanotechnology.

Sunil has published 5 journal articles and 3 proceeding papers. He is a referee to Journal of Electrochemical Society since 2005, and has served as an elected President of the Student Chapter of The Electrochemical Society at the University of Florida in 2006-07. Sunil received the 2008 IEEE Division H. H. Dow Memorial Student Achievement Award from The Electrochemical Society.